University of Silesia in Katowice

Faculty of Natural Sciences

Institute of Earth Sciences

Katarzyna Skrzyńska

Zeolite mineralization of pyrometamorphic rocks from the Hatrurim Basin, Israel

Doctoral Dissertation

Supervisor: Prof. Dr. habil. Evgeny Galuskin

Sosnowiec, 2024

I am deeply grateful to:

Prof. Dr. habil. Evgeny Galuskin and Prof. Dr. habil. Irina Galuskina

For introducing me to the world of mineralogy,

patience, substantial and methodological support

Dr. habil. Georgia Cametti

For introducing me to crystallography

and sharing her knowledge with me

My colleagues, especially Dr. Rafał Juroszek

For constant support and inspiration

My parents, brother, grandmother and husband

For patience and unconditional support

in the acquisition of education

Publications included in the doctoral dissertation:

1. **Skrzyńska Katarzyna**, Cametti Georgia, Galuskina Irina, Vapnik Yevgeny, Galuskin Evgeny (2022) Flörkeite, $(K_3Ca_2Na)[Al_8Si_8O_{32}]\cdot12H_2O$: A Rare Zeolite from Pyrometamorphic Rocks of the Hatrurim Complex, Israel; *Lithosphere*, volume 2022, article ID 1343791, DOI 10.2113/2022/1343791

   5-year IF 3.0

   List of journals of Ministry of Science and Higher Education of Poland 140 pkt

2. **Skrzyńska Katarzyna**, Cametti Georgia, Galuskina Irina, Vapnik Yevgeny, Galuskin Evgeny (2023) Gismondine, $Sr_4(Al_8Si_8O_{32})\cdot9H_2O$, a new strontium dominant, orthorhombic zeolite of the gismondine series from the Hatrurim Complex, Israel; *American Mineralogist*, 2023, volume 108, pages 149–258, DOI 10.2138/am-2022-8376

   5-year IF 3.5

   List of journals of Ministry of Science and Higher Education of Poland 100 pkt

3. **Skrzyńska Katarzyna**, Cametti Georgia, Juroszek Rafał, Schäfer Christof, Galuskina Irina (2023) New data on minerals with the GIS framework-type structure: gismondine-Sr from the Bellerberg volcano, Germany, and amicite and Ba-rich gismondine from the Hatrurim Complex, Israel; *Mineralogical Magazine*, 2023, 87(3), 443–454, DOI 10.1180/mgm.2023.27

   5-year IF 2.1

   List of journals of Ministry of Science and Higher Education of Poland 100 pkt

Other publications with contributions of the PhD student:

1. Nádudvari Á., Krzykawski T., Jabłońska M., Fabiańska M., **Skrzyńska K.**, Abramowicz A., Książek M., Ciesielczuk J., Organic minerals in a self-heating coal-waste dump in Upper Silesian, Poland: structure, formation pathways and environmental issues (2024), Int. J. Coal Geol., 281, 104403, DOI: 10.1016/j.coal.2023.104403

   5-year IF 6.8

   List of journals of Ministry of Science and Higher Education of Poland 140 pkt

2. Futrzyński J., Juroszek R., **Skrzyńska K.**, Vapnik Y., Galuskin E., Uvarovite from reduced native Fe-bearing paralava, Hatrurim Complex, Israel (2023) Lithosphere, lithosphere_2023_214, DOI:10.2113/2023/lithosphere_2023_214

   5-year IF 3.0

   List of journals of Ministry of Science and Higher Education of Poland 140 pkt

3. Krzątała A., **Skrzyńska K.**, Cametti G., Galuskina I., Vapnik Y., Galuskin E., Fluoralforsite, $Ba_5(PO_4)_3F$ – a new apatite group mineral from the Hatrurim Basin, Negev Desert, Israel (2023), Mineral. Mag., DOI: 10.1180/mgm.2023.58

   5-year IF 2.1

   List of journals of Ministry of Science and Higher Education of Poland 100 pkt

4. Giordani M., **Skrzyńska K.**, Cametti G., Stepwise dehydration of thomsonite (**THO**) with disordered Si/Al distribution: A new partially hydrated phase (2022), Microporous Mesoporous Mater., volume 346, article number 112308

   5-year IF 4.8

   List of journals of Ministry of Science and Higher Education of Poland 100 pkt

5. Kruszewski Ł., Palchik V., Vapnik Y., **Nowak K.**, Banasik K., Galuskina I., Mineralogical, geochemical and rock mechanic characteristics of zeolite-bearing rocks of the Hatrurim Basin, Israel (2021), Minerals, 11(10), 1062

   5-year IF 2.7

   List of journals of Ministry of Science and Higher Education of Poland 100 pkt

6. **Nowak K.**, Galuskina I, Galuskin E., Greenockite whiskers from the Bytom burned coal dump, Upper Silesia, Poland (2020), Minerals, 10(5), 470

   5-year IF 2.7

   List of journals of Ministry of Science and Higher Education of Poland 100 pkt

Summary

The Hatrurim Complex is located in Jordan, Israel and the Palestinian Authority. It consists of separate outcrops spread over the Dead Sea rift valley, located between 10 and 100 km from the Dead Sea Transform Fault. The rocks of the complex were formed as a result of pyrometamorphism (so-called combustion metamorphism), which corresponds to high-temperature and low-pressure conditions of rock transformations. The largest outcrop of pyrometamorphic rocks in Israel is the Hatrurim Basin, a stratotype of the complex. It is characterized by a great variety of high-temperature metamorphic rocks. Intensive studies over the last decade have enabled a better understanding of the mineralogy of the Hatrurim Complex, leading to the discovery of many new natural phases. These investigations have focused mainly on high-temperature rock-forming minerals, whereas the low-temperature mineralization has remained essentially unexplored.

The objective of the present doctoral dissertation has been to characterize the zeolite mineralization of the pyrometamorphic rocks of the Hatrurim Basin. Samples originating from the collection of Prof. Galuskin's research group were used for the study. In addition, samples collected during fieldwork in 2022 were analyzed. In order to achieve the desired objective, the following methods of instrumental analysis were applied: scanning electron microscopy, electron microprobe analysis, Raman spectroscopy, and single-crystal X-ray diffraction. In total, nearly 120 thin sections and dozens of rock samples were examined.

The most abundant zeolite in the pyrometamorphic rocks of the Hatrurim Basin is flörkeite, $K_3Ca_2Na[Al_8Si_8O_{32}]\cdot12H_2O$. It is a rare zeolite with **PHI-**type structure. To date, flörkeite has been known only from the type locality – the Bellerberg volcano in Germany. In Israel, flörkeite has been found in several types of rocks in association with the following minerals: thomsonite-Ca, minerals of the gismondine series, minerals of the tobermorite supergroup, and vertumnite. It is important to note that flörkeite crystallises at the end of the low-temperature mineralization sequence, overgrowing previously formed minerals or filling the remaining space in the cavities. The structural investigation confirmed the triclinic symmetry and a fully ordered structure. In addition, the comparison of the Raman spectra of flörkeite and minerals of the phillipsite series revealed that the main band at 470 cm^{-1}, characteristic for the **PHI**-type structures, is independent of the Si/Al ratio and the arrangement of cations in the framework.

During the work on the project, a new mineral – gismondine-Sr, $Sr_4[Al_8Si_8O_{32}]\cdot9H_2O$, was discovered. It is the strontium analog of gismondine-Ca with a **GIS-**type structure.

Gismondine-Sr was found in partially melted hornfels, which is mainly composed of wollastonite, gehlenite and minerals of the grossular-andradite garnet series. A number of zeolites characterized by low Si/Al ratios were identified in the low-temperature mineralization, similar to the flörkeite association. Interestingly, only the new mineral was rich in Sr, whereas the surrounding zeolites were not enriched. Chemical composition analyses revealed that gismondine-Sr differs from gismondine-Ca not only by the dominant cation, but also by the significant substitution of monovalent cations (mainly potassium), which was not observed in the calcium counterpart. The structural investigation enabled the solution and refinement of the new zeolite structure in the $B22_12$ space group with the following unit cell parameters $a = 14.0256(2)$ Å, $b = 10.45900(10)$ Å, $c = 13.79360(10)$ Å, $V = 2023.44(4)$Å^3. Contrary to the monoclinic gismondine-Ca, gismondine-Sr crystallizes in the orthorhombic crystal system. Both minerals have an ordered aluminosilicate framework. The extraframework cations of gismondine-Sr are disordered, a feature which contrasts with the ordered cation arrangement of gismondine-Ca. In addition, a comparison of both frameworks showed significant deformations of the eight-membered rings in the structure of the strontium analog. The spectroscopic study of minerals with **GIS-**type structure showed that the main band is located about 460 cm^{-1} regardless of the elliptical deformation of the eight-membered rings.

Insightful analyses of obtained results and literature data on minerals with **GIS-**type structure enabled to distinguish two mineral series varying in Si/Al ratio. The series with a ratio equal to 1, including gismondine-Sr, gismondine-Ca, and amicite, can be represented by the following general formula $(M_yD_{0.5(8-y)})[Al_8Si_8O_{32}] \cdot nH_2O$, wherein $y \leq 8$ and represents the stoichiometric coefficient of the monovalent cations. Additionally, a Ba-rich mineral of this series has been found in pyrometamorphic rocks, and can be considered as a potentially new mineral. The second series includes minerals with a Si/Al ratio greater than 1.66. The general formula of this series can be written as $(M_yD_{0.5(x-y)})[Al_xSi_{(16-x)}O_{32}] \cdot nH_2O$, where $x \leq 8$ and $y \leq 8$ denote coefficients of trivalent Al cation and monovalent cations, respectively. Accordingly, garronite-Ca, gobbinsite, and garronite-Na belong to this series. However, the distinction between gobbinsite and garronite-Na is disputable, as they have been distinguished based on slightly different hydration levels and differences in Si/Al ratios, resulting in various Na contents.

In summary, the occurrence of flörkeite in various types of pyrometamorphic rocks indicates the regional character of relatively uniform conditions for zeolite formation in the Hatrurim Basin. The formation of this mineralization can be divided into two stages.

6

Ca played a major role in the first stage, and rarely Na-enriched minerals may be found. However, monovalent cations (Na and K) were dominant in the second stage, resulting in the formation of flörkeite at the end of the crystallization sequence. Generally, zeolites from the pyrometamorphic rocks of the Hatrurim Complex are characterized by a low Si/Al ratio implied by a high Al content in the crystallization environment and consequently, high alkalinity. Such conditions resulted from the interaction of meteoric water and clinker-like minerals, which induced Al release into the system. Also, local enrichment in Sr and Ba is a result of their release from minerals such as barium feldspar or minerals of the fluorapatite-fluorellestadite series.

The abovementioned results were published as three contributions to mineralogical journals.

Streszczenie

Wychodnie skał Kompleksu Hatrurim znajdują się na terenie Jordanii, Izraela oraz Autonomii Palestyńskiej. Skały występują na obszarze Pustyni Judzkiej (Autonomia Palestyńska) oraz Negew (Izrael) w odległości od 10 do 100 km od uskoku transformacyjnego Morza Martwego. Kompleks zbudowany jest ze skał pirometamorficznych, które tworzą się w wyniku tzw. metamorfizmu spalania, czyli w warunkach wysokiej temperatury i niskiego ciśnienia. Te nietypowe warunki przeobrażania oraz unikatowy skład chemiczny protolitu przyczyniły się do powstania wielu rzadkich oraz nowych minerałów. Największym obszarem występowania tych skał na terenie Izraela jest Basen Hatrurim, który odznacza się dużą różnorodnością wysokotemperaturowych skał pirometamorficznych. Od ponad 10 lat kompleks ten jest intensywnie badany przez naukowców. Jednak jak dotąd badania te skupiały się głównie na minerałach wysokotemperaturowych, podczas gdy, mineralizacja niskotemperaturowa była opisywana jedynie pobieżnie i wyrywkowo. Na szczególną uwagę zasługuje mineralizacja zeolitowa, której występowanie było powszechnie znane, jednak nie była ona przedmiotem dokładnych badań.

Celem niniejszej rozprawy doktorskiej było szczegółowe scharakteryzowanie mineralizacji zeolitowej występującej w pustkach wysokotemperaturowych skał pirometamorficznych z Basenu Hatrurim w Izraelu. W trakcie projektu przeanalizowane zostały próbki skalne pochodzące z kolekcji naukowej zespołu badawczego „Nowe minerały skał pirometamorficznych" Profesora dr hab. Evgenyego Galuskina. Ponadto przebadano próbki pozyskane podczas prac terenowych prowadzonych na obszarze Basenu Hatrurim w 2022 roku. Celem dokładnej identyfikacji zeolitów występujących w próbkach, przeprowadzono szereg analiz stosując następujące metody instrumentalne: skaningowa mikroskopia elektronowa, mikrosonda elektronowa, spektroskopia Ramana oraz eksperymenty dyfrakcji rentgenowskiej na monokrysztale. Podsumowując, przebadano prawie 120 płytek cienkich oraz kilkadziesiąt próbek skalnych.

Najczęściej występującym zeolitem w pustkach skał pirometamorficznych Basenu Hatrurim jest flörkeit, $K_3Ca_2Na[Al_8Si_8O_{32}]\cdot12H_2O$. Jest to rzadki minerał należący do zeolitów z topologią struktury **PHI**. Do tej pory był znany jedynie z wulkanu Bellerberg w Niemczech, gdzie został opisany po raz pierwszy. W próbkach izraelskich flörkeit został znaleziony w kilku typach skał w asocjacji z thomsonitem-Ca, minerałami serii gismondinu, minerałami z supergrupy tobermorytu oraz rzadkim minerałem vertumnitem. Co istotne, flörkeit zawsze występował na końcu sekwencji krystalizacji asocjacji

niskotemperaturowej narastając na wcześniej powstałe kryształy lub wypełniając pozostałą przestrzeń w pustkach skalnych. Badania strukturalne tego rzadkiego minerału potwierdziły jego trójskośną symetrię i w pełni uporządkowaną strukturę. Dodatkowo przeprowadzono badania spektroskopowe minerałów ze strukturą typu **PHI**. Porównanie widm Ramana flörkeitu oraz minerału z serii phillipsytu pokazało, że główne pasmo znajdujące się na około 470 cm^{-1} jest niezależne od stosunku Si/Al oraz uporządkowania kationów w szkielecie.

Podczas prac nad projektem odkryto nowy minerał – gismondin-Sr, $Sr_4[Al_8Si_8O_{32}]\cdot 9H_2O$. Jest to strontowy analog znanego gismondinu-Ca z topologią struktury **GIS**. Gismondin-Sr został znaleziony w pustkach częściowo przetopionego hornfelsu zbudowanego z wollastonitu, gehlenitu oraz granatów z serii grossular-andradyt-schorlomit. W asocjacji niskotemperaturowej zidentyfikowano szereg zeolitów charakteryzujących się niskim stosunkiem Si/Al, podobnie jak w przypadku flörkeitu. Co ciekawe, jedynie nowy minerał odznaczał się dużą zawartością Sr, podczas gdy zeolity z asocjacji były ubogie w ten pierwiastek. Badania składu chemicznego ujawniły, że gismondin-Sr różni się od gismondinu-Ca nie tylko kationem dominującym, ale także znacznymi domieszkami kationów jednowartościowych (głównie potasu), które do tej pory nie były opisywane w odmianie wapniowej. Badania strukturalne nowego minerału pozwoliły na rozwiązanie i udokładnienie jego struktury krystalicznej ($B22_12$, $a = 14.0256(2)$ Å, $b = 10.45900(10)$ Å, $c = 13.79360(10)$ Å, $V = 2023.44(4)$Å^3). Gismondin-Sr krystalizuje w układzie rombowym w przeciwieństwie do jednoskośnego gismondinu-Ca. Oba minerały posiadają uporządkowany szkielet glinokrzemianowy, jednak gismondin-Sr charakteryzuje się nieuporządkowanymi kationami poza szkieletowymi w odróżnieniu do gismondinu-Ca. Dodatkowo porównanie szkieletów obu odmian pokazało znaczne deformacje pierścieni 8-członowych w strukturze strontowego analogu. Natomiast, badania spektroskopowe minerałów z serii gismondinu ujawniły, że główne pasmo na widmie Ramana, znajdujące się na około 460 cm^{-1}, jest niezależne od eliptycznych deformacji w szkieletach zeolitów z topologią **GIS**.

Wnikliwa analiza pozyskanych danych oraz danych literaturowych dotycząca minerałów z topologią struktury **GIS** pozwoliła na wyróżnienie dwóch serii mineralnych z różnym stosunkiem Si/Al. Do serii ze stosunkiem równym 1, o następującym wzorze ogólnym $(M_yD_{0.5(8-y)})[Al_8Si_8O_{32}]\cdot nH_2O$, gdzie $y \leq 8$ oznacza zawartość kationów jednowartościowych, należą gismondin-Sr, gismondin-Ca oraz amicyt. Dodatkowo, w skałach pirometamorficznych znaleziono minerał z serii gismondinu bogaty w Ba, który może być w przyszłości kolejnym członem tej serii. Druga seria charakteryzuje się stosunkiem Si/Al powyżej 1.66 i jest opisana

wzorem ogólnym $(M_yD_{0.5(x-y)})[Al_xSi_{(16-x)}O_{32}] \cdot nH_2O$, gdzie $x \leq 8$ oznacza zawartość Al., a y – kationów jednowartościowych. Do tej serii należą garronit-Ca, garronit-Na oraz gobbinsyt. Jednakże dokładne porównanie dwóch ostatnich gatunków mineralnych poddało w wątpliwość podstawy ich wyróżnienia, ponieważ różnią się one jedynie stopniem uwodnienia oraz stosunkiem Si/Al, skutkującym różną zawartością Na.

Podsumowując, znalezienie flörkeitu w różnych typach skał pirometamorficznych wskazuje na regionalny charakter stosunkowo jednolitych warunków powstawania zeolitów w Basenie Hatrurim. Formowanie się mineralizacji zeolitowej w skałach kompleksu można podzielić na dwa etapy. W pierwszym etapie dominującą rolę odgrywały minerały bogate w Ca, sporadycznie wzbogacone w Na. Drugi etap charakteryzował się powstawaniem minerałów dominujących w Na oraz K. Generalnie minerały zeolitowe ze skał wysokotemperaturowych Basenu Hatrurim charakteryzują się niskim stosunkiem Si/Al, wynikającym z wysokiej zawartości Al w środowisku krystalizacji, a w konsekwencji jego wysoką alkalicznością. Takie warunki były skutkiem interakcji wody opadowej z minerałami skałotwórczymi, których przemiany powodowały uwalnianie się Al do środowiska. Również, lokalne wzbogacenie w Sr oraz Ba jest skutkiem ich uwalniania z minerałów akcesorycznych takich jak skaleń barowy czy minerały z serii fluorapatytu-fluorellestadytu.

Wymiernym rezultatem przeprowadzonych badań jest opublikowanie trzech prac w renomowanych czasopismach naukowych.

Table of Contents

Alphabetical list of abbreviations

The abbreviations of minerals are given in agreement with approved mineral symbols by the International Mineralogical Association Commission on New Minerals, Nomenclature, and Classification (Warr 2021).

Adr – andradite

Ami – amicite

BSE – backscattered electrons spectrometer

Chr – chromite

Cls – celsian

D – divalent cations

dcc – double crankshaft chain

EDX – energy dispersive X-ray spectrometer

EMPA – electron microprobe analysis

Ess – esseneite

Fap – fluorapatite

FAU – framework of structure with faujasite-type topology

Flö – flörkeite

Gh – gehlenite

GIS – framework of structure with gismondine-type topology

gis – gis-type minerals

Gis-Sr – gismondine-Sr

Grs – grossular

kfe – channel along [001] in framework of structure with phillipsite-type topology

Kls – kalsilite

Lat – latiumite

M – monovalent cations

MER – framework of structure with merlinoite-type topology

oto – composite building unit in framework of structure with phillipsite-type topology

PBU – primary building unit

pfu – per formula unit

PHI – framework of structure with phillipsite-type topology

phi – composite building unit in framework of structure with phillipsite-type topology

Phi-K – phillipsite-K

SBU – secondary building unit

SEM – scanning electron microscope

Spl – spinel

T – tetrahedral site

T_5O_{10} – chain building the fibrous zeolites

t-gsm – composite building unit in framework of structure with gismondine-type topology

Thm-Ca – thomsonite-Ca

Wo – wollastonite

Vtn – vertumnite

IMA–CNMNC– International Mineralogical Association Commission on New Minerals, Nomenclature, and Classification

Alphabetical list of mineral names and end-member formulas

The mineral names and end-members formulas are given in agreement with the most recent IMA–CNMNC List of Minerals, as of May 2024. Otherwise, an appropriate references are provided.

Amicite – $K_2Na_2(Al_4Si_4O_{16})\cdot5H_2O$

Andradite – $Ca_3Fe^{3+}{}_2(SiO_4)_3$

Analcime – $Na[AlSi_2O_6]\,H_2O$

Celsian – $Ba[Al_2Si_2O_8]$

Chromite – $Fe^{2+}Cr_2O_4$

Esseneite – $CaFe^{3+}AlSiO_6$

Flörkeite – $K_3Ca_2Na[Al_8Si_8O_{32}]\cdot12H_2O$

Fluorapatite – $Ca_5(PO_4)_3F$

Fluorellestadite – $Ca_5(SiO_4)_{1.5}(SO_4)_{1.5}F$

Garronite-Ca – $Ca_3[Al_6Si_{10}O_{32}]\cdot14H_2O$

Garronite-Na – $Na_6[Al_6Si_{10}O_{32}]\cdot14.3H_2O$

Gehlenite – $Ca_2Al(SiAl)O_7$

Gismondine-Ca - $Ca_4[Al_8Si_8O_{32}]\cdot16H_2O$

Gismondine-Sr – $Sr_4[Al_8Si_8O_{32}]\cdot9H_2O$

Gobbinsite – $Na_5[Al_5Si_{11}O_{32}]\cdot11H_2O$

Gonnardite – $(Na,Ca)_2[(Si,Al)_5O_{10}]\cdot3H_2O$

Grossular – $Ca_3Al_2(SiO_4)_3$

Kalsillite – $KAlSiO_4$

Latiumite – $(Ca,K)[Si,Al]5O_{11}(SO_4,CO_3)$

Merlinoite – $K_5Ca_2[Al_9Si_{23}]O_{64}\cdot24H_2O$

Phillipsite-Ca – $Ca_3[Al_6Si_{10}]O_{32}\cdot12H_2O$

Phillipsite-K – $K_6[Al_6Si_{10}]O_{32}\cdot12H_2O$

Phillipsite-Na – $Na_6[Al_6Si_{10}]O_{32}\cdot12H_2O$

Rankinite – $Ca_3Si_2O_7$

Spinel – $MgAl_2O_4$

Strätlingite – $Ca_2Al(Al,Si)_2O_2(OH)_{10}\cdot2.25H_2O$

Tobermorite supergroup – $Ca_{4+x}(Al_ySi_{6-y})O_{15+2x-y}\cdot5H_2O$ (Biagioni et al. 2015)

Thomsonite-Ca – $NaCa_2[Al_5Si_5]O_{20}\cdot6H_2O$

Willhendersonite – $KCa[Si_3Al_3O_{12}]\cdot5H_2O$

Wollastonite – $CaSiO_3$

Vertumnite – $Ca_4Al_4Si_4O_6(OH)_{24}\cdot3H_2O$

Introduction

Hatrurim Complex

The Hatrurim Complex, also known as the Mottled Zone, is located in Israel in the Negev Desert, in the Palestinian Authority in the Judean Desert, and in Jordan in the Transjordan Plateau (Fig. 1a) (Bentor 1963; Gross 1977). It consists of separate, individual outcrops spread over the rift valley of the Dead Sea, located between 10 and 100 km from the Dead Sea Transform Fault (Vapnik et al. 2015). The Hatrurim Complex is a well-known example of the occurrence of pyrometamorphic rocks. The metamorphic transformations, called combustion metamorphism, of the rocks in this Complex correspond to the conditions of the sanidine facies, characterized by low pressure and exceptionally high temperatures (Gross 1977; Grapes 2010). The largest outcrop of the Hatrurim Complex in Israel is the Hatrurim Basin – a stratotype of the Hatrurim Complex (Fig. 1b) (Burg et al. 1991; Sokol et al. 2019). It covers an area of nearly 48 km^2, which is characterized by a wide variety of high-temperature metamorphic rocks (Gross 1977; Vapnik et al. 2007; Sokol et al. 2019). The area hosts various types of pyrometamorphic rocks, including calcite-zeolite-hydrogarnet rocks, spurrite marbles, larnite pseudoconglomerates, and gehlenite hornfels, each representing a different metamorphic grade (Gross 1977; Burg et al. 1991; Vapnik et al. 2007; Novikov et al. 2013). Nevertheless, the gehlenite-(pseudo)wollastonite-andradite and rankinite-gehlenite paralavas within hornfelses have attracted the greatest attention, mainly due to the high-temperature rock-forming minerals and Ba, V-bearing enclaves (Galuskina et al. 2017b, 2017a; Krzątała et al. 2020, 2023). More recently, the study of the breccia of hydrogrossular-bearing rocks cemented by gehlenite paralava has begun due to their unusual reductive mineral association (Britvin et al. 2015, 2019; Galuskin et al. 2022, 2023b, 2023a). Despite numerous mineralogical studies, the origin of the Hatrurim Complex remains controversial. The presumed protoliths of the metamorphic rocks are sedimentary rocks of the Maastrichtian Ghareb and Paleocene Taqiye Formations, which include clays, marls, and chalks enriched in bituminous matter and oil shale (Gross 1977; Gur et al. 1995; Geller et al. 2012). Furthermore, the thermal energy source that drove the metamorphism is unknown. According to Gur and co-authors, the major combustion metamorphic events occurred around 3 Ma, whereas the initial events occurred at 16 Ma based on K-Ar and ^{40}Ar/^{39}Ar techniques (Gur et al. 1995). One of the hypotheses considers the combustion of organic matter in the Ghareb and Taqiye Formations (Gross 1977; Matthews and Gross 1980; Geller et al. 2012), whereas the second one associates

the pyrometamorphism with tectonically induced mud volcanism and combustion of hydrocarbon gases (Sokol et al. 2007, 2008; Sharygin et al. 2008; Novikov et al. 2013). The rocks of the Hatrurim Complex can be divided into two main mineral assemblages corresponding to two stages of metamorphism (Fig. 2). The first type of rock forms conical hills in the Negev desert and is resistant to the intense weathering of the arid climate. These rocks are products of high-temperature metamorphism – hornfels and paralavas with amygdaloidal cavities (Fig. 2a). Their formation is related to the prograde stage of metamorphism, during which the temperature could locally reach > 1500 °C (Galuskin et al. 2023b). The mineral assemblage of these rocks is considered to be a natural analog of clinker phases (Gross 1977). Nevertheless, the high-temperature rocks have been affected by retrograde metamorphism and weathering processes, as they are strongly veined by a low-temperature mineralization, which also fills amygdaloidal cavities (Vapnik et al. 2007; Kolodny et al. 2014; Juroszek et al. 2020a). The second type of rock occurring in the Hatrurim Complex, the so-called "low-grade Hatrurim", mainly consists of calcium hydrosilicates and zeolites (Fig. 2b, Gross 1977; Vapnik et al. 2007; Kruszewski et al. 2021). These rocks were formed as a result of post-depositional alteration of various sedimentary rocks and as by-products of the hydrothermal alteration of high-temperature metamorphosed rocks (Vapnik et al. 2007; Sokol et al. 2019). Their mineral assemblages correspond to phases found in industrial concrete (Gross 1977; Matthews and Gross 1980; Kolodny et al. 2014; Sokol et al. 2014).
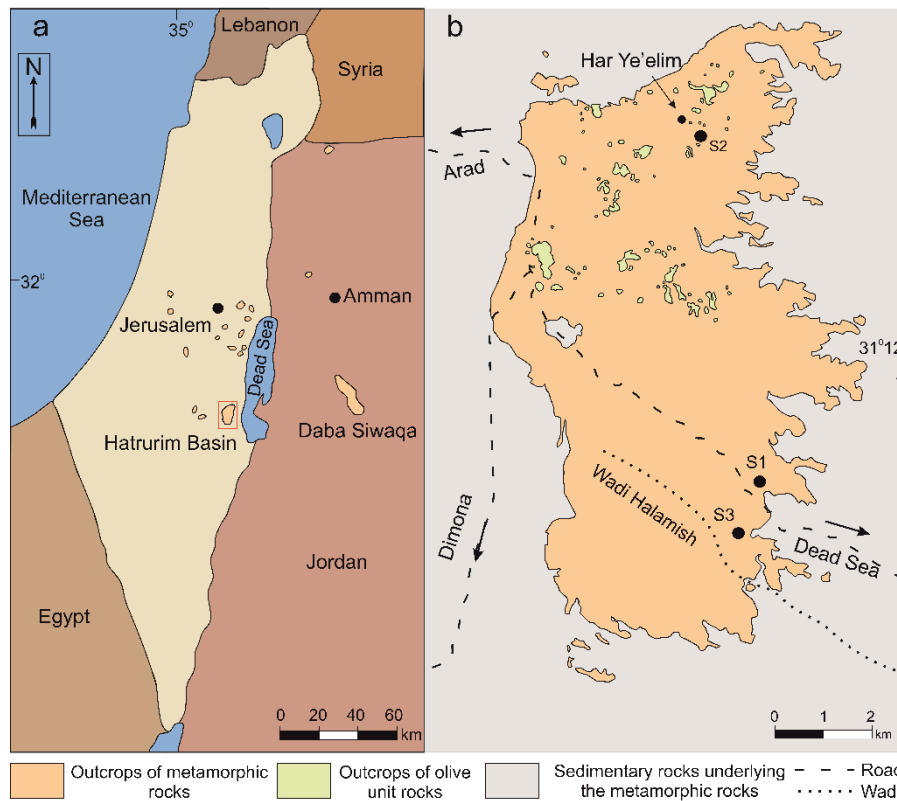
Figure 1 (a) Simplified map of the outcrops of the Hatrurim Complex,
the area outlined by the frame is magnified in (b); (b) Generalized map of the Hatrurim Basin outcrop
considering the olive unit outcrops and exemplary sampling localities
(modified from Geological Map of Israel 1: 50 000, Arad sheet (Hirsch et al. 2008)
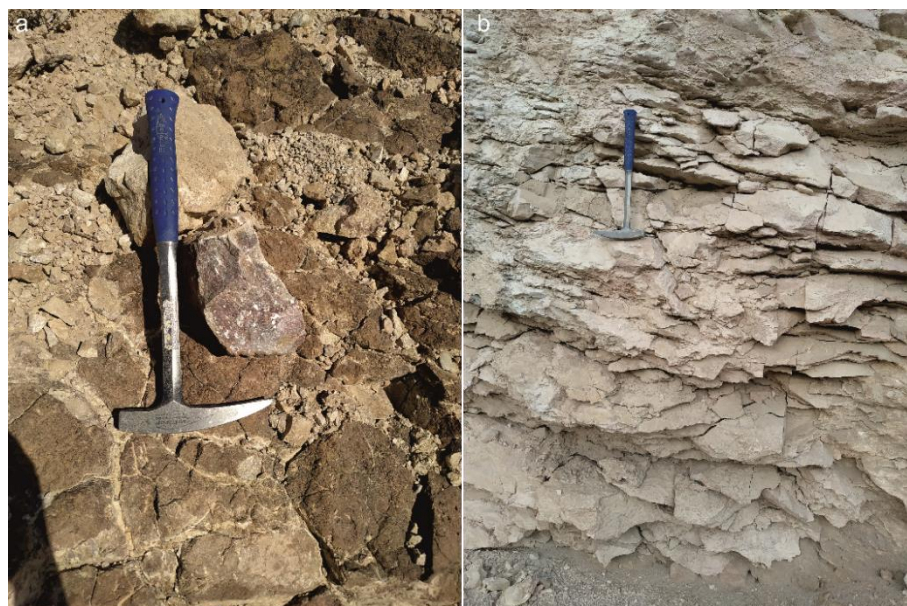
Figure 2 Two main mineral assemblages occurring in the Hatrurim Complex: (a) High-temperature rocks,
(b) Low-temperature calcium-hydrosilicate rocks representing the retrograde stage of metamorphism

Zeolite minerals

According to the International Mineralogy Association, a zeolite is a mineral with a structure consisting of a three-dimensional framework of linked tetrahedra composed of four oxygens and a central cation (T) – a primary building unit (PBU, Fig. 3a). The structure contains open cavities filled with water molecules and exchangeable extraframework cations. In these minerals, dehydration takes place at low temperatures (< 400 °C), and is usually reversible (Coombs et al. 1997). In the case of OH or F anions being present in the coordination sphere of the tetrahedral cation, the given apex is not shared with the adjacent tetrahedra, implying an interruption of the framework. The central tetrahedral site (Fig. 3a) can be occupied by various cations such as Al^{3+}, Si^{4+}, Zn^{2+}, $P^{5+,}$ and Be^{2+} (Coombs et al. 1997; Passaglia and Sheppard 2001; Yang et al. 2023; Kampf et al. 2024). However, aluminosilicate frameworks are the most typical in nature. Therefore, only this type of zeolites will be discussed here. The general formula for aluminosilicate zeolites can be written as $M_xD_y[Al_{x+2y}Si_{n-(x+2y)}O_{2n}]\cdot mH_2O$, where M and D correspond to monovalent and divalent cations, respectively. The square brackets refer to the negatively charged framework resulting from $Si^{4+} \rightarrow Al^{3+}$ substitution (Passaglia and Sheppard 2001). The chemical compositions of zeolites are characterized by a great variety due to the considerable flexibility of their structures. Therefore, only a classification based on the topologies of the structures is reliable. Nevertheless, the diversity of the zeolite framework type structures is relevant. The Structure Commission of the International Zeolite Association has established a three-letter code for each framework type of zeolite, that shall be given as three capital letters in boldface type, e.g., **FAU** (Passaglia and Sheppard 2001; Baerlocher et al. 2007). Within each framework type, different secondary building units (SBUs) can be distinguished, such as single four-membered rings, single six-membered rings, double four-membered rings and T_5O_{10}. They are formed as a consequence of the geometrical arrangements of the PBU (Fig. 3b) (Gottardi and Galli 1985; Armbruster and Gunter 2001). Subsequently, the linked SBUs form chains (Baerlocher et al. 2007, p. 6). For instance, linked four-membered rings form a double crankshaft chain (hereafter abbreviated as *dcc,* Fig. 3c), which is the main building block of the following framework types gismondine (**GIS**), phillipsite **(PHI)** and merlinoite (**MER**). The *dcc* comprises rings with tetrahedral apices alternately pointing up and down, defining the T-O-T angle between them (Fig. 3c, d). This arrangement resembles a corrugated ribbon – crankshaft with a periodicity of ~10Å

(Gottardi and Galli 1985; Armbruster and Gunter 2001). The connected *dcc*s form a three-dimensional framework with cages and channels hosting extraframework cations, which balance the negative charge of the framework (Fig. 3d). The great flexibility of zeolite structures and their variety of chemical compositions imply a considerable diversity in terms of symmetry within a given topology. The highest symmetry in zeolite structures (archetype structure) is the topological symmetry, in which all tetrahedral sites are considered to be equivalent (Gottardi 1979; Smith 1988). In the case of an ordered framework (with non-equivalent tetrahedral sites) the symmetry is reduced to the topochemical symmetry. The real symmetry takes into account the order of the extraframework cations as well as the distortion of the framework caused by unadjusted extraframework sites (Gottardi 1979).
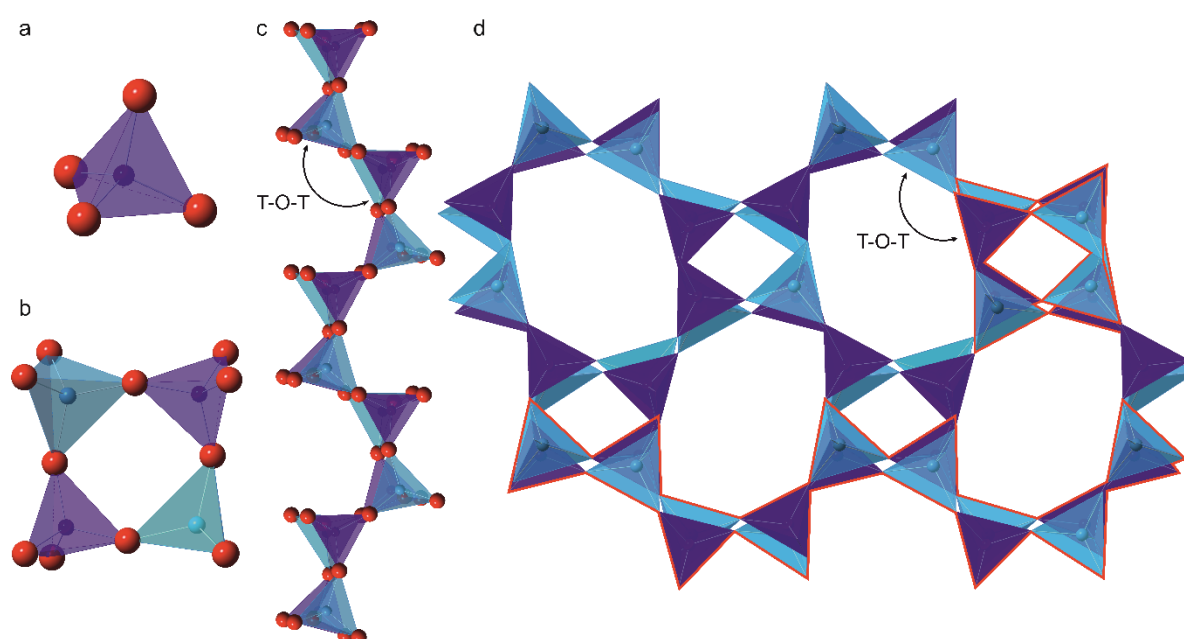

Figure 3 (a) Tetrahedron – primary building unit (PBU) of aluminosilicate framework of zeolite;
*(b) Four-membered ring of tetrahedra – secondary building unit (SBU); (c) Double crankshaft chain (dcc) with marked T-O-T angle; (d) **GIS** framework type with indicated T-O-T angle and dcc marked in red.*

20

Research motivation and objectives

The Hatrurim Complex is a world-famous locality for pyrometamorphic rocks where many rare minerals occur. It has been intensively studied by mineralogists over the last decade, resulting in the discovery of many new natural phases (Sharygin et al. 2013; Galuskina et al. 2017a; Britvin et al. 2019, 2020; Galuskin et al. 2019; Krząтała et al. 2022). To date, studies have mainly focused on high-temperature rock-forming minerals, whereas investigations of the low-temperature mineralization have been extremely limited (Kolodny et al. 2014; Seryotkin et al. 2019; Juroszek et al. 2020b). Generally, the low-temperature mineralization and weathering products of pyrometamorphic rocks have found little interest and were only occasionally the topic of mineralogical research (Lengauer et al. 2009; Juroszek et al. 2018).

Therefore, this project aimed at an insightful characterization of the mineralization occurring in veins and cavities in high-temperature pyrometamorphic rocks, particularly zeolites. The Hatrurim Complex is known for its abundant zeolite mineralisation. Surprisingly, detailed mineralogical identification has been provided to date (Gross 1977).

Figure 4 High-temperature rocks with cavities filled with low-temperature mineralization

Methodology

Initially, the project foresaw both extensive fieldwork and complementary analytical laboratory work. Fieldwork was hampered as consequence of the travel restrictions imposed by the COVID 19 pandemic (2020 – 2022) and the geopolitical situation at the Gaza Strip (2023). Hence, only one week of fieldwork was carried out in 2022 at the Hatrurim Basin in Israel in November of 2022. On this occasion, a number of rock samples were collected. In addition, samples from the collection of Prof. Galuskin's research group were used for the present work. The workflow employed for the mineralogical sample characterization, together with the analytical methods used in the present project, is displayed in Figure 5. The preliminary examination of the rock samples was carried out using an OLYMPUS BX-51 stereoscopic microscope. Qualitative and semi-quantitative chemical composition, mineral association and crystal morphology were determined using a Phenom XL scanning electron microscope equipped with an energy dispersive X-ray (EDX) spectrometer and backscattered electrons (BSE) detectors at the Institute of Earth Sciences, Faculty of Natural Sciences, University of Silesia in Katowice, Poland. Raman spectroscopy investigations were conducted at the same institute using a WITec alpha 300R confocal Raman microscope. Quantitative chemical analyses were performed using Cameca SX100 electron microprobe analyzers (EMPA) with instruments located at the Faculty of Geology, University of Warsaw and Polish Geological Institute, National Research Institute, Poland. Crystals for structural investigation were selected from the polished rock samples under the stereoscopic microscope and mounted on MiTeGen loops. Single-crystal X-ray diffraction experiments were conducted using a Rigaku Synergy-S diffractometer equipped with a dual micro-focused source and a Hypix detector in collaboration with Dr. habil. Georgia Cametti from the University of Bern, Switzerland. Subsequently, the optical properties of crystals were determined using a petrographic microscope. Micro-indentation testing was carried out using a Nexus 400A micro Vickers hardness tester.
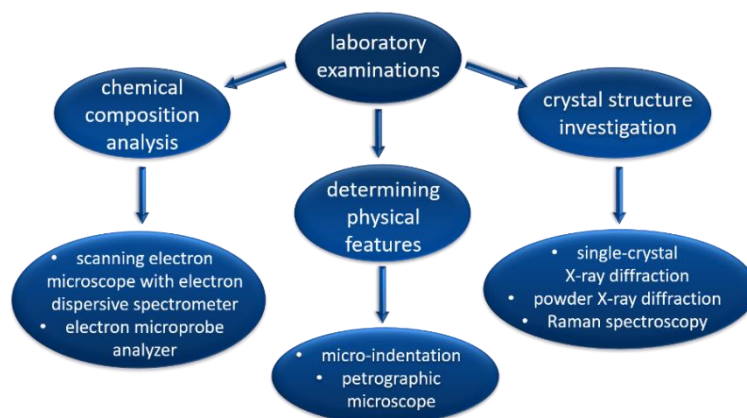
Figure 5 Diagram (work-flow) showing the laboratory methods used in the project

Results – summary of the articles included in the doctoral dissertation

The study of nearly 120 thin sections and dozens of rock samples from various pyrometamorphic rocks has shown that zeolites are predominantly found in amygdaloidal cavities of pyrometamorphic rocks from the Hatrurim Basin, with occurrences in veins being less common. In contrast, carbonate and sulfate mineralizations are found in veins cutting high-temperature rocks (Kolodny et al. 2014). The most abundant zeolite in high-temperature pyrometamorphic rocks of the Hatrurim Basin is a rare zeolite flörkeite, $K_3Ca_2Na[Al_8Si_8O_{32}] \cdot 12H_2O$. Furthermore, a new zeolite, gismondine-Sr, $Sr_4[Al_8Si_8O_{32}] \cdot 9H_2O$, was discovered and fully characterised during the present project. Moreover, a number of mineral species, such as amicite, gonnardite, willhendersonite and strätlingite, previously unknown from this locality, were described. Moreover, the occurrences of other minerals previously identified, such as vertumnite, thomsonite-Ca, gismondine-Ca, were confirmed (Gross 1977; Matthews and Gross 1980; Burg et al. 1991).

Flörkeite

Occurrence and mineral association

The Hatrurim Basin in Israel is the second worldwide occurrence of flörkeite. To date, this mineral had only been described from one locality – Bellerberg volcano, East Eifel volcanic region, Germany (Lengauer et al. 2009). In order to characterize flörkeite and its mineral associations, three types of pyrometamorphic rocks were selected as the most representative samples for a detailed description. These included gehlenite-wollastonite-kalsilite paralava with amygdaloidal texture (Fig. 6a, a'), esseneite-latiumite hornfels (Fig. 6b, b'), and gehlenite-wollastonite-garnet hornfels and paralavas (Fig. 6c, c').

23

In amygdaloidal paralavas (Fig. 6a, a'), vertumnite, $Ca_4Al_4Si_4O_6(OH)_{24} \cdot 3H_2O$, thomsonite-Ca, $NaCa_2[Al_5Si_5O_{20}] \cdot 6H_2O$, and minerals of the tobermorite supergroup, $Ca_{4+x}(Al_ySi_{6-y})O_{15+2x-y} \cdot 5H_2O$ (Biagioni et al. 2015) occur in addition to flörkeite. In the esseneite-latiumite hornfels (Fig. 6b, b'), flörkeite occurs in association with minerals of the phillipsite series. Zeolites of the gismondine series may also be present. Gehlenite-wollastonite-garnet hornfels (Fig. 6c, c') shows the most variable low-temperature mineralization with minerals such as gismondine-Ca, $Ca_4[Al_8Si_8O_{32}] \cdot 18H_2O$ (Wadoski-Romeijn and Armbruster 2013), newly discovered gismondine-Sr, Ba-rich minerals of the gismondine series, thomsonite-Ca, gonnardite, $(Na,Ca)_2[(Si,Al)_5O_{10}] \cdot 3H_2O$, willhendersonite, $KCa[Si_3Al_3O_{12}] \cdot 5H_2O$, and Ba-enriched vertumnite. It is noteworthy that flörkeite always occurs at the end of the crystallization sequence, overgrowing other minerals or filling the remaining space in the cavities.

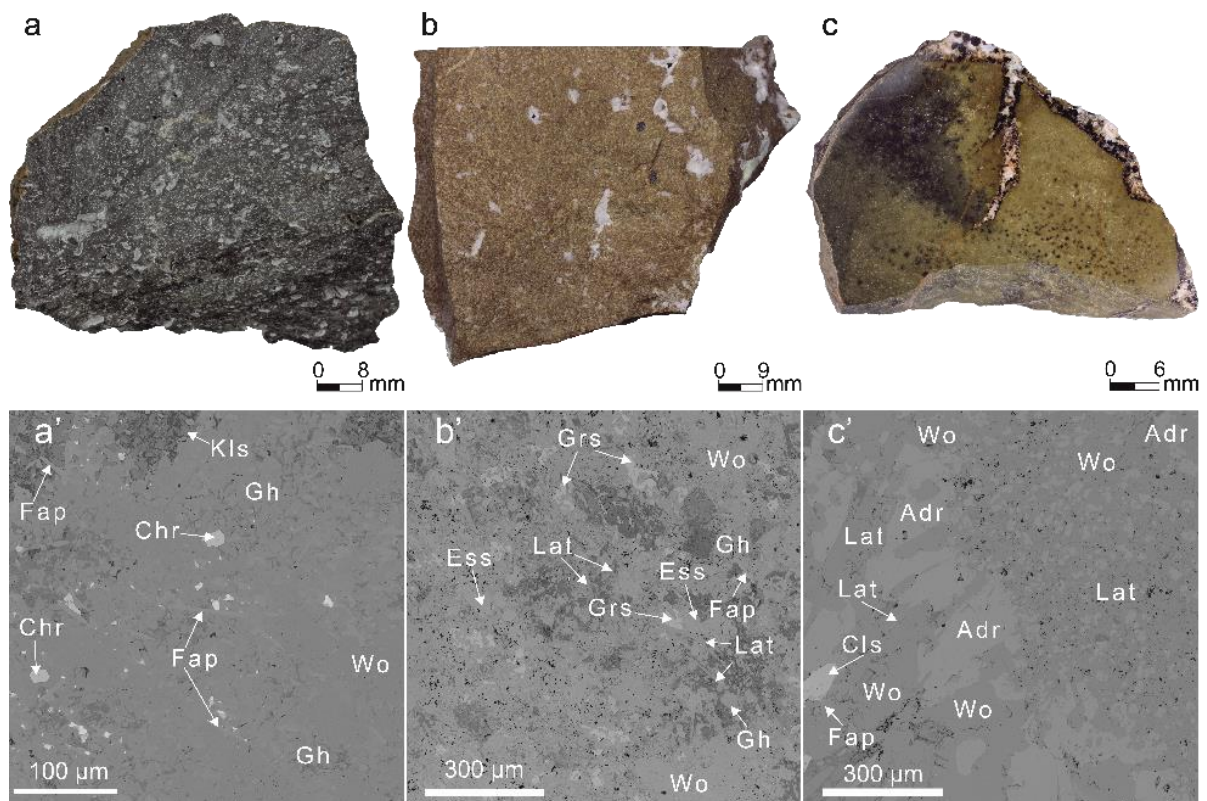Figure 6 General view of rock samples and BSE images of forming minerals in (a, a') Gehlenite-wollastonite-kalsilite paralava with amygdaloidal texture, (b, b') Esseneite-latiumite hornfels, (c, c') Gehlenite-wollastonite-garnet hornfels with paralava part. Adr – andradite, Chr – chromite, Cls – celsian, Ess – esseneite, Fap – fluorapatite, Gh – gehlenite, Grs – grossular, Kls – kalsilite, Lat – latiumite, Wo – wollastonite.

Electron microprobe analyses

Electron microprobe analyses were carried out on flörkeite crystals from all three types of rocks, resulting in the empirical crystal-chemical formulas presented in Table 1.

Table 1 Empirical crystal-chemical formulas of flörkeite from different pyrometamorphic rocks of the Hatrurim Basin calculated based on 16 T-sites

Pyrometamorphic rocks	Empirical crystal-chemical formulas
gehlenite-wollastonite-kalsilite paralava with amygdaloidal voids (Fig. 6a, a')	$K_{2.87}Ca_{1.96}Na_{0.95}[Al_{7.98}Si_{8.02}O_{32}]\cdot6.98H_2O$
esseneite-latiumite hornfels (Fig. 6b, b')	$K_{2.91}Ca_{2.00}Na_{0.91}[Al_{7.96}Si_{8.04}O_{32}]\cdot7.52H_2O$
gehlenite-wollastonie-garnet hornfels and paralavas (Fig. 6c, c')	$K_{2.91}Ba_{0.13}Ca_{1.97}Sr_{0.05}Na_{1.04}[Al_{7.93}Si_{8.07}O_{32}]\cdot8.31H_2O$

The empirical crystal-chemical formulas are close to the end-member formula $K_3Ca_2Na[Al_8Si_8O_{32}]\cdot12H_2O$. Based on EMPA data, the water contents (as calculated by the mass difference to 100%) are always underestimated. By contrast, the SC-XRD data indicate the presence of twelve water molecules per formula unit (*pfu*). A similar divergence was observed in the first description of flörkeite (Lengauer et al. 2009).

Moreover, the comparison of the chemical compositions of minerals from phillipsite series and flörkeite from the Hatrurim Complex with literature data revealed that minerals from Israel stand out by the highest Al content found among natural phillipsite specimens (Fig. 7).
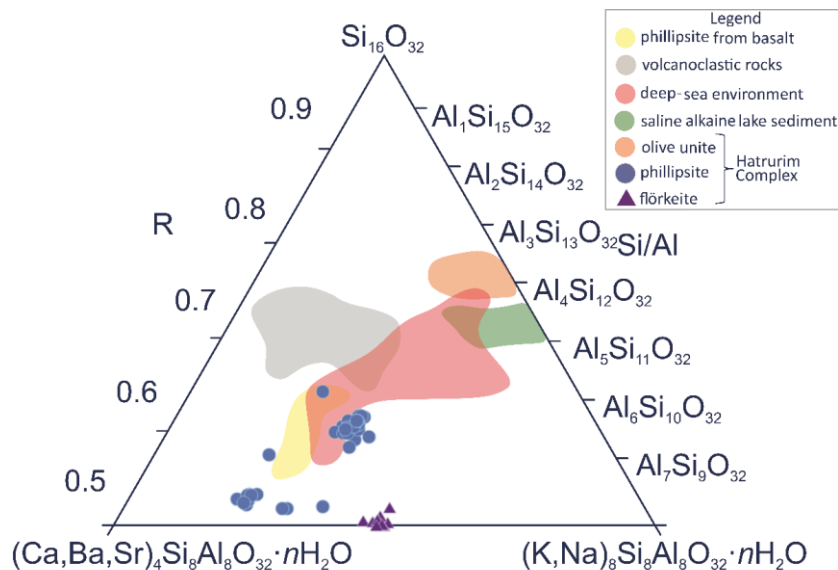

Figure 7 R^{2+} - R^{+} - Si ternary diagram presenting the difference in the chemical composition of phillipsite series minerals depending on geological environments; comparing literature and Hatrurim Complex data

Raman spectroscopy

The Raman spectroscopy investigation of flörkeite and phillipsite-K did not show any significant differences between these two minerals. This observation clearly shows that the principal band at about 470 cm^{-1}, assigned tentatively to modes of four-membered rings, is typical for **PHI**-type structures and is independent of both the order of structure and the Si/Al ratio within the framework (Fig. 8).
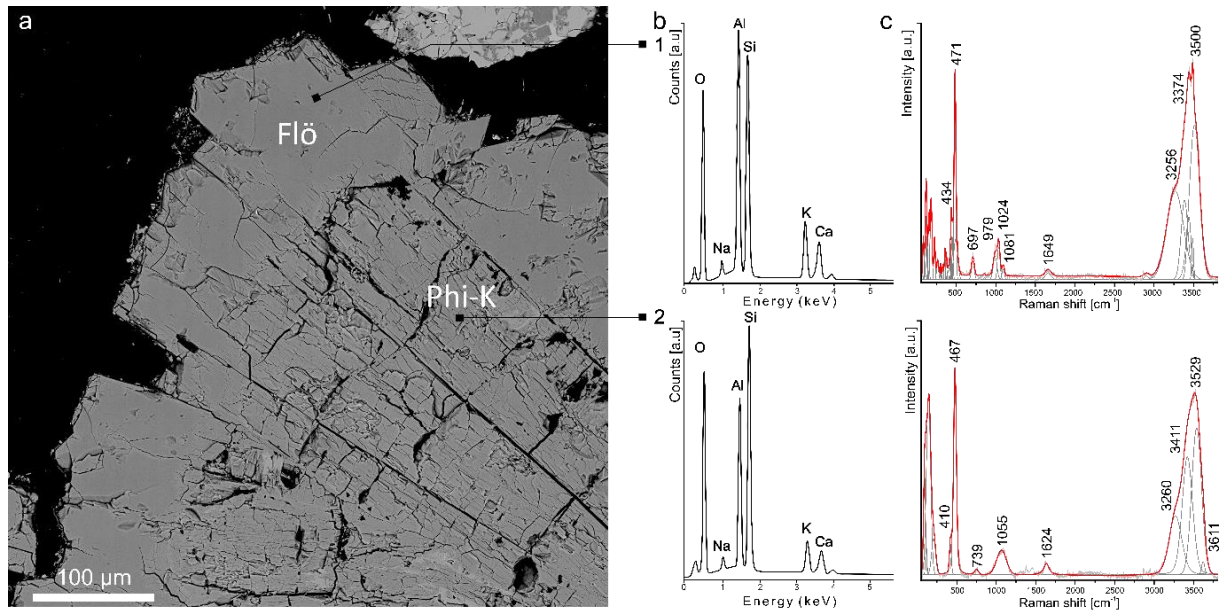
Figure 8 Flörkeite (Flö) and phillipsite-K (Phi-K) in esseneite-latiumite hornfels: (a) BSE image;
(b) EDX spectra; (c) Raman spectra

Single crystal X-ray diffraction

The SC-XRD experiment yielded the triclinic *P*-1 space group and the following unit cell parameters a = 19.9366(2) Å, b = 14.25170(1) Å, c = 8.69350(1) Å, α = 88.2480(1)°, β = 125.0960(1) °, γ = 89.6350(1) °, V = 2019.19(4)Å^3. The structure refinement converged to a value of R_1 = 0.0341%, revealing a **PHI**-type structure with ordered framework cations as well as an ordered extraframework cations and water molecules, which are distributed over the *phi* and *oto* units (Fig. 9). The **PHI** topology is a type of framework occurring in common minerals of the phillipsite series. The structure is built up by double crankshaft chains with the topological symmetry *Cmcm*. However, in the phillipsite series minerals, it is reduced to a monoclinic symmetry as consequence of the distortion caused by the presence of large cations such as K and Ba (Gottardi 1979; Passaglia and Sheppard 2001). Conversely, in flörkeite, the symmetry is first reduced to *B*2/*b* owing to the ordered arrangement of Al and Si within the framework (Gottardi 1979; Lengauer et al. 2009).

26

Subsequently, the ordered distribution of extraframework cations and water molecules in the channels leads to the doubling of the unit cell parameter *a*, resulting in triclinic symmetry (Lengauer et al. 2009). The results obtained for flörkeite from pyrometamorphic rocks of the Hatrurim Complex are in excellent agreement with those obtained on a sample from the type locality in Germany (Lengauer et al. 2009). In conclusion, the main difference between flörkeite and minerals of the phillipsite series is the order of the structure.
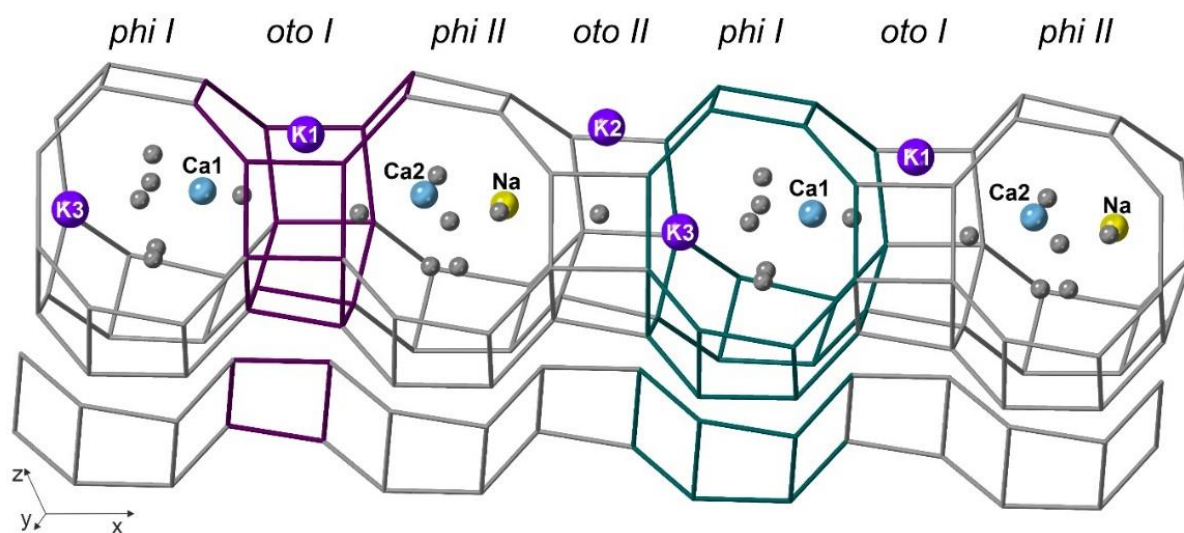
*Figure 98 Top: The kfe channel in the structure of flörkeite with orderly distributed extraframework cations and water molecules. Bottom: The double crankshaft chain building the **PHI**-type structure. The purple and green sticks indicate phi and oto units, respectively.*

Minerals with the **GIS**-type structure

Occurrence and mineral association

During the present project, a new mineral – gismondine-Sr (IMA 2021-043), $Sr_4[Al_8Si_8O_{32}]\cdot 9H_2O$, was discovered and approved by the Commission on New Minerals, Nomenclature and Classification of the International Mineralogical Association (IMA–CNMNC). It is the orthorhombic Sr-analog of gismondine-Ca and the first Sr-dominant zeolite with a **GIS**-type structure. The new zeolite was found in cavities of the gehlenite-wollastonite-garnet hornfels. The low-temperature mineralization was represented by gismondine-Ca, thomsonite-Ca, analcime, and two generations of flörkeite (Fig. 10). Minerals of the tobermorite supergroup were also present. Interestingly, Ba-rich vertumnite occurred as well in this type of rock. Moreover, Ba-rich gismondine and amicite, representing **GIS-**type structure minerals, were found in latiumite-esseneite hornfels and gehlenite-wollastonite-kalsilite paralava, respectively (Fig. 11). In addition, the second worldwide occurrence of gismondine-Sr was reported. The mineral was found in xenolith samples from the Bellerberg volcano in Germany, implying pyrometamorphic conditions similar to those of the formation of rocks from the Hatrurim Basin (Juroszek and Ternes 2022).
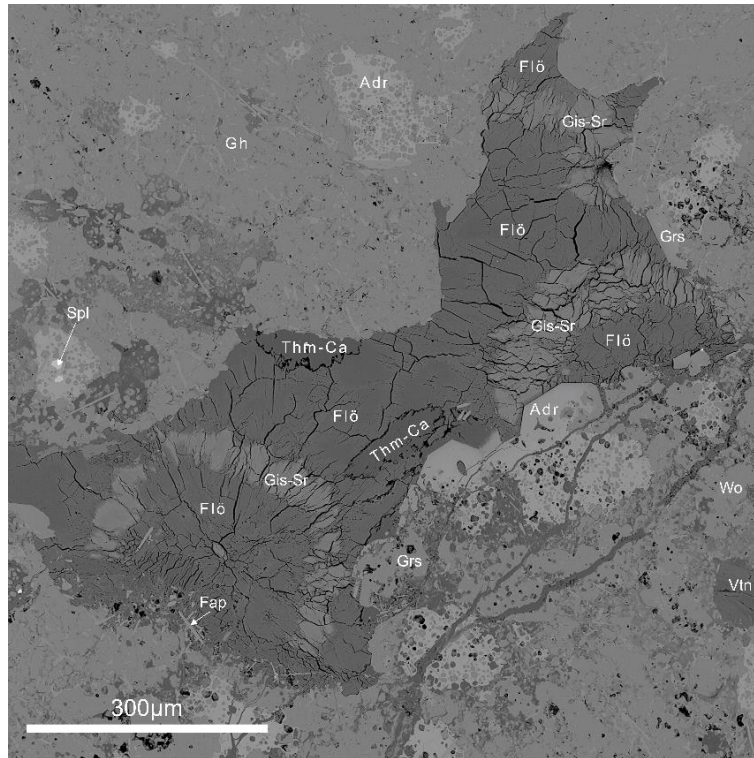
Figure 10 BSE image of gismondine-Sr between two flörkeite generations. Adr – andradite, Fap – fluorapatite, Flö – flörkeite, Gh – gehlenite, Grs – grossular, Spl – spinel, Vtn – vertumnite, Wo – wollastonite. Gis-Sr – gismondine-Sr, Thm-Ca – thomsonite-Ca.
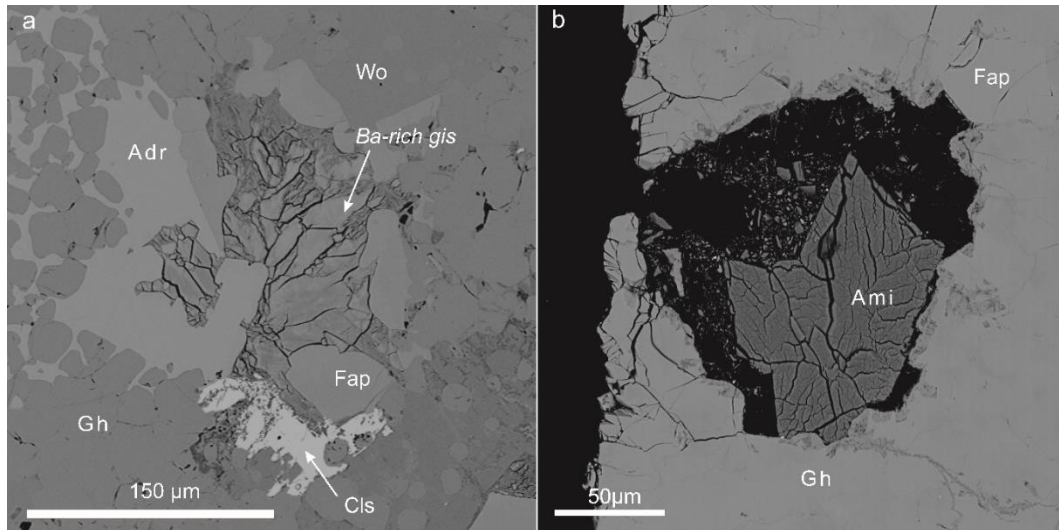
Figure 91 BSE images of (a) Ba-rich gismondine; (b) Amicite in high-temperature pyrometamorphic rocks from the Hatrurim Complex, Israel. Adr – andradite, Ami – amicite, Cls – celsian, Fap – fluorapatite, Gh – gehlenite, Wo – wollastonite, gis – gis-type minerals.

Electron microprobe analyses

Electron microprobe analyses were performed on both, gismondine-Sr from two Israel and Germany, as well as on Ba-rich gismondine and amicite from the Hatrurim Basin. The empirical crystal-chemical formulas presented in Table 2 were calculated on the basis of 16 T-sites.

*Table 2 Empirical crystal-chemical formulas of minerals with **GIS**-type structure from Hatrurim Basin and Bellerberg volcano*

Mineral name	Locality	Empirical crystal-chemical formulas
Gismondine-Sr	Hatrurim Basin (type locality)	$(Sr_{2.02}Ca_{1.09}Ba_{0.02}K_{.0.72}Na_{0.62})_{\Sigma 4.47}[Al_{7.91}Si_{8.09}O_{31.85}]\cdot 9.00H_2O$
Gismondine-Sr	Bellerberg volcano	$(Sr_{1.74}Ca_{1.05}Ba_{0.09}K_{1.56}Na_{0.49})[Al_{7.98}Si_{8.06}O_{32}]\cdot 9.62H_2O$
Ba-rich gismondine	Hatrurim Basin	$(Ba_{1.27}Sr_{1.26}K_{1.25}Ca_{0.73}Na_{0.36})_{\Sigma 4.87}[Al_{7.78}Fe_{0.05}Si_{8.09}O_{32}]\cdot 8.40H_2O$
Amicite	Hatrurim Basin	$(K_{3.73}Na_{3.29}Ca_{0.31})_{\Sigma 7.33}[Al_{8.03}Fe_{0.02}Si_{8.06}O_{32}]\cdot 4.80H_2O$

Based on the empirical crystal-chemical formulas, the end-member of gismondine-Sr was determined as $Sr_4[Al_8Si_8O_{32}]\cdot 18H_2O$ according to the recommended nomenclature for zeolites (Coombs et al. 1997). Noteworthy is a significant K substitution in gismondine-Sr, especially from Germany.

Single crystal X-ray diffraction and structure description

Data acquisition of SC-XRD were carried out on gismondine-Sr crystals from the Hatrurim Complex, Israel and the Bellerberg volcano, Germany. The comparison of unit cell parameters resulting from the measurements is shown in Table 3. Attempts to determine the crystal structures of Ba-rich gismondine and amicite were unsuccessful due to the brittleness and small size of the grains.

Table 3 Comparison of unit cell parameters of gismondine-Sr from the Hatrurim Basin, Israel (type locality) and Bellerberg volcano, Germany

		Hatrurim Complex, Israel	Bellerberg volcano, Germany
Crystal system		orthorhombic	orthorhombic
Space group		$B22_12$	$B22_12$
Unit cell parameters (Å, Å³)	a	14.0256(2)	13.9859(2)
	b	10.45900(10)	10.46830(10)
	c	13.79360(10)	13.7542(2)
	V	2023.44(4)	2013.73(5)

The structure of gismondine-Sr belongs to the **GIS** framework type structures, in which Al and Si are distributed in an orderly manner over the tetrahedral framework sites, in accordance with the Löwenstein rule (Löwenstein 1954). The structure is composed of four-membered rings forming double crankshaft chains. Two systems of chains can be distinguished in the structure, running parallel to [101] and [10-1], respectively. This arrangements leads to the formation of two systems of channels with eight-membered apertures in corresponding directions related by a 2_1 axis (Fig. 12). At the intersection of the channels, the *t-gsm* cage is formed. The cage consists of six four-membered rings and four eight-membered rings, denoted as $4^6 8^4$ (Alberti and Vezzalini 1979). In the gismondine-Sr structure, there are two non-equivalent cages, that contain disorderly distributed extraframework cations and water molecules at partially occupied sites (Fig. 13). In agreement with chemical analyses, Sr is a dominant extraframework cation, besides, Ca, K, Na cations and water molecules were located.
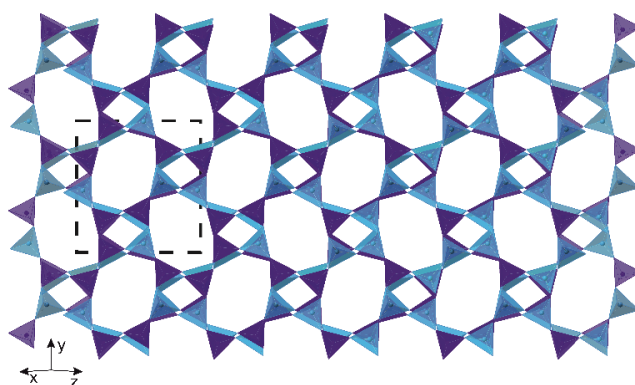
Figure 12 Framework of gismondine-Sr, projection on (101). Silica tetrahedra are dark blue; alumina tetrahedra are light blue; the dashed line indicates the unit cell.
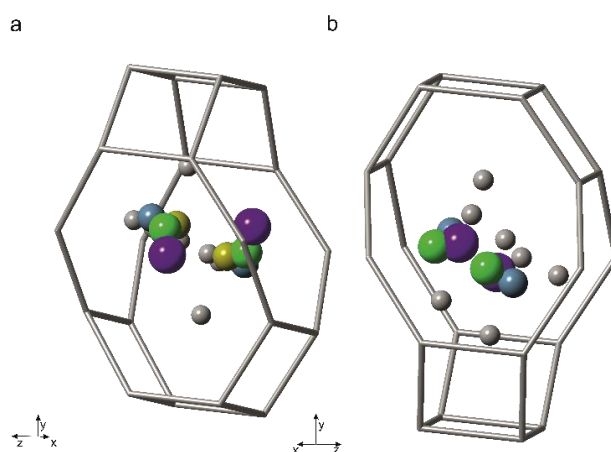
Figure 13 Extraframework cations and water molecules in the two non-equivalent cages in gismondine-Sr structure from the Hatrurim Complex: (a) Cage containing Ca, Na, and K at C1A, C1B, and C1C, respectively; (b) Cage containing Ca and K at C2A and C2B sites. All extraframework sites are partially occupied. Strontium, calcium, potassium, and sodium are represented as green, blue, purple, and yellow spheres, respectively. Gray spheres represent H_2O sites.

Gismondine-Sr crystallises in the orthorhombic space group $B22_12$, which contrasts the monoclinic symmetry (space group $P2_1/c$) of the calcium analog gismondine-Ca. However, framework cations are ordered in both minerals, reducing the topological symmetry (space group $I4_1/amd$, Fig. 14). In the structure of gismondine-Sr, the extraframework cations are disordered, unlike as found in gismondine-Ca. In the latter, the symmetry is reduced to monoclinic due to the ordered arrangement of the extraframework cations. Thus, the orthorhombic symmetry of investigated gismondine-Sr is a consequence of both ordered framework and disordered extraframework cations (Fig. 13, 14). Additionally, a comparison of gismondine-Sr and gismondine-Ca structures has shown that the unit cell parameters of gismondine-Sr are related to the monoclinic setting by the following matrix transformation 101/010/10-1. This corresponds to a rotation of 45° around the y-axis, which leads to an increase in the a and c parameters. As a result, the unit cell volume of gismondine-Sr is almost double that of the monoclinic gismondine-Ca (Vezzalini et al. 1993).
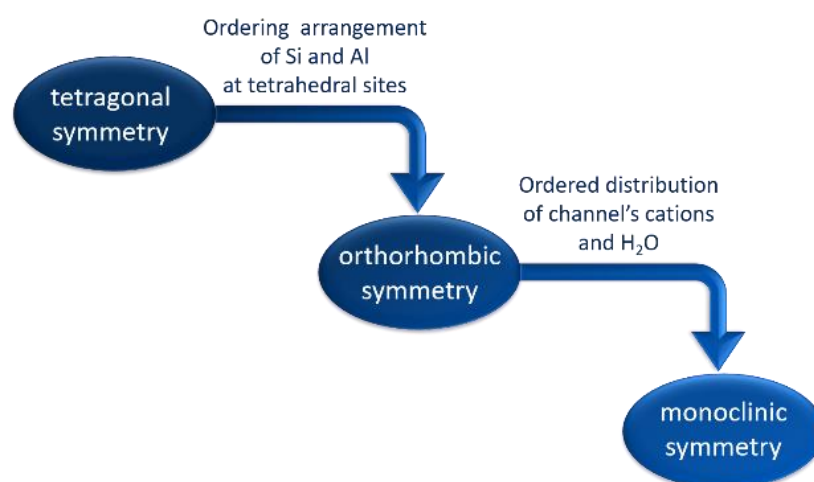
*Figure 14 Scheme of symmetry reduction in **GIS** framework-type structure (Gottardi 1979).*

Interestingly, comprehensive comparison of gismondine minerals revealed that the average T-O-T angle is smaller in the Sr counterpart. Furthermore, the ellipticity ratio of the eight-membered aperture is modified. This modification results from the tilting of the *dcc* around the oxygen – bridging atom which link two four-membered rings in the perpendicular chain (Fig. 3d). It emerges as the tilting of the four-membered rings on oxygen, which plays a role of hinge (Fig. 15). Despite the tilting, no significant changes were observed in the four-membered rings suggesting their quasi-rigid behavior in the structure. Even more interesting is the fact, that a similar ellipticity deformation was observed in partially dehydrated gismondine-Ca. As a result of water loss, a phase transition from the

monoclinic space group $P2_1/c$ to the orthorhombic space group $P2_12_12_1$ took place (Fig. 15c). A comparable deformation of the structure was also observed in the pressure-induced structure of gismondine-Ca (Betti et al. 2007; Ori et al. 2008).
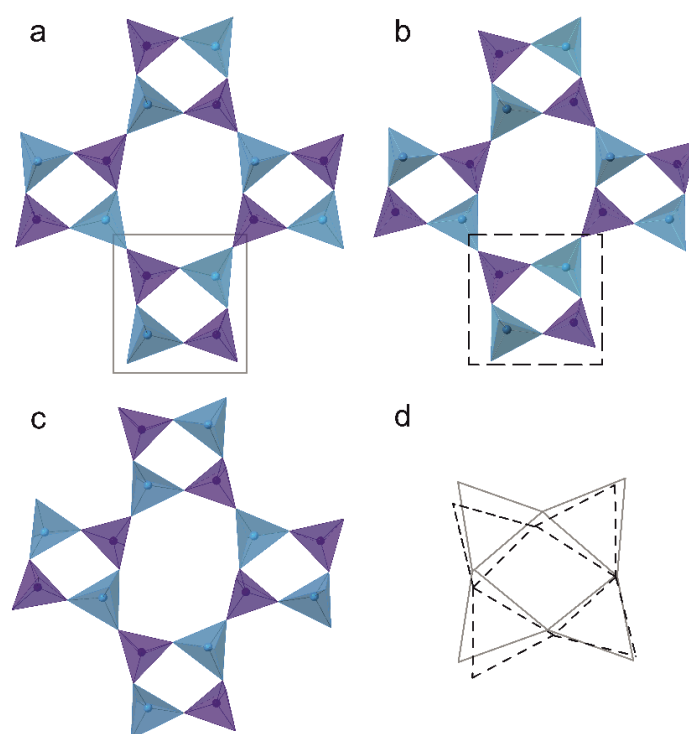
Figure 15 Part of the framework with 8-membered and four-membered rings: (a) monoclinic gismondine-Ca along [001] (Wadoski-Romeijn and Armbruster 2013); (b) gismondine-Sr, projection along [101]; (c) partially dehydrated gismondine-Ca at 75°C along [101] (Wadoski-Romeijn and Armbruster 2013); (d) scheme of overlapping four-membered rings of gismondine-Ca (gray line) and gismondine-Sr (dashed line)

Raman spectroscopy

Raman spectroscopy investigations were conducted on the minerals with **GIS-**type structure found in the pyrometamorphic rocks of the Hatrurim Basin, Israel, and Bellerberg volcano, Germany (Fig. 16). Generally, the Raman spectra of zeolites consist of two overlapping types of bands which can be assigned to the vibrations of the PBUs as well as to modes of the structural framework arising from the links between PBUs. Therefore, the accurate assignment of individual bands to the vibrations is not straightforward. The vibrations of PBUs are independent of the type of three-dimensional framework, whereas the modes arising from the PBUs links are conditional on the type of structure (Auerbach et al. 2003; Čejka 2007; Chester and Derouane 2009). Three regions of framework vibrations 300 - 500 cm^{-1}, 650 - 730 cm^{-1} and 950 - 1100 cm^{-1} can be distinguished in all three spectra. In addition, the presence of water molecules gives rise to additional bands. The bands at ~1650 cm^{-1} correspond to the O-H bending modes, while the bands in the range 3363 - 3585 cm^{-1} represent O-H

stretching vibrations of the water molecules. The framework vibrations part of the spectra show the most prominent band at ~460 cm^{-1}. This peculiar band of **GIS**-type structures has been assigned to the breathing modes of four-membered rings originating from symmetric bending vibrations of T-O-T (Mozgawa 2001; Auerbach et al. 2003; Mozgawa et al. 2005; Čejka 2007; Borodina et al. 2022). On the other hand, bands below 407 cm^{-1} can be attributed to vibrations of eight-membered rings (Mozgawa 2001; Borodina et al. 2022). In the 650 - 724 cm^{-1} region, bands correspond to the symmetric stretching vibrations of T-O-T, whereas 958 - 1079 cm^{-1} are associated with asymmetric stretching modes. However, intra-tetrahedral vibrations can also occur in this region (Auerbach et al. 2003; Gujar et al. 2005; Čejka 2007). The asymmetric bending vibrations of the tetrahedra can be observed at about 700 cm^{-1}. Moreover, asymmetric and symmetric stretching vibrations of T-O can appear between 958-1079 cm^{-1} (Dutta and Del Barco 1988; Dutta et al. 1991; Knops-Gerrits et al. 1997; Yu et al. 2001; Gujar et al. 2005).
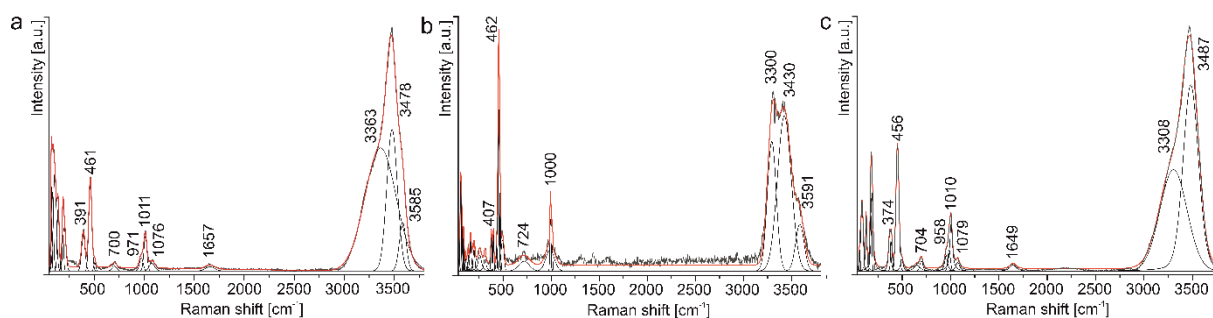
*Figure 16 Raman spectra of zeolites with **GIS**-type structure: (a) gismondine-Sr from Germany; (b) amicite from Israel; (c) Ba-rich gismondine from Israel*

A comparison of Raman spectra of minerals with **GIS**-type structure did not reveal any significant changes in the frequencies of the main bands. It is worth highlighting that the Raman spectra of gismondine-Sr, and gismondine-Ca are almost indistinguishable despite the deformation of the eight-membered rings in the framework of gismondine-Sr. Consequently, the bands at ~460 cm^{-1} are independent of the abovementioned deformation. It confirms the assignment of these bands to the vibrations of the four-membered rings, as these are the only rigid units in the framework that have not changed.

Two series of **GIS**-type minerals – nomenclature implications

As shown above, gismondine-Sr differs significantly from gismondine-Ca. The main differences are symmetry and hydration level. Moreover, the content of monovalent extraframework cations was found to be negligible in gismondine-Ca, whereas gismondine-Sr shows a significant substitution with K (Vezzalini and Oberti 1984). Despite the number of significant differences, the Sr-dominant zeolite with

GIS-type structure was classified as a new end-member of gismondine-Sr Sr$_4$[Al$_8$Si$_8$O$_{32}$]·9H$_2$O, in accordance with the IMA–CNMNC criteria (Coombs et al. 1997). Interestingly, experiments on a synthetic pure Sr-dominant zeolite with **GIS**-type structure, without other extraframework cations, indicate monoclinic symmetry (Allen et al. 2002). As a result of the discovery of gismondine-Sr, IMA–CNMNC established "gismondine" as the name of the series. Consequently, the mineral known previously as gismondine was renamed gismondine-Ca. Moreover, the data presented on Ba-rich gismondine indicates the existence of another potentially new end-member of this series.

The need to review the classification of minerals with **GIS**-type structure is a direct consequence of the approval of gismondine-Sr and garronite-Na (Grice et al. 2016) as a new mineral species. Among the minerals with **GIS**-type structure, only gismondine-Sr, gismondine-Ca, and amicite exhibit a Si/Al ratio equal to one. The data presented in this work indicate a possible solid solution between minerals of the gismondine series and amicite (Fig. 17). Both gismonndine-Sr and gismondine-Ca are divalent cation dominant zeolites. In contrast, amicite is a Na, K dominant mineral. Thus, the scheme of isomorphic substitution from gismondine-Ca to gismondine-Sr can be presented as follows: Ca^{2+} → Sr^{2+}, while the possible heterovalent substitution mechanisms from divalent minerals (D^{2+}) of the gismondine series to monovalent dominant (M$^+$) amicite are more complex. Considering the Si/Al ratio equal to one implies a probable substitution scheme as D^{2+} → 2M$^+$. However, the reduced hydration level must be taken into account. As reported in the literature, K-exchanged gismondine features a lower water content as K ions occupy water sites in the extraframework space due to similar interatomic distances to the oxygens of the framework (Bauer and Baur 1998). It leads to the following substitution mechanism H$_2$O + D^{2+} → 2K$^+$ elucidating lower hydration level and enrichment in K in gismondine-Sr. In view of the above consideration and criteria specified in the IMA–CNMNC recommendation, amicite should be regarded as an alkali end-member of the gismondine series (Coombs et al. 1997).
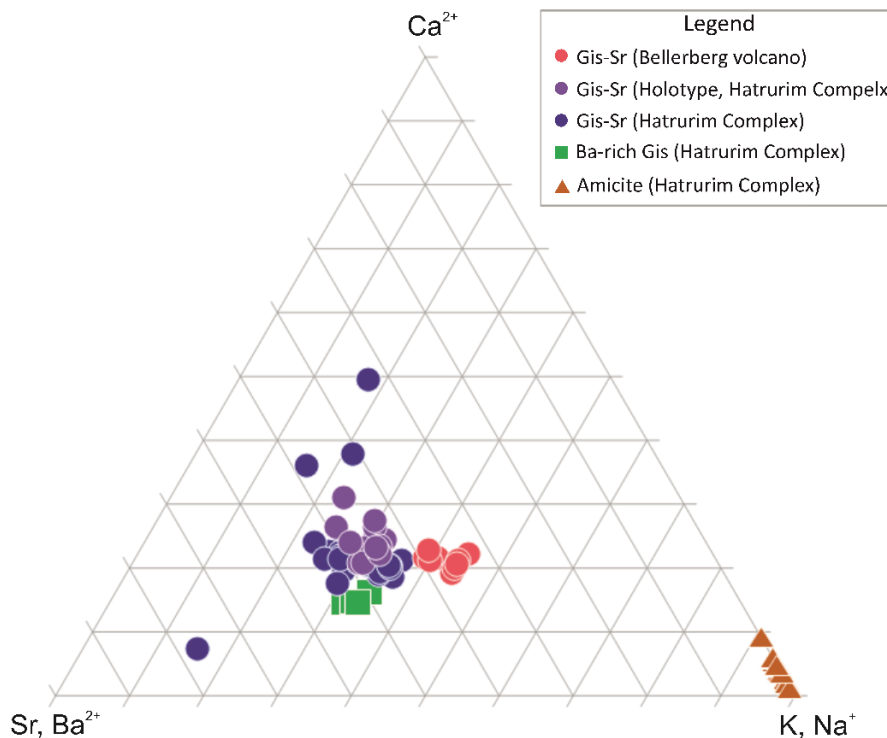
Figure 17 Ternary diagram comparing atomic proportions of extraframework cations in gismondine-Sr (Gis-Sr) from Germany and Israel, as well as Ba-rich gismondine and amicite from Israel.

Following this line of reasoning, the minerals with different Si/Al ratios in terms of the **GIS**-type framework should be reconsidered thoroughly. There are only three known mineral species – garronite-Na, $Na_6[Al_6Si_{10}O_{32}] \cdot 14.3H_2O$, garronite-Ca, $Ca_3[Al_6Si_{10}O_{32}] \cdot 14H_2O$, and gobbinsite, $Na_5[Al_5Si_{11}O_{32}] \cdot 11H_2O$. They are all characterized by higher Si/Al ratios, implying a disordered or only partially ordered framework. However, the distinction between gobbinsite and garronite-Na is disputable. In addition, the discovery of Si-rich garronite (Hirahata et al. 2022), provided additional doubts. These two Na-dominant zeolites were distinguished based on slightly different hydration levels and differences in Si/Al ratios, resulting in various Na content. This leads to the following substitution mechanism: $2M^+ + Al^{3+} \rightarrow M^+ + Si^{4+}$. The insightful analysis of literature data allows to postulate the possible existence of a solid solution series between garronite-Ca and gobbinsite (Fig. 18). Furthermore, in view of the current rules for the nomenclature of natural zeolites (Coombs et al. 1997), it appears highly questionable to consider gobbinsite and garronite-Na as distinct mineral species.
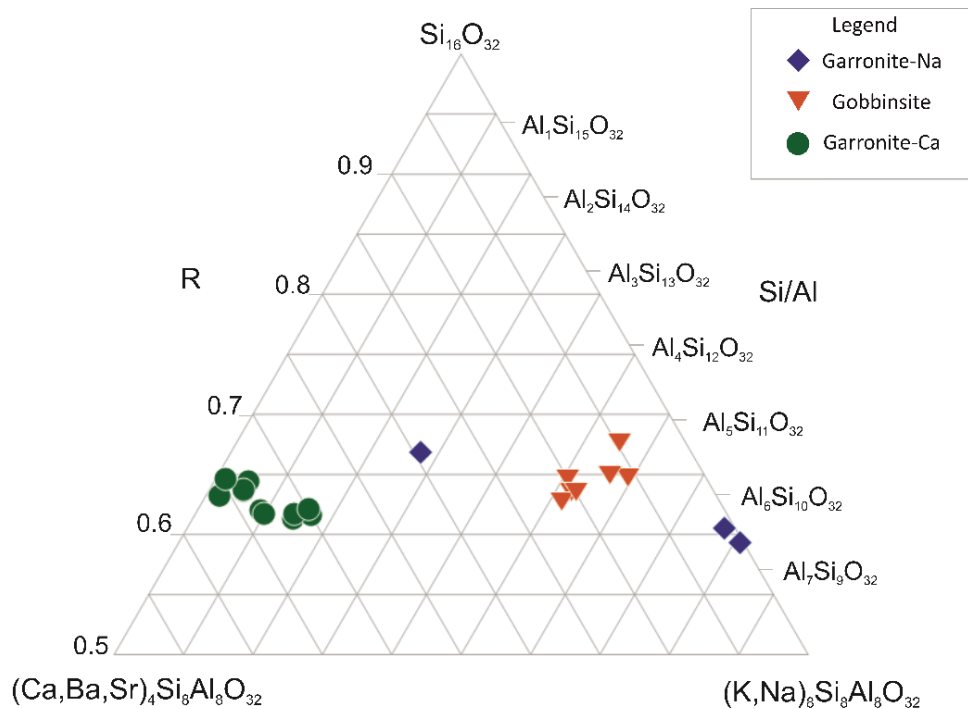
Figure 18 Diagram depicting compositional variations of garronite series and gobbinsite (Walker 1962; Nawaz and Malone 1982; Artioli 1992; Artioli and Foy 1994; Gatta et al. 2010; Kónya and Szakáll 2011; Pauliš et al. 2015; Grice et al. 2016; Popova et al. 2020; Hirahata et al. 2022)

In conclusion, two mineral series can be distinguished within a **GIS** framework type structure. The first series is characterized by a Si/Al ratio equal to one and includes gismondine-Ca, gismondine-Sr, and amicite. These zeolites can be described by the general formula $(M_yD_{0.5(8-y)})[Al_8Si_8O_{32}]\cdot nH_2O$, where $y \leq 8$ is the content of monovalent cations. The second series includes minerals with a Si/Al ratio greater than 1.66. Accordingly, garronite-Ca, gobbinsite and garronite-Na belong to this series. The general formula of this series can be written as $(M_yD_{0.5(x-y)})[Al_xSi_{(16-x)}O_{32}]\cdot nH_2O$, where $x \leq 8$ and refers to the content of Al, while y represents the content of monovalent cations.

37

Conclusions

The most important results of the present project have been published in three articles in scientific journals (Skrzyńska et al. 2022, 2023a, 2023b). Moreover, during this work, the following minerals, previously unknown in the Hatrurim Complex, were identified: amicite, flörkeite, gonnardite, gismondine-Sr, Ba-dominant gismondine, strätlingite, and willhendersonite enriched in Na. In addition, the occurrences of the following minerals were confirmed: vertumnite, thomsonite-Ca, gismondine-Ca, and phillipsite-K and -Ca. Moreover, Sr-enriched thomsonite-Ca was also found.

The present doctoral dissertation (Skrzyńska et al. 2023a, 2023b) showed clearly that in addition to high pressure and dehydration, extraframework cations and water molecules of *t-gsm* in **GIS**-type structures may cause the elliptical deformation of eight-membered rings. Moreover, the rigid behavior of four-membered rings was demonstrated and their relation to the most prominent band at 460 cm^{-1} in the Raman spectra of **GIS**-type crystals.

The occurrence of flörkeite in different types of pyrometamorphic rocks suggests a regional character of relatively uniform conditions of zeolite formation in the Hatrurim Basin (Skrzyńska et al. 2022). The examination of amygdaloidal cavities in pyrometamorphic rocks with stereoscopic and scanning electron microscopes, allowed to identify two distinct stages of zeolite formation. In the first stage, Ca played a major role resulting in the formation of Ca-rich minerals such as vertumnite and thomsonite-Ca. Gonnardite, containing both Na and Ca cations, is rarely found in the Na-enriched corresponding mineralization. Nevertheless, the second stage was dominated by monovalent alkaline metal cations (Na and K). Consequently, flörkeite was formed at the end of the crystallization sequence, as observed in all samples. In general, the zeolites from the high-temperature rocks of the Hatrurim Basin have a low Si/Al ratio as a consequence of their unusually high Al content. In contrast, the zeolites from olive unit rocks, belonging to the "low-grade Hatrurim" (Fig. 1b, Fig. 7), are characterized by a significantly higher Si/Al ratio (Kruszewski et al. 2021). This may be indicative of protolith diversity (Langella et al. 2001; Trian et al. 2012; Novembre et al. 2021). As a general rule, the higher the Al content is in zeolites, the more alkaline their formation environment must have been (Mariner and Surdam 1970; Passaglia et al. 1990; Chipera and Apps 2001; Hay and Sheppard 2001; Langella et al. 2001; Novembre et al. 2021). In the case of high-temperature pyrometamorphic rocks from the Hatrurim Basin, the considerable alkalinity of the zeolite crystallization environment results most likely from the interaction between meteoritic water and clinker-like rocks (Khoury et al.

1992; Milodowski et al. 2011; Vapnik et al. 2019). The presence of such natural cement phases and their reaction with water provokes an increase of the pH value which result in turn in the alteration of rock-forming minerals, such as gehlenite or kalsilite, and the subsequent release of Al. The sharp boundaries between Ba, Sr-rich and Ba, Sr-poor minerals indicate a pronounced variation of the availability of these cations in the crystallization environment (Fig. 9), which presumably origin from rock-forming minerals such as celsian (Fig. 10) or minerals of the fluorapatite-fluorellestadite series (Sokol et al. 2019). Thus, the release of strontium and barium cations could result in local enrichment in these ions and induce the observed diversification of the zeolite mineralization.

References

Alberti, A., and Vezzalini, G. (1979) The crystal structure of amicite, a zeolite. Acta Crystallographica Section B Structural Crystallography and Crystal Chemistry, 35, 2866–2869.

Allen, S., Carr, S., Chapple, A., Dyer, A., and Heywood, B. (2002) Ion exchange in the synthetic gismondine, zeolite MAP. Physical Chemistry Chemical Physics, 4, 2409–2415.

Armbruster, T., and Gunter, E. (2001) Crystal Structures of Natural Zeolites. In Natural Zeolites: Occurrence, properties, applications Vol. 45, pp. 1–68. Mineralogical Society of America; Geochemical Society.

Artioli, G. (1992) The crystal structureof garronite. American Mineralogist, 77, 189–196.

Artioli, G., and Foy, H. (1994) Gobbinsite from Magheramorne Quarry, Northern Ireland. Mineralogical Magazine, 58, 615–620.

Auerbach, S.M., Carrado, K.A., and Dutta, P.K., Eds. (2003) Handbook of zeolite science and technology, 1184 p. M. Dekker, New York.

Baerlocher, C., McCusker, L.B., and Olson, D.H. (2007) Atlas of zeolite framework types, 6th rev. ed., 398 p. Elsevier, Amsterdam.

Bauer, T., and Baur, W.H. (1998) Structural changes in the natural zeolite gismondine (GIS) induced by cation exchange with Ag, Cs, Ba, Li, Na, K and Rb. European Journal of Mineralogy, 10, 133–148.

Bentor, Y.K. (1963) Some unusual minerals from the "Mottled Zone" Complex, Israel. Mineralogical Notes, 48.

Betti, C., Fois, E., Mazzucato, E., Medici, C., Quartieri, S., Tabacchi, G., Vezzalini, G., and Dmitriev, V. (2007) Gismondine under HP: Deformation mechanism and re-organization of the extra-framework species. Microporous and Mesoporous Materials, 103, 190–209.

Biagioni, C., Merlino, S., and Bonaccorsi, E. (2015) The tobermorite supergroup: a new nomenclature. Mineralogical Magazine, 79, 485–495.

Borodina, U., Goryainov, S., Krylova, S., Vtyurin, A., and Krylov, A. (2022) The behavior of zeolites wairakite and phillipsite at high P-T parameters. Spectrochimica Acta Part A: Molecular and Biomolecular Spectroscopy, 273, 120979.

Britvin, S.N., Murashko, M.N., Vapnik, Y., Polekhovsky, Y.S., and Krivovichev, S.V. (2015) Earth's Phosphides in Levant and insights into the source of Archean prebiotic phosphorus. Scientific Reports, 5, 8355.

Britvin, S.N., Vapnik, Y., Polekhovsky, Y.S., Krivovichev, S.V., Krzhizhanovskaya, M.G., Gorelova, L.A., Vereshchagin, O.S., Shilovskikh, V.V., and Zaitsev, A.N. (2019) Murashkoite, FeP, a new terrestrial phosphide from pyrometamorphic rocks of the Hatrurim Formation, South Levant. Mineralogy and Petrology, 113, 237–248.

Britvin, S.N., Murashko, M.N., Vapnik, Y., Polekhovsky, Y.S., Krivovichev, S.V., Krzhizhanovskaya, M.G., Vereshchagin, O.S., Shilovskikh, V.V., and Vlasenko, N.S. (2020) Transjordanite, Ni_2P, a new terrestrial and meteoritic phosphide, and natural solid solutions barringerite-transjordanite (hexagonal Fe_2P–Ni_2P). American Mineralogist, 105, 428–436.

Burg, A., Starinsky, A., Bartov, Y., and Kolodny, Y. (1991) Geology of the Hatrurim Formation ("Mottled Zone") in the Hatrurim basin. Israel Journal of Earth Sciences, 40, 107–124.

Čejka, J., Ed. (2007) Introduction to zeolite science and practice, 3rd rev. ed., 1058 p. Elsevier, Amsterdam ; Boston.

Chester, A.W., and Derouane, E.G., Eds. (2009) Zeolite Chemistry and Catalysis. Springer Netherlands, Dordrecht.

Chipera, S.J., and Apps, J.A. (2001) Geochemical Stability of Natural Zeolites. In Natural Zeolites: Occurrence, properties, applications Vol. 45, pp. 117–157. Mineralogical Society of America; Geochemical Society.

Coombs, D., Alberti, A., Armbruster, T., Artioli, G., Colella, C., Galli, E., Grice, J.D., Liebau, F., Mandarino, J.A., Minato, H., and others (1997) Recommended nomenclature for zeolite minerals: report of the subcommittee on zeolites of the international mineralogical association, commission on new minerals and mineral name. The Canadian Mineralogist, 35, 1571–1606.

Dutta, P.K., and Del Barco, B. (1988) Raman spectroscopy of zeolite A: influence of silicon/aluminum ratio. The Journal of Physical Chemistry, 92, 354–357.

Dutta, P.K., Rao, K.M., and Park, J.Y. (1991) Correlation of Raman spectra of zeolites with framework architecture. The Journal of Physical Chemistry, 95, 6654–6656.

Galuskin, E., Galuskina, I.O., Kamenetsky, V., Vapnik, Y., Kusz, J., and Zieliński, G. (2022) First *In Situ* Terrestrial Osbornite (TiN) in the Pyrometamorphic Hatrurim Complex, Israel. Lithosphere, 2022, 8127747.

Galuskin, E.V., Krüger, B., Galuskina, I.O., Krüger, H., Vapnik, Y., Pauluhn, A., and Olieric, V. (2019) Levantite, $KCa_3(Al_2Si_3)O_{11}(PO_4)$, a new latiumite-group mineral from the pyrometamorphic rocks of the Hatrurim Basin, Negev Desert, Israel. Mineralogical Magazine, 83, 713–721.

Galuskin, E.V., Galuskina, I.O., Vapnik, Y., and Zieliński, G. (2023a) Discovery of "Meteoritic" Layered Disulphides $ACrS2$ (A = Na, Cu, Ag) in Terrestrial Rock. Minerals, 13, 381.

Galuskin, E.V., Kusz, J., Galuskina, I.O., Książek, M., Vapnik, Y., and Zieliński, G. (2023b) Discovery of terrestrial andreyivanovite, FeCrP, and the effect of Cr and V substitution on the low-pressure barringerite-allabogdanite transition. American Mineralogist, 108, 1506–1515.

Galuskina, I.O., Galuskin, E.V., Vapnik, Y., Prusik, K., Stasiak, M., Dzierżanowski, P., and Murashko, M. (2017a) Gurimite, $Ba_3(VO_4)_2$ and hexacelsian, $BaAl_2Si_2O_8$ – two new minerals from schorlomite-rich paralava of the Hatrurim Complex, Negev Desert, Israel. Mineralogical Magazine, 81, 1009–1019.

Galuskina, I.O., Galuskin, E.V., Pakhomova, A.S., Widmer, R., Armbruster, T., Krüger, B., Grew, E.S., Vapnik, Y., Dzieraẓanowski, P., and Murashko, M. (2017b) Khesinite, $Ca_4Mg_2Fe^{3+}_{10}O_4[(Fe^{3+}_{10}Si_2)O_{36}]$, a new rhönite-group (sapphirine supergroup) mineral from the Negev Desert, Israel– natural analogue of the SFCA phase. European Journal of Mineralogy, 101–116.

Gatta, G.D., Birch, W.D., and Rotiroti, N. (2010) Reinvestigation of the crystal structure of the zeolite gobbinsite: A single-crystal X-ray diffraction study. American Mineralogist, 95, 481–486.

Geller, Y.I., Burg, A., Halicz, L., and Kolodny, Y. (2012) System closure during the combustion metamorphic "Mottled Zone" event, Israel. Chemical Geology, 334, 25–36.

Gottardi, G. (1979) Topologic symmetry and real symmetry in framework silicates. Mineralogy and Petrology, 26, 39–50.

Gottardi, G., and Galli, E. (1985) Natural zeolites.

Grapes, R. (2010) Pyrometamorphism. Springer Berlin Heidelberg, Berlin, Heidelberg.

Grice, J.D., Rowe, R., and Poirier, G. (2016) Garronite-Na, A New Zeolite Species From Mont Saint-Hilaire, Québec. The Canadian Mineralogist, 54, 1549–1562.

Gross, S. (1977) The mineralogy of the Hatrurim Formation, Israel. Geological Survey of Israel Bulletin, 70.

Gujar, A.C., Moye, A.A., Coghill, P.A., Teeters, D.C., Roberts, K.P., and Price, G.L. (2005) Raman investigation of the SUZ-4 zeolite. Microporous and Mesoporous Materials, 78, 131–137.

Gur, D., Steinitz, G., Kolodny, Y., Starinsky, A., and McWilliams, M. (1995) 40Ar/39Ar dating of combustion metamorphism ("Moltted Zone", Israel). Chemical Geology, 122.

Hay, R.L., and Sheppard, R.A. (2001) Occurrence of Zeolites in Sedimentary Rocks: An Overview. In Natural Zeolites: Occurrence, properties, applications Vol. 45, pp. 217–232. Mineralogical Society of America; Geochemical Society.

Hirahata, Y., Kobayashi, S., and Nishido, H. (2022) Silica-Rich Garronite-Na From Hirado Island, Nagasaki Prefecture, Japan. The Canadian Mineralogist, 60, 91–99.

Hirsch, F., Burg, A., and Avani, Y. (2008) Geological Map of Israel 1:50 000 Arade Sheet. Geological Survey.

Juroszek, R., and Ternes, B. (2022) Crystal chemistry and Raman spectroscopy study of bennesherite, $Ba_2Fe^{2+}Si_2O_7$, and rare accessory Ba minerals from Caspar quarry, Bellerberg volcano, Germany. Mineralogical Magazine, 86, 777–791.

Juroszek, R., Krüger, B., Banasik, K., Vapnik, Y., and Galuskina, I. (2018) Raman spectroscopy and structural study of baryte-hashemite solid solution from pyrometamorphic rocks of the Hatrurim Complex, Israel. Spectrochimica Acta Part A: Molecular and Biomolecular Spectroscopy, 205, 582–592.

Juroszek, R., Krüger, B., Galuskina, I., Krüger, H., Vapnik, Y., and Galuskin, E. (2020a) Siwaqaite, $Ca_6Al_2(CrO_4)_3(OH)_{12}\cdot26H_2O$, a new mineral of the ettringite group from the pyrometamorphic Daba-Siwaqa complex, Jordan. American Mineralogist, 105, 409–421.

Juroszek, R., Czaja, M., Lisiecki, R., Krüger, B., Hachuła, B., and Galuskina, I. (2020b) Spectroscopic and structural investigations of blue afwillite from Ma'ale Adummim locality, Palestinian Autonomy. Spectrochimica Acta Part A: Molecular and Biomolecular Spectroscopy, 227, 117688.

Kampf, A.R., Gu, X., Yang, H., Ma, C., and Marty, J. (2024) Ebnerite and epiebnerite: NH_4ZnPO_4 dimorphs with zeolite-type frameworks from the Rowley mine, Arizona, USA. Mineralogical Magazine, 1–23.

Khoury, H.N., Salameh, E., Clark, I.D., Fritz, P., Bajjali, W., Milodowski, A.E., Cave, M.R., and Alexander, W.R. (1992) A natural analogue of high pH cement pore waters from the Maqarin area of northern Jordan. I: introduction to the site. Journal of Geochemical Exploration, 46, 117–132.

Knops-Gerrits, P.-P., De Vos, D.E., Feijen, E.J.P., and Jacobs, P.A. (1997) Raman spectroscopy on zeolites. Microporous Materials, 8, 3–17.

Kolodny, Y., Burg, A., Geller, Y.I., Halicz, L., and Zakon, Y. (2014) Veins in the combusted metamorphic rocks, Israel; Weathering or a retrograde event? Chemical Geology, 385, 140–155.

Kónya, P., and Szakáll, S. (2011) Occurrence, composition and paragenesis of the zeolites and associated minerals in the alkaline basalt of a maar-type volcano at Haláp Hill, Balaton Highland, Hungary. Mineralogical Magazine, 75, 2869–2885.

Kruszewski, Ł., Palchik, V., Vapnik, Y., Nowak, K., Banasik, K., and Galuskina, I. (2021) Mineralogical, Geochemical, and Rock Mechanic Characteristics of Zeolite-Bearing Rocks of the Hatrurim Basin, Israel. Minerals, 11, 1062.

Krzątała, A., Krüger, B., Galuskina, I., Vapnik, Y., and Galuskin, E. (2020) Walstromite, $BaCa_2(Si_3O_9)$, from Rankinite Paralava within Gehlenite Hornfels of the Hatrurim Basin, Negev Desert, Israel. Minerals, 10, 407.

Krzątała, A., Krüger, B., Galuskina, I., Vapnik, Y., and Galuskin, E. (2022) Bennesherite, $Ba_2Fe^{2+}Si_2O_7$: A new melilite group mineral from the Hatrurim Basin, Negev Desert, Israel. American Mineralogist, 107, 138–146.

Krzątała, A., Skrzyńska, K., Cametti, G., Galuskina, I., Vapnik, Y., and Galuskin, E. (2023) Fluoralforsite, $Ba_5(PO_4)_3F$ – a new apatite-group mineral from the Hatrurim Basin, Negev Desert, Israel. Mineralogical Magazine, 87, 866–877.

Langella, A., Cappelletti, P., and de' Gennaro, M. (2001) Zeolites in Closed Hydrologic Systems. In Natural Zeolites: Occurrence, properties, applications Vol. 45, pp. 235–257. Mineralogical Society of America; Geochemical Society.

Lengauer, C.L., Kolitsch, U., and Tillmanns, E. (2009) Flörkeite, $K_3Ca_2Na[Al_8Si_8O_{32}]\cdot12H_2O$, a new phillipsite-type zeolite from the Bellerberg, East Eifel volcanic area, Germany. European Journal of Mineralogy, 21, 901–913.

Loewenstein, W. (1954) The distribution of aluminum in the tetrahedra of silicates and aluminates. American Mineralogist, 39, 92–69.

Mariner, R.H., and Surdam, R.C. (1970) Alkalinity and Formation of Zeolites in Saline Alkaline Lakes. Science, 170, 977–980.

Matthews, A., and Gross, S. (1980) Petrologic Evolution of the "Mottled Zone" (Hatrurim) Metamorphic Complex of Israel. Israel Journal of Earth Sciences, 29, 93–106.

Milodowski, A.E., Trotignon, L., Khoury, H., Salameh, E., Arnal, N., Bienvenu, P., Bulle, C., Chenery, S.R., Crouzet N., Fontanini, L., and others (2011) The Analogue Cement ZOne (ACZ). In A natural analog study of cement buffered, hyperalkaline groundwaters and their interaction with a Repository Host Rock IV: An examination of the Khushaym Matruk (central Jordan) and Maqarin (northern Jordan) sites, chapter 4. NDA, Moors Row, U.K.

Mozgawa, W. (2001) The relation between structure and vibrational spectra of natural zeolites. Journal of Molecular Structure, 596, 129–137.

Mozgawa, W., Jastrzębski, W., and Handke, M. (2005) Vibrational spectra of D4R and D6R structural units. Journal of Molecular Structure, 744–747, 663–670.

Nawaz, R., and Malone, J.F. (1982) Gobbinsite, a new zeolite mineral from Co. Antrim, N. Ireland. Mineralogical Magazine, 46, 365–369.

Novembre, D., Gimeno, D., Cappelletti, P., and Graziano, S.F. (2021) A case study of zeolitization process: "Tufo Rosso a Scorie Nere" (Vico volcano, Italy): inferences for a general model. European Journal of Mineralogy, 33, 315–328.

Novikov, I., Vapnik, Y., and Safonova, I. (2013) Mud volcano origin of the Mottled Zone, South Levant. Geoscience Frontiers, 4, 597–619.

Ori, S., Quartieri, S., Vezzalini, G., and Dmitriev, V. (2008) Pressure-induced over-hydration and water ordering in gismondine: A synchrotron powder diffraction study. American Mineralogist, 93, 1393–1403.

Passaglia, E., and Sheppard, A. (2001) The Crystal Chemistry of Zeolites. In Natural Zeolites: Occurrence, properties, applications Vol. 45, pp. 69–116. Mineralogical Society of America; Geochemical Society.

Passaglia, E., Vezzalini, G., and Carnevali, R. (1990) Diagenetic chabazites and phillipsites in Italy: crystal chemistry and genesis. European Journal of Mineralogy, 2, 827–840.

Pauliš, P., Hrůzek, L., Janeček, O., Sejkora, J., Malíková, R., and Pour, O. (2015) Tschernichite, garronite-Ca and associated zeolite mineralization from Jehly u České Kamenice (Česká republika). Bulletin mineralogicko-petrologického oddělení Národního muzea v Praze, 23, pp. 147–170.

Popova, V.I., Kasatkin, A.V., Popov, V.A., Nikandrov, S.N., Makagonov, E.P., Kuznetsov, A.M., and Škoda, R. (2020) Zeolites in Pegmatites and Late Veinlets of the Vishnevogorsky Alkaline-Carbonatite Complex (South Urals). МИНЕРАЛОГИЯ (MINERALOGY), 6, 1–16.

Seryotkin, Y.V., Sokol, E.V., Kokh, S.N., and Sharygin, V.V. (2019) Natural bentorite – Cr^{3+} derivate of ettringite: determination of crystal structure. Physics and Chemistry of Minerals, 46, 553–570.

Sharygin, V.V., Sokol, E.V., and Vapnik, Ye. (2008) Minerals of the pseudobinary perovskite-brownmillerite series from combustion metamorphic larnite rocks of the Hatrurim Formation (*Israel*). Russian Geology and Geophysics, 49, 709–726.

Sharygin, V.V., Lazic, B., Armbruster, T.M., Murashko, M.N., Wirth, R., Galuskina, I.O., Galuskin, E.V., Vapnik, Y., Britvin, S.N., and Logvinova, A.M. (2013) Shulamitite $Ca_3TiFe^{3+}AlO_8$ - a new perovskite-related mineral from Hatrurim Basin, Israel. European Journal of Mineralogy, 25, 97–111.

Skrzyńska, K., Cametti, G., Galuskina, I.O., Vapnik, Y., and Galuskin, E. (2022) Flörkeite, $(K_3Ca_2Na)[Al_8Si_8O_{32}]\cdot12H_2O$: A Rare Zeolite from Pyrometamorphic Rocks of the Hatrurim Complex, Israel. Lithosphere, 2022, 1343791.

Skrzyńska, K., Cametti, G., Galuskina, I.O., Vapnik, Y., and Galuskin, E.V. (2023a) Gismondine-Sr, $Sr_4(Al_8Si_8O_{32})\cdot H_2O$, a new strontium dominant, orthorhombic zeolite of the gismondine series from the Hatrurim Complex, Israel. American Mineralogist, 108, 249–258.

Skrzyńska, K., Cametti, G., Juroszek, R., Schäfer, C., and Galuskina, I. (2023b) New data on minerals with the GIS framework-type structure: gismondine-Sr from the Bellerberg volcano, Germany, and amicite and Ba-rich gismondine from the Hatrurim Complex, Israel. Mineralogical Magazine, 1–33.

Smith, J.V. (1988) Topochemistry of zeolites and related materials. 1. Topology and geometry. Chemical Reviews, 88, 149–182.

Sokol, E., Kokh, S., Sharygin, V., Danilovsky, V., Seryotkin, Y., Liferovich, R., Deviatiiarova, A., Nigmatulina, E., and Karmanov, N. (2019) Mineralogical Diversity of Ca_2SiO_4-Bearing Combustion Metamorphic Rocks in the Hatrurim Basin: Implications for Storage and Partitioning of Elements in Oil Shale Clinkering. Minerals, 9, 465.

Sokol, E.V., Novikov, I.S., Vapnik, Ye., and Sharygin, V.V. (2007) Gas fire from mud volcanoes as a trigger for the appearance of high-temperature pyrometamorphic rocks of the Hatrurim Formation (Dead Sea area). Doklady Earth Sciences, 413, 474–480.

Sokol, E.V., Novikov, I.S., Zateeva, S.N., Sharygin, V.V., and Vapnik, Ye. (2008) Pyrometamorphic rocks of the spurrite-merwinite facies as indicators of hydrocarbon discharge zones (the Hatrurim formation, Israel). Doklady Earth Sciences, 420, 608–614.

Sokol, E.V., Kokh, S.N., Vapnik, Y., Thiery, V., and Korzhova, S.A. (2014) Natural analogs of belite sulfoaluminate cement clinkers from Negev Desert, Israel. American Mineralogist, 99, 1471–1487.

Trian, J.M.R., Herrera, J.F.R., Rios, C.A.R., Castellanos, O.M.A., Henao, J.A.M., Williams, D.C., and Roberts, C.L. (2012) Natural zeolites filling amygdales and veins in basalts from the British Tertiary Igneous Province on the Isle of Skye, Scotland. Earth Sciences Research Journal, 16.

Vapnik, Y., Sharygin, V.V., Sokol, E.V., and Shagam, R. (2007) Paralavas in a combustion metamorphic complex: Hatrurim Basin, Israel. The Geological Society of America Reviews in Engineering Geology, XVIII, pp. 1–21.

Vapnik, Y., Galuskina, I.O., Palchik, V., Sokol, E.V., Galuskin, E.V., Lindsley-Griffin, N., and Stracher, G.B. (2015) Stone-Tool Workshops of the Hatrurim Basin, Israel. In Coal and Peat Fires: A Global Perspective pp. 281–316. Elsevier.

Vapnik, Y., Galuskin, E.V., Galuskina, I.O., Kusz, J., Stasiak, M., Krzykawski, T., and Dulski, M. (2019) Qatranaite, $CaZn_2(OH)_6 \cdot 2H_2O$: a new mineral from altered pyrometamorphic rocks of the Hatrurim Complex, Daba-Siwaqa, Jordan. European Journal of Mineralogy, 31, 575–584.

Vezzalini, G., and Oberti, R. (1984) The crystal chemistry of gismondines: the non-existence of K-rich gismondines. Bulletin de Minéralogie, 107, 805–812.

Vezzalini, G., Quartieri, S., and Alberti, A. (1993) Structural modifications induced by dehydration in the zeolite gismondine. Zeolites, 13, 34–42.

Wadoski-Romeijn, E., and Armbruster, T. (2013) Topotactic transformation and dehydration of the zeolite gismondine to a novel Ca feldspar structure. American Mineralogist, 98, 1988–1997.

Walker, G.P.L. (1962) Garronite, a new zeolite, from Ireland and Iceland. Mineralogical Magazine and Journal of the Mineralogical Society, 33, 173–186.

Warr, L. N. (2021) IMA–CNMNC approved mineral symbols. Mineralogical Magazine, 85, 291–320.

Yang, H., Gu, X., Gibbs, R.B., and Downs, R.T. (2023) Loomisite, $Ba[Be_2P_2O_8] \cdot H_2O$, the first natural example with the zeolite **ABW**-type framework, from Keystone, Pennington County, South Dakota, USA. Mineralogical Magazine, 87, 79–85.

Yu, Y., Xiong, G., Li, C., and Xiao, F.-S. (2001) Characterization of aluminosilicate zeolites by UV Raman spectroscopy. Microporous and Mesoporous Materials, 46, 23–34.

Contributions of the co-authors

Herein, the doctoral dissertation includes three scientific papers addressing the topic of zeolite mineralization of pyrometamorphic rocks from the Hatrurim Basin, Israel. Below are presented the contributions of the PhD candidate in the studies confirmed by the co-authors (Table 4, 5, 6).

Article 1

Skrzyńska Katarzyna, Cametti Georgia, Galuskina Irina, Vapnik Yevgeny, Galuskin Evgeny (2022) Flörkeite, $(K_3Ca_2Na)[Al_8Si_8O_{32}]\cdot12H_2O$: A Rare Zeolite from Pyrometamorphic Rocks of the Hatrurim Complex, Israel; *Lithosphere*, volume 2022, article ID 1343791, DOI 10.2113/2022/1343791

5-year IF 3.0

List of scientific journals of Ministry of Science and Higher Education of Poland 140 pkt

Contribution of the PhD candidate: Field work, research using a scanning electron microscope, including a description of mineral association; preparation of single crystals for diffraction studies; interpretation of structural data; spectroscopic investigation and their interpretation of the results, preparation of samples for EMPA measurements and analysis of the obtained data; sample preparation for EMPA measurements and analysis of the obtained data; manuscript writing, acting as a corresponding author.

Table 4 Percentage contribution of authors

Author	Percentage	Signature
Skrzyńska Katarzyna	**70%**	
Cametti Georgia	15%	
Galuskina Irina	5%	
Vapnik Yevgeny	5%	
Galuskin Evgeny	5%	

Article 2
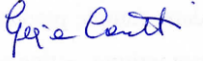
Skrzyńska Katarzyna, Cametti Georgia, Galuskina Irina, Vapnik Yevgeny, Galuskin Evgeny (2023) Gismondine, $Sr_4(Al_8Si_8O_{32})\cdot 9H_2O$, a new strontium dominant, orthorhombic zeolite of the gismondine series from the Hatrurim Complex, Israel; *American Mineralogist*, 2023, volume 108, pages 149–258, DOI 10.2138/am-2022-8376

5-year IF 3.5 List

List of scientific journals of Ministry of Science and Higher Education of Poland 100 pkt

Contribution of the PhD candidate: investigation using SEM-EDX, including description of mineral association; preparation of single crystals for the diffraction experiments; interpretation of the structural data; spectroscopic investigation and their interpretation of the results; sample preparation for EMPA measurements and analysis of the obtained data; manuscript writing, acting as a corresponding author.

Table 5 Percentage contribution of authors

Author	Percentage	Signature
Skrzyńska Katarzyna	**70%**	
Cametti Georgia	15%	
Galuskina Irina	5%	
Vapnik Yevgeny	5%	
Galuskin Evgeny	5%	
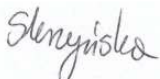
Skrzyńska Katarzyna, Cametti Georgia, Juroszek Rafał, Schäfer Christof, Galuskina Irina (2023) New data on minerals with the GIS framework-type structure: gismondine-Sr from the Bellerberg volcano, Germany, and amicite and Ba-rich gismondine from the Hatrurim Complex, Israel; *Mineralogical Magazine*, 2023, 87(3), 443–454, DOI 10.1180/mgm.2023.27

5-year IF 2.1

List of scientific journals of Ministry of Science and Higher Education of Poland 100 pkt

Contribution of the PhD candidate: investigation using SEM-EDX, including description of mineral association; preparation of single crystals for the diffraction experiments; conducting SC-XRD experiments during the internship at University of Bern in Switzerland in terms of Preludium Bis project of Polish National Agency for Academic Exchange; assisting in structure solution and refinement; interpretation of the structured data; spectroscopic investigation and their interpretation of the results; sample preparation for EMPA measurements and analysis of the obtained data; manuscript writing, acting as a corresponding author.

Table 6 Percentage contribution of authors

Author	Percentage	Signature
Skrzyńska Katarzyna	70%	
Cametti Georgia	15%	
Juroszek Rafał	5%	
Schäfer Christof	5%	
Galuskina Irina	5%	

Lithosphere

Research Article

Flörkeite, $(K_3Ca_2Na)[Al_8Si_8O_{32}]\cdot 12H_2O$: A Rare Zeolite from Pyrometamorphic Rocks of the Hatrurim Complex, Israel

Katarzyna Skrzyńska [ID],[1] **Georgia Cametti** [ID],[2] **Irina O. Galuskina** [ID],[1] **Yevgeny Vapnik,**[3] **and Evgeny Galuskin** [ID][1]

[1]*University of Silesia, Faculty of Natural Sciences, Institute of Earth Sciences, Sosnowiec 41-200, Poland*
[2]*University of Bern, Institute of Geological Science, Bern 3012, Switzerland*
[3]*Ben-Gurion University of the Negev, Department of Geological and Environmental Sciences, Beer Sheva 84105, Israel*

Correspondence should be addressed to Katarzyna Skrzyńska; katarzyna.k.nowak@us.edu.pl

Flörkeite, a rare zeolite with **PHI** (phillipsite) framework type, was found in numerous amygdaloidal voids in pyrometamorphic rocks of the Hatrurim Basin, Hatrurim Complex, Israel. This is the second reported occurrence of flörkeite previously found in a Ca-rich xenolith from a quarry at the Bellerberg volcano near Ettringen, East Eifel volcanic area, Germany. The mineral with the empirical crystal chemical formula $(K_{2.91}Ca_{2.00}Na_{0.91})[Al_{7.96}Si_{8.04}O_{31.94}]\cdot 12H_2O$ (P-1, no. 2, $a = 19.9366\,(2)$, $b = 14.2517\,(1)$, $c = 8.89350\,(10)$ Å, $\alpha = 88.2480\,(1)$, $\beta = 125.0960\,(10)$, $\gamma = 89.6350\,(10)$, $V = 2019.19\,(4)$ Å^3, and $R = 3.41\%$) did not show significant differences with respect to that of the type locality. The Raman spectrum of flörkeite is here reported for the first time. No significant differences are noticed compared to phillipsite-K. The main band $\sim 470\,cm^{-1}$, characteristic of the **PHI**-type structures, is independent on framework order and Si/Al ratio. The zeolite mineralization of amygdules in pyrometamorphic rocks results from meteoric water circulations in Al-rich rocks during their cooling. The crystallization sequence of zeolite corresponds to the Ca/(K+Na) ratio decrease. Flörkeite formed at the end of a low-temperature crystallization sequence, indicating the predominant role of potassium in crystallization. The occurrence of flörkeite in different pyrometamorphic rocks implies the relatively uniform, regional mineral-forming conditions, and open hydrologic system of zeolitization. In pyrometamorphic rocks of the Hatrurim Basin, the process of zeolitization is characterized by low silica activity and high pH conditions.

1. Introduction

Zeolites occur in diverse geological environments. Generally, their origin can be sedimentary or hydrothermal [1–4]. It is widely known that most zeolites are formed from low-temperature alterations due to water penetrating into rocks. Minerals belonging to the phillipsite (-K, -Na, and -Ca) series are one of the most widespread zeolites. The most frequent is phillipsite-K, which is present in volcanic rocks and in diagenetically altered sediments and deep-sea sediments [5, 6]. The chemical composition of the phillipsite-type minerals depends on the protolith composition. Therefore, they exhibit a wide variation of the extraframework population, reflected in the wide R ($R=Si/(Si+Al+Fe^{3+})$) range from 0.5 to 0.77 [7]. The zeolite, with **PHI** (phillipsite) framework

type, characterized by the highest aluminum content is flörkeite $(K_3Ca_2Na)[Al_8Si_8O_{32}]\cdot 12H_2O$, which stands out because of the completely ordered framework and extraframework sites. Up to now, flörkeite has only been known in a Ca-rich xenolith from a quarry at Bellerberg volcano, East Eifel volcanic area, Germany [8].

Here, we report on the second occurrence of flörkeite, which was found in numerous amygdaloidal voids of the pyrometamorphic rocks from the Hatrurim Basin, Negev desert, Israel. The pyrometamorphic Hatrurim Complex in Israel has been the subject of many mineralogical studies over the last ten years. However, the research has focused chiefly on high-temperature rather than low-temperature minerals. Recent studies have shown the wide zeolites diversity and great potential for the occurrence of rare and new
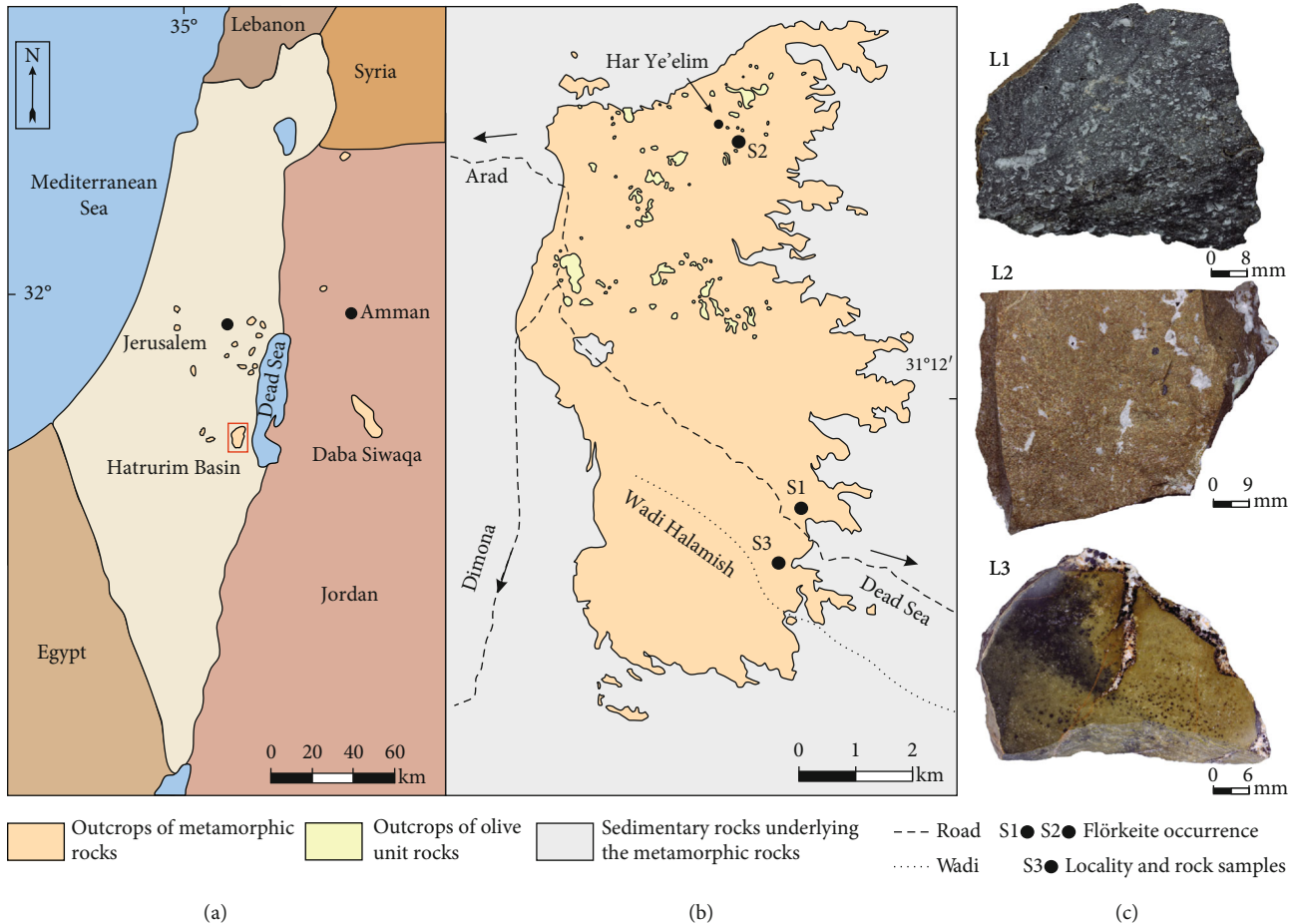
Figure 1: (a) Schematic map of the pyrometamorphic rocks outcrops in Israel, Palestinian Autonomy and Jordan; fragment outlined by frame is magnified in (b); (b) Hatrurim Basin outcrops with marked localities of sampling and olive unit outcrops, which is a major unit subjected to zeolitization; (c) rock samples: L1, gehlenite-wollastonite-kalsilite paralava with amygdaloidal texture from Zuk Tamrur; L2, esseneite-latiumite hornfels from Har Ye'elim; L3, gehlenite-wollastonite-garnet hornfels with paralava part from Halamish wadi (modified from Geological Map of Israel 1: 50 000, Arad sheet, [27]).

zeolites [9]. This paper provides data on the chemical composition, structure, and Raman spectroscopy of a rare zeolite—flörkeite—from the rocks of the Hatrurim Complex. Moreover, zeolite genesis is discussed.

2. Geological Setting

The Hatrurim Complex, commonly called the Mottled Zone because of its multicolored appearance, is a complex of pyrometamorphic rocks on both sides of the Dead Sea Transform Fault and widespread over the territory of Israel, Palestine Autonomy, and Jordan (Figure 1(a)) [10–13]. It consists of high-temperature rocks and their alteration products. The high-temperature, low-pressure rocks occur as irregular bodies embedded in light-colored, low-temperature calcium-hydrosilicate rocks [9, 14]. The genesis of the Hatrurim Complex is still under debate. Until now, two hypotheses have been suggested. For several decades, the Hatrurim Complex was considered as a result of spontaneous surface combustion [11, 15, 16]. The bituminous chalks and marls of the Ghareb and Taqiye Formations, dated at Maastrichtian to Paleocene age, were subjected to

burning [11, 12]. The second hypothesis relates the origin of pyrometamorphic processes with neotectonics mud volcanism and methane burning [16–18]. The combustion metamorphism event dates to ca. 16 Ma in the Miocene and at 4.0-2.3 Ma in the Pliocene-Pleistocene [12, 19–21]. The temperature of the regional metamorphic processes is estimated at 600-900°C. However, the temperature locally reached up to 1350°C [18]. It led to the protolith's calcination, annealing, or even fusion. As a result, clinker-like mineral associations are formed [11]. The low-temperature hydrothermal stage and supergene processes are linked to the concrete formation (hydrated Portland cement and sulfoaluminate clinkers) [20, 22].

The Hatrurim Basin, a stratotype [23] (Figure 1(b)) of the Hatrurim Complex, stands out among Mottled Zone areas of diverse rock types with high and ultrahigh formation temperatures. It is composed of conical hills separated by wadis [23]. Up to now, there are the following distinguished types of high-temperature rocks: anorthite-pyroxene paralava of the olive unit, spurrite rocks and larnite pseudoconglomerates, fine-grained grey pyrrhotite-bearing amygdaloidal paralava, gehlenite-wollastonite hornfels, coarse-grained
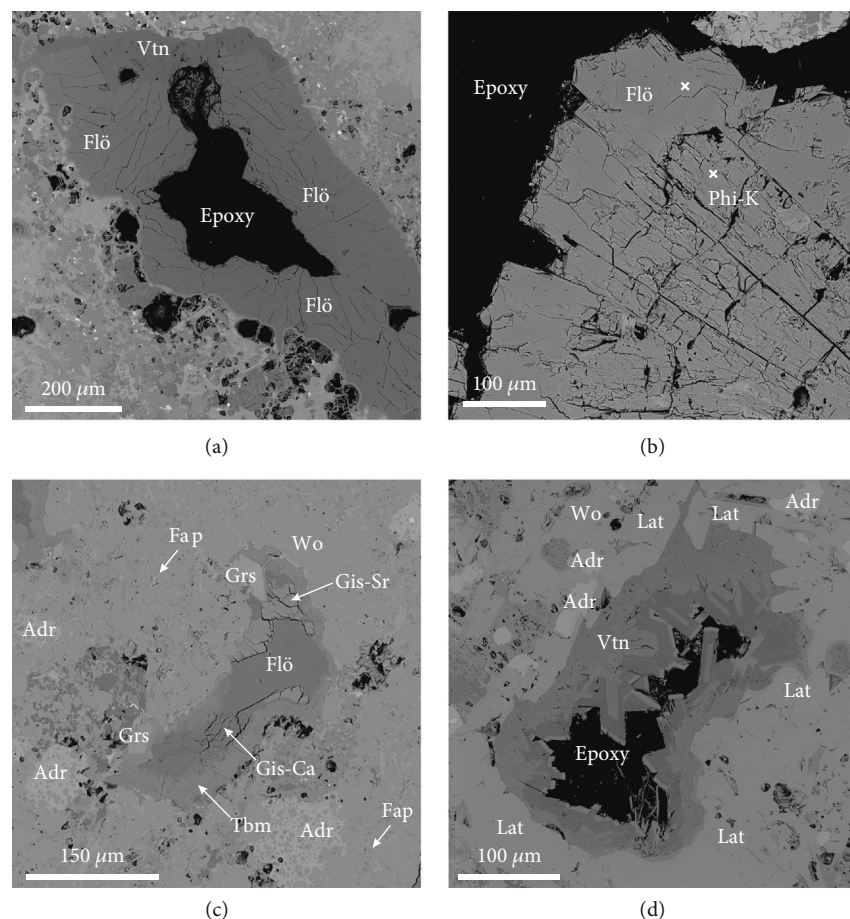
FIGURE 2: BSE images: (a) the void of gehlenite-wollastonite paralava filled with vertuminite and flörkeite; (b) crystals of phillipsite-K overgrown by flörkeite; (c) flörkeite overgrowing gismondine-Sr and gismondine-Ca in amygdule of gehlenite hornfels; x indicates a point of Raman spectra collection; (d) voids of gehlenite hornfels filled by Ba-bearing vertumnite. Adr: andradite; Fap: fluorapatite; Flö: flörkeite; Gis-Ca: gismondine-Ca; Gis-Sr: gismondine-Sr; Grs: grossular; Lat: latiumite; Phi-Ca: phillipsite-Ca; Tbm: tobermorite; Vtn: vertumnite; Wo: wollastonite.

wollastonite-andradite-schorlomite-kalsilite paralava, and recently found fine-grained esseneite-latiumite paralava and hornfels [24]. The high-temperature rocks are surrounded by brecciated metasediments and calcium-hydrosilicate rocks, so-called low-grade Hatrurim. The low-temperature mineralization, which veined pyrometamorphic rocks, is formed due to hydrothermal alteration and weathering processes, especially the interaction of meteoric water and rocks [14, 20, 23, 25]. Additionally, anorthite-pyroxene hornfels of the olive unit, located in the northern part of the Hatrurim Basin, were subjected to zeolitization [9]. Zeolites occur mainly in amygdaloidal voids of pyrometamorphic rocks associated with tobermorite supergroup minerals, minerals of ettringite group, and hydrotalcite supergroup. The veins are mainly filled by carbonates and varying amounts of ettringite and tobermorite group minerals [20, 26], which were formed in the 250–30 Ka range. Thus, they are significantly younger than high-temperature rocks [20]. This age corresponds to intensive weathering in the Southern Levant during interglacial periods [9].

Flörkeite was found in three lithological types of rocks from the 3 localities of the Hatrurim Basin (Figures 1 and 2 and supplementary Figure S1). The samples represent the high-temperature types of pyrometamorphic rocks of the Hatrurim Complex. The first sample (L1, Figure 2(a) and S1a) is composed of gehlenite, wollastonite, kalsilite, fluorapatite, garnet of the grossular-andradite-schorlomite series, chromite, pyrrhotite, and perovskite. In the amygdaloidal voids occur the following minerals: vertumnite, flörkeite, and minerals of the tobermorite supergroup. Flörkeite forms crystals up to 200 μm. According to observations, flörkeite crystallized on the vertumnite. The second sample (L2, Figure 2(b) and S1b) is less porous than L1. Esseneite, latiumite-levantite series, wollastonite, gehlenite, and garnet of the grossular-andradite-schorlomite series are the main minerals of the sample. The low-temperature mineralization is represented by flörkeite, which is grown on phillipsite-K and phillipsite-Ca (Figure 2(b)). The third sample (L3, Figure 2(c) and S1c) consists of hornfels and paralava, macroscopically nonporous. Both hornfels and paralava parts differ in grain size, but mineral associations are similar. The following minerals are associated: wollastonite, latiumite-levantite series, garnet of the grossular-andradite-schorlomite series, and gehlenite, and the accessory minerals are as follows:

52:4037074934

TABLE 1: Chemical composition of flörkeite.

Constituent	L1 Mean ($n = 12$)	s.d.	Range	L2 Mean ($n = 6$)	s.d.	Range	L3 Mean ($n = 4$)	s.d.
SiO_2	37.39	0.52	36.57-38.46	37.10	0.39	36.42-37.63	36.07	0.50
Al_2O_3	31.56	0.39	31.18-32.62	31.16	0.54	30.23-31.71	30.09	0.48
CaO	8.53	0.13	8.22-8.7	8.6	0.22	8.31-8.85	8.24	0.66
SrO	n.d.			n.d.			0.39	0.3
BaO	n.d.			n.d.			1.46	0.31
Na_2O	2.28	0.08	2.15-2.43	2.17	0.07	2.08-2.29	2.41	0.38
K_2O	10.48	0.2	10.14-10.78	10.53	0.22	10.22-10.68	10.21	0.61
H_2O	9.76			10.41			11.14	
Total	100.00			100.00			100.00	
R	0.50			0.50			0.50	
E %	3.15			1.79			-3.99	
Si	8.02			8.04			8.07	
Al	7.98			7.96			7.93	
T	16.00			16.00			16.00	
Ca	1.96			2.00			1.97	
Sr							0.05	
Ba							0.13	
Na	0.95			0.91			1.04	
K	2.87			2.91			2.91	
Extraframework	5.78			5.82			6.1	
H_2O	6.98			7.52			8.31	

s.d.: standard deviation; $R = Si/Al + Fe + Si$; E-balance error $= (Al + Fe^{3+} - Al_{theor.})/Al_{theor.} \times 100 Al_{theor.} = K + Na + 2Ca + 2Sr + 2Ba$ [32]; water content is calculated by difference to 100%; n.d.: not detected.

FIGURE 3: Raman spectra of (a) flörkeite and (b) phillipsite-K.

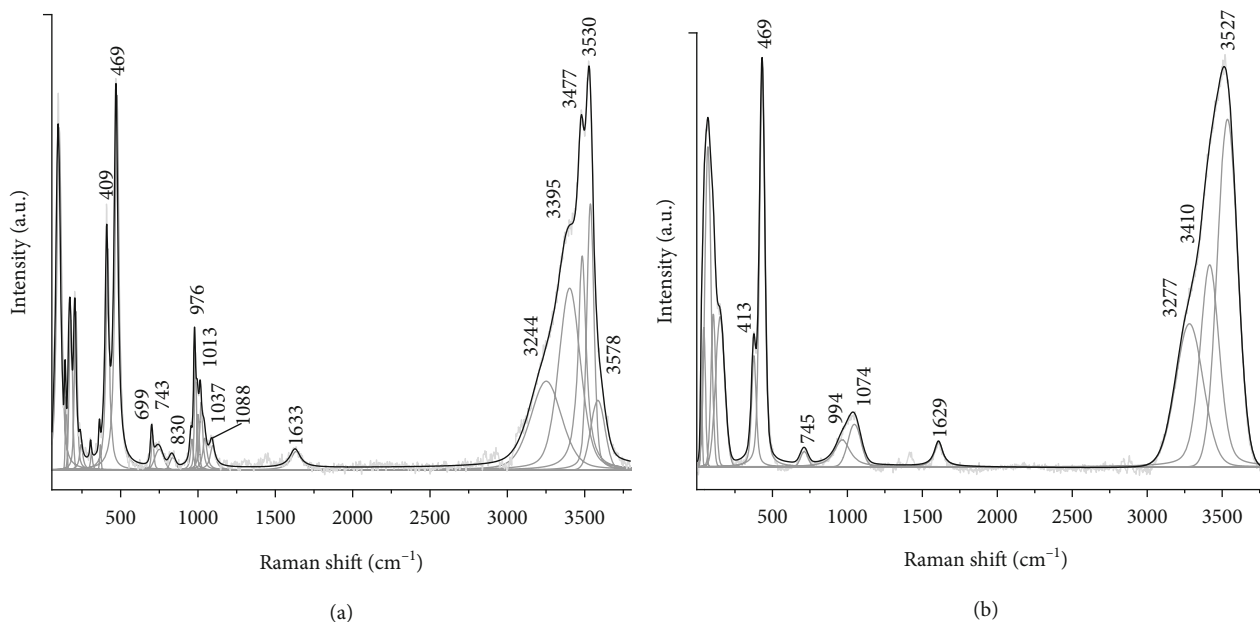fluorapatite and perovskite (Figure S1c). In voids, zeolites such as gismondine-Ca, gismondine-Sr, thomsonite-Ca, and flörkeite occur, which usually is overgrown with gismondine-Sr (Figure 2(c)) [28]. There is also analcime, which surrounds the voids, and minerals of the tobermorite supergroup. Baryte crystals were rarely observed. Additionally, vertumnite is

present in the low-temperature association (Figure 2(d)). Its crystals are characterized by zoning due to the increased barium content in the cores and rims. In gehlenite hornfels, flörkeite occurs as xenomorphic crystals filling the voids and rarely as automorphic crystals. In contrast to L1 and L2, zeolite mineralization of gehlenite hornfels is definitely more diverse. In all cases, minerals of the ettringite group are rarely associated with zeolites. Also, it should be emphasized that zeolites fill voids rather than veins.

3. Analytical Methods

3.1. Chemical Composition. The preliminary chemical composition of zeolites and minerals of the host rocks was examined by scanning electron microscope (Phenom XL), equipped with an EDS (energy-dispersive X-ray spectrometer) detector. Their morphology and composition inhomogeneity were observed in backscattered electron mode. The quantitative chemical analyses of the samples L1 and L2 were obtained by electron microprobe, using a CAMECA SX100 operating at 15 keV and 10 nA. For sample L1, the spot size was defocused to $10\,\mu m$. For sample L2, beam size of $8\,\mu m$ was used. The following lines and standards were used for both samples: $NaK\alpha$ = albite, $SiK\alpha$ = diopside, $AlK\alpha$ = orthoclase, $KK\alpha$ = orthoclase, $CaK\alpha$ = diopside, $SrL\alpha$ = celestine, and $BaL\alpha$ = baryte. Sample L3 was also investigated with the CAMECA SX100 electron microprobe analyzer at 15 kV and 10 nA. The spot size was equal to $10\,\mu m$. The lines and standards were as follows: $NaK\alpha$ = NaCl, $SiK\alpha$ = wollastonite, $AlK\alpha$ = orthoclase, $KK\alpha$ = orthoclase, $CaK\alpha$ = wollastonite, $SrL\alpha$ = celestine, and $BaL\alpha$ = baryte.

3.2. Raman Spectroscopy. For a complete characterization of mineral flörkeite, Raman spectroscopy was performed. Raman spectra were collected using a confocal Raman microscope WITec alpha 300R equipped with a 488 nm laser, and a CCD camera was used to obtain the spectrum. A $30\,\mu m$ optical fiber and a monochromator with a $600\,mm^{-1}$ grating were used to record the Raman spectra. The monochromator calibration was conducted using a Raman scattering line of a silicon plate ($520.7\,cm^{-1}$). Measurement time amounted to 3 s with an accumulation of 25 scans. The spectral resolution was $3\,cm^{-1}$. In order to refine the Raman spectrum, the spectral software package GRAMS was used.

3.3. SC-XRD. Single-crystal X-ray diffraction (SC-XRD) data were collected using a Rigaku Synergy-S diffractometer equipped with a dual microfocused source and a Hypix detector. The $CuK\alpha$ radiation ($\lambda = 1.540598$ Å) was chosen due to the small size of the crystal. Data reduction and absorption correction were conducted using the software package CrysalisPro 40.29a. The structure was solved by direct methods using SHELXS [29]. During the refinement of the structure, which was carried out using SHELXL [30], neutral atomic scattering factors were used for all atoms.

TABLE 2: Parameters for X-ray data collection and crystal structure refinement of flörkeite.

Crystal data	
Empirical formula	$K_{3.02}Ca_{1.98}Na_{0.99}Al_{8.01}Si_{8.01}O_{44.01}$
Crystal system	Triclinic
Space group	-1
	$a = 19.9366\,(2)$
	$b = 14.25170\,(1)$
	$c = 8.69350\,(1)$
Unit cell dimensions (Å, °)	$\alpha = 88.2480\,(1)$
	$\beta = 125.0960\,(1)$
	$\gamma = 89.6350\,(1)$
Volume (Å^3)	2019.19 (4)
Formula weight	303.34
Data collection	
Diffractometer	Synergy-S
Radiation wavelength (Å)	1.54184
Temperature (K)	293 (2)
Absorption coefficient (mm^{-1})	10.582
F(000)	1352
θ range for data collection (°)	3.104–80.112
	$-25 \leq h \leq 25$
Index ranges	$-17 \leq k \leq 12$
	$-11 \leq l \leq 11$
Structure refinement	
Reflections collected	27274
Independent reflections	8593
Observed data ($I > 2\sigma(I)$)	7486
$R_1, wR_2\ (I > 2\sigma(I))$	0.0341 (wR = 0.0995)
R_1, wR_2 (for all)	0.0390 (wR = 0.1027)
GooF	1.087
$\Delta\rho_{min}$ (e/Å^{-3})	-0.764
$\Delta\rho_{max}$ (e/Å^{-3})	0.102

4. Results

4.1. Chemical Composition. The results of flörkeite chemical microanalysis are given in Table 1. The empirical crystal-chemical formulas of flörkeite were calculated based on 16 framework T-*sites*. The flörkeite empirical crystal-chemical formulas were determined as follows for the corresponding localities: L1, $(K_{2.87}Ca_{1.96}Na_{0.95})[Al_{7.93}Si_{8.07}O_{31.91}]\cdot12H_2O$; L2, $(K_{2.91}Ca_{2.00}Na_{0.91})[Al_{7.96}Si_{8.04}O_{31.94}]\cdot12H_2O$; and L3, $(K_{2.91}Ca_{1.97}Na_{1.04}Ba_{0.13}Sr_{0.05})[Al_{7.93}Si_{8.07}O_{32.16}]\cdot12H_2O$. The water contents calculated for flörkeite on the base of microprobe analyses are underestimated (Table 1). A similar problem was noticed for the microprobe analyses of flörkeite from the type locality [8]. The theoretical determination of water content in flörkeite based on the mean refractive index and ion polarizability gives the water content about $12H_2O$ [31]. In the empirical formulas of the studied flörkeite, we used the water content obtained by structural data. The

TABLE 3: Atom coordinates (x, y, and z), equivalent isotropic displacement parameters (U_{iso}, Å^2), and site occupancies of flörkeite.

Site	Atom	x	y	z	U_{eq}/U_{iso} (Å^2)	Occupancy
K1	K	0.42274 (4)	-0.74243 (5)	0.64599 (10)	0.03247 (15)	1
K2	K	-0.06261 (5)	-0.74923 (5)	0.73279 (13)	0.04070 (18)	1
K3	K	0.41577 (4)	-0.74191 (5)	0.11511 (11)	0.03779 (17)	1
Ca1	Ca	0.19490 (3)	-0.87734 (3)	0.05342 (7)	0.01449 (11)	1
Ca2	Ca	0.21055 (3)	-0.34979 (3)	0.04392 (7)	0.01602 (11)	1
Na1	Na	0.29854 (7)	-0.13244 (8)	0.93652 (16)	0.0263 (2)	1
Si1	Si	0.07219 (4)	-0.64049 (4)	0.57303 (8)	0.00787 (12)	1
Si2	Si	0.29350 (3)	-0.14230 (4)	0.53221 (8)	0.00739 (12)	1
Si3	Si	0.46547 (3)	-0.99945 (4)	0.21715 (8)	0.00769 (12)	1
Al1	Al	0.29108 (4)	-0.35957 (4)	0.49658 (9)	0.00808 (13)	1
Si4	Si	0.20831 (3)	-0.85633 (4)	0.48076 (8)	0.00709 (12)	1
Si5	Si	0.03798 (3)	-0.00179 (4)	0.79311 (8)	0.00726 (12)	1
Si6	Si	0.37213 (3)	-0.53873 (4)	0.79003 (8)	0.00795 (12)	1
Al2	Al	0.06494 (4)	-0.86337 (4)	0.54300 (9)	0.00771 (13)	1
Si7	Si	0.43037 (4)	-0.35693 (4)	0.43460 (8)	0.00930 (12)	1
Al3	Al	0.56986 (4)	-0.86651 (4)	0.55618 (9)	0.00805 (13)	1
Al4	Al	0.21212 (4)	-0.63933 (4)	0.51376 (9)	0.00812 (13)	1
Al5	Al	0.12924 (4)	-0.02609 (4)	0.23219 (9)	0.00729 (13)	1
Al6	Al	0.37530 (4)	-0.97002 (4)	0.77592 (9)	0.00756 (13)	1
Si8	Si	0.12877 (3)	-0.46335 (4)	0.21277 (8)	0.00783 (12)	1
Al7	Al	0.02871 (4)	-0.50803 (4)	0.78793 (9)	0.00764 (13)	1
Al8	Al	0.47077 (4)	-0.49336 (4)	0.21018 (9)	0.00857 (13)	1
O1	O	0.04250 (11)	-0.74724 (11)	0.5472 (3)	0.0168 (3)	1
O2	O	0.00647 (11)	-0.58452 (12)	0.3768 (2)	0.0167 (3)	1
O3	O	0.07405 (11)	-0.59975 (12)	0.7466 (2)	0.0159 (3)	1
O4	O	0.16495 (10)	-0.63534 (13)	0.6311 (3)	0.0171 (3)	1
O5	O	0.30313 (10)	-0.25155 (11)	0.5975 (2)	0.0133 (3)	1
O6	O	0.33896 (10)	-0.12260 (12)	0.4282 (2)	0.0143 (3)	1
O7	O	0.19641 (10)	-0.11540 (11)	0.3854 (2)	0.0126 (3)	1
O8	O	0.33293 (11)	-0.08114 (11)	0.7184 (2)	0.0139 (3)	1
O9	O	0.54823 (10)	-0.04596 (12)	0.2584 (3)	0.0157 (3)	1
O10	O	0.40609 (10)	-0.95326 (11)	0.0053 (2)	0.0133 (3)	1
O11	O	0.48473 (10)	-0.91408 (11)	0.3555 (2)	0.0124 (3)	1
O12	O	0.41394 (10)	-0.07871 (11)	0.2419 (2)	0.0122 (3)	1
O13	O	0.32858 (11)	-0.44110 (12)	0.6782 (3)	0.0180 (4)	1
O14	O	0.18954 (10)	-0.37502 (11)	0.3059 (2)	0.0111 (3)	1
O15	O	0.33573 (10)	-0.35997 (12)	0.3701 (2)	0.0149 (3)	1
O16	O	0.19584 (11)	-0.74782 (11)	0.4119 (2)	0.0143 (3)	1
O17	O	0.17532 (10)	-0.91668 (11)	0.2935 (2)	0.0126 (3)	1
O18	O	0.15676 (10)	-0.88348 (12)	0.5666 (2)	0.0147 (3)	1
O19	O	0.30417 (10)	-0.88078 (12)	0.6353 (2)	0.0159 (3)	1
O20	O	-0.04171 (10)	-0.96088 (12)	0.7740 (2)	0.0138 (3)	1
O21	O	0.07841 (10)	-0.91770 (11)	0.7436 (2)	0.0114 (3)	1
O22	O	0.01839 (10)	-1.09034 (11)	0.6629 (2)	0.0139 (3)	1
O23	O	0.11108 (10)	-1.03313 (11)	0.0097 (2)	0.0119 (3)	1
O24	O	0.31592 (10)	-0.62772 (11)	0.6847 (2)	0.0129 (3)	1
O25	O	0.10799 (10)	-0.46199 (11)	1.0016 (2)	0.0118 (3)	1
O26	O	0.38865 (10)	-0.53587 (11)	0.9965 (2)	0.0126 (3)	1

TABLE 3: Continued.

Site	Atom	x	y	z	U_{eq}/U_{iso} (Å²)	Occupancy
O28	O	0.04743 (10)	-0.44150 (12)	0.2033 (2)	0.0152 (3)	1
O29	O	0.45816 (10)	-0.55832 (12)	0.8164 (2)	0.0155 (3)	1
O30	O	0.43204 (11)	-0.40132 (12)	0.2672 (2)	0.0161 (3)	1
O31	O	0.17464 (11)	-0.56030 (12)	0.3243 (2)	0.0170 (3)	1
O32	O	0.45985 (11)	-0.24987 (11)	0.4576 (3)	0.0155 (3)	1
O33	O	0.49284 (12)	-0.41221 (12)	0.6330 (3)	0.0201 (4)	1
W1	O	0.52962 (16)	-0.7311 (2)	1.0427 (4)	0.0474 (6)	1
W2	O	0.30993 (12)	-0.30203 (14)	0.9617 (3)	0.0232 (4)	1
W3	O	0.3133 (3)	-0.6309 (2)	0.2899 (6)	0.0838 (13)	1
W4	O	0.25178 (11)	-0.96378 (14)	0.9220 (3)	0.0218 (4)	1
W5	O	0.11174 (13)	-0.74485 (14)	1.0213 (3)	0.0262 (4)	1
W6	O	0.22652 (12)	-1.18038 (13)	1.0777 (3)	0.0215 (4)	1
W7	O	0.25039 (13)	-0.74439 (15)	0.9765 (3)	0.0317 (5)	1
W8	O	0.33720 (12)	-0.88100 (15)	0.3257 (3)	0.0242 (4)	1
W9	O	0.24838 (13)	-0.49830 (15)	0.9762 (4)	0.0343 (5)	1
W10	O	0.13807 (16)	-0.3297 (2)	0.7090 (4)	0.0555 (8)	1
W11	O	0.06612 (18)	-0.26114 (18)	0.9165 (4)	0.0523 (7)	1
W12	O	0.15461 (16)	-0.14255 (19)	0.6492 (4)	0.0399 (5)	1

presence of barium and strontium distinguishes the third sample from the others. The presented data are consistent with the end member formula $(K_3Ca_2Na)[Al_8Si_8O_{32}]\cdot12H_2O$ and data reported for the type specimen [8].

4.2. Raman Spectroscopy. Raman spectra of flörkeite and phillipsite-K are presented in Figure 3. Vibrational spectra consist of three range: $150-469\,cm^{-1}$, $699-830\,cm^{-1}$, and $976-1088\,cm^{-1}$ [33–35]. The main characteristic band is approximately $470\,cm^{-1}$. It corresponds to the motion of an oxygen atom in a plane perpendicular to the T–O–T bond, which means symmetric bending T–O–T vibrations [33, 34], whereas bands below $470\,cm^{-1}$ are assigned to pore opening vibrations [33, 36]. Bands within $699 - 830\,cm^{-1}$ are attributed to symmetric stretching T–O–T vibrations. Vibrations of asymmetric stretching T–O–T motions are present between 976 and $1088\,cm^{-1}$. In the ranges $699-830\,cm^{-1}$ and $976-1088\,cm^{-1}$, the intratetrahedral asymmetric and symmetric stretching T–O vibrations occur, respectively [33, 35, 37]. The bands between 3244 and $3578\,cm^{-1}$ correspond to the stretching vibrations of water molecules; the bending vibrations of which are present between 1629 and $1633\,cm^{-1}$ [38].

4.3. Crystallography and Structure Description. The crystal structure of flörkeite was refined from SC-XRD data. Table 2 reports the details of the experimental and refinement procedure. According to the data from Tables 3 and 4, Si and Al are orderly arranged at the 16 framework sites in compliance with the Löewenstein rule and previous studies [8, 39]. The mean cation-oxygen distance of aluminum tetrahedra is 1.74 Å, and the mean length of silica tetrahedra is equal to 1.62 Å (Table 4). The interatomic distances between extrafra-

mework cations and oxygen atoms within the flörkeite structure are reported in Table 5.

Flörkeite has a **PHI** framework type with an ordered distribution of Si/Al at *T*-sites and ordered arrangement of extraframework cations. The **PHI**-type structures are constituted by double-connected 4-member rings, which form double crankshaft chains (*dcc*) (Figure 4(a)) [40–42]. In the **PHI** framework type, the *dcc* resembles a corrugated ribbon and runs parallel to the *a*-axis forming 8-membered windows on the layer perpendicular to [100] [42–44]. In the **PHI**-type structure, there are two channel systems and two types of cages [6, 8, 43, 44].

The channel system parallel to [100] consists of alternately a *phi* and an *oto* units (Figure 5(a)). The channel, confined by an 8-membered window of the *phi* units, is parallel to [010] (Figure 5(b)). Thus, the *phi* unit appears at the intersection of the two channels system (Figures 4 and 5).

The dimensions of the units vary depending on the extraframework cation content (Figure 6). In flörkeite, the *oto* units are occupied by potassium and water molecules. Two types of the *oto* units can be distinguished based on the distribution of water molecules (Figures 6(a)–6(d)). In the *oto I*, the water molecule (W11) is located in the center of the 8-member ring (Figures 6(a) and 6(b)), whereas in the *oto II*, the water molecule (W1) is within the cage (Figures 6(c) and 6(d)). In phillipsite-type minerals, the *oto* units are occupied by large cations such as K and Ba [43]. Greater diversity has been observed between the two types of *phi* units (Figures 6(e)–6(h)). The *phi I* is occupied by K, Ca, and water molecules (Figures 6(e) and 6(f)). Potassium is located near the center of the 8-membered ring (Figure 6(f)), wherein phillipsite-K water molecules are present [8]. The calcium is located within the unit (Figures 6(e) and 6(f)). Water molecules (W5, W4, and W9) are located

Table 4: Selected interatomic distances of the framework of flörkeite structure.

Site 1	Site 2	Distance (Å)	Site 1	Site 2	Distance (Å)
Si1	O1	1.6109 (17)	Al1	O5	1.7091 (18)
Si1	O2	1.6114 (17)	Al1	O13	1.7091 (18)
Si1	O3	1.6144 (17)	Al1	O14	1.7504 (17)
Si1	O4	1.6156 (18)	Al1	O15	1.7684 (18)
Mean		1.613	Mean		1.734
Si2	O5	1.6124 (16)	Al2	O1	1.7187 (17)
Si2	O6	1.6275 (17)	Al2	O18	1.7417 (18)
Si2	O7	1.6256 (17)	Al2	O21	1.7577 (17)
Si2	O8	1.6217 (17)	Al2	O22	1.7511 (17)
Mean		1.622	Mean		1.742
Si3	O9	1.6065 (17)	Al3	O6	1.7486 (18)
Si3	O10	1.6232 (17)	Al3	O11	1.7511 (17)
Si3	O11	1.6243 (17)	Al3	O12	1.7479 (17)
Si3	O12	1.6224 (17)	Al3	O32	1.7349 (17)
Mean		1.619	Mean		1.746
Si4	O16	1.6059 (17)	Al4	O4	1.7421 (18)
Si4	O17	1.6385 (17)	Al4	O16	1.7432 (17)
Si4	O18	1.6224 (17)	Al4	O24	1.7324 (17)
Si4	O19	1.6091 (17)	Al4	O31	1.7322 (18)
Mean		1.619	Mean		1.737
Si5	O20	1.6030 (17)	Al5	O7	1.7352 (17)
Si5	O21	1.6281 (16)	Al5	O17	1.7508 (17)
Si5	O22	1.6159 (17)	Al5	O20	1.7263 (17)
Si5	O23	1.6292 (16)	Al5	O23	1.7573 (17)
Mean		1.619	Mean		1.742
Si6	O13	1.6020 (17)	Al6	O8	1.7469 (17)
Si6	O24	1.6162 (17)	Al6	O9	1.7288 (18)
Si6	O26	1.6297 (17)	Al6	O10	1.7421 (17)
Si6	O29	1.6157 (17)	Al6	O19	1.7354 (17)
Mean		1.616	Mean		1.738
Si7	O15	1.6317 (17)	Al7	O2	1.7321 (17)
Si7	O30	1.6222 (18)	Al7	O3	1.7440 (17)
Si7	O32	1.6150 (17)	Al7	O25	1.7581 (17)
Si7	O33	1.6063 (18)	Al7	O28	1.7237 (18)
Mean		1.619	Mean		1.739
Si8	O14	1.6316 (16)	Al8	O26	1.7559 (18)
Si8	O25	1.6325 (17)	Al8	O29	1.7269 (18)
Si8	O28	1.6037 (17)	Al8	O30	1.7404 (17)
Si8	O31	1.6025 (17)	Al8	O33	1.7131 (18)
Mean		1.618	Mean		1.734
Total mean		1.618	Total mean		1.739

Table 5: Selected interatomic distances of the extraframework cations in flörkeite structure.

Site 1	Site 2	Distance (Å)	Site 1	Site 2	Distance (Å)
K1	W1	2.837 (3)	Ca2	O14	2.5574 (17)
K1	O24	2.8521 (18)	Ca2	O15	2.4744 (18)
K1	O29	2.9387 (18)	Ca2	O25	2.4668 (17)
K1	O32	2.9547 (19)	Ca2	W2	2.553 (2)
K1	W3	2.959 (4)	Ca2	W6	2.4418 (19)
K1	O19	3.0499 (18)	Ca2	W9	2.442 (2)
K1	O9	3.0647 (18)	Ca2	W10	2.399 (3)
K1	W8	3.079 (2)	Ca2	W11	2.705 (3)
K2	O28	2.7746 (18)	Na	O8	2.453 (2)
K2	W5	2.892 (2)	Na	O12	2.460 (2)
K2	O14	2.9292 (17)	Na	W12	2.506 (3)
K2	O7	2.9881 (18)	W1	K3	2.686 (3)
K2	O20	3.0243 (18)	W2	Ca2	2.553 (2)
K2	W11	3.098	W4	Ca1	2.3804 (19)
K2	W12	3.180 (3)	W5	Ca1	2.406 (2)
K2	O1	3.298 (2)	W6	Ca2	2.4418 (19)
K2	W10	3.369 (3)	W7	K3	2.786 (2)
K3	W1	2.686 (3)	W9	Ca2	2.443 (2)
K3	W7	2.786 (2)	W10	K2	3.369 (3)
K3	O11	2.9355 (18)	W11	K2	3.098 (4)
K3	O33	2.949 (2)	W12	K2	3.180 (3)
K3	O26	3.0218 (18)	W4	Na	2.546 (2)
K3	O32	3.056 (2)	W6	Na	2.5454 (2)
K3	O10	3.1610 (18)	W7	Ca1	2.462 (2)
K3	O24	3.4106 (18)	W9	Ca2	2.442 (2)
Ca1	O17	2.3854 (17)	W10	Ca2	2.399
Ca1	O21	2.4283 (17)	W11	Ca2	2.705 (3)
Ca1	O23	2.6899 (17)			
Ca1	W4	2.3803 (19)			
Ca1	W5	2.406 (2)			
Ca1	W7	2.462 (2)			
Ca1	W8	2.434 (2)			

near the center of the 8-membered rings, which build the unit. W8 and W3 water molecules are found in a cavity formed by a double crankshaft chain (Figures 6(e) and 6(f)). The *phi II* unit is closer to the phillipsite-K structure

[6, 8, 43]. Na and Ca cations and water molecules are inside the *phi II* unit [6, 43, 44]. However, in phillipsite-K, the Na position is equivalent to the Ca site, and the Ca site is a counterpart of the water position [8]. The symmetry of the **PHI** structure aristotype (topological symmetry) is $Cmcm$, which is reduced to $P2_1/m$ [8, 40, 41, 45] as a result of a slight distortion induced on the tetrahedral framework by the presence of larger cations (K and Ba) [7]. Full occupancy of large cations position in flörkeite structure increased the distortion of the framework. The topochemical symmetry of flörkeite is lowered to $B2/b$ due to ordered Si/Al distribution in the tetrahedral framework, which is the main difference between flörkeite and phillipsite minerals [8, 40]. As noted by Lengauer et al. [8], the atomic coordinates of the framework do not exhibit significant differences in the two minerals (Table 3). A comparison of the unit cell parameters of phillipsite and flörkeite
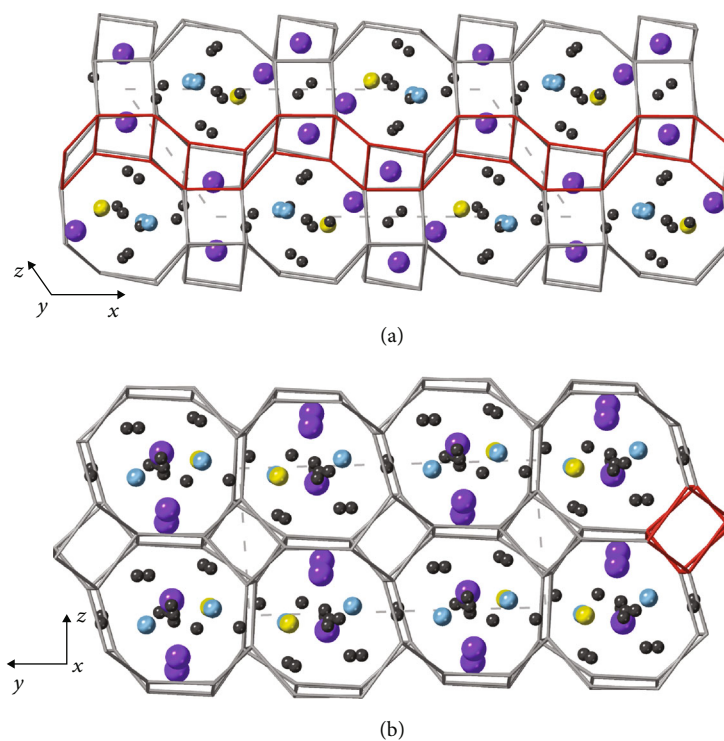
FIGURE 4: Extraframework cations in flörkeite framework: (a) projection along [010]; (b) projection of framework with extraframework cations along [100], a double crankshaft chain is marked red. Potassium, calcium, and sodium are purple, blue, and yellow spheres, respectively. Dark grey spheres represent H_2O sites.
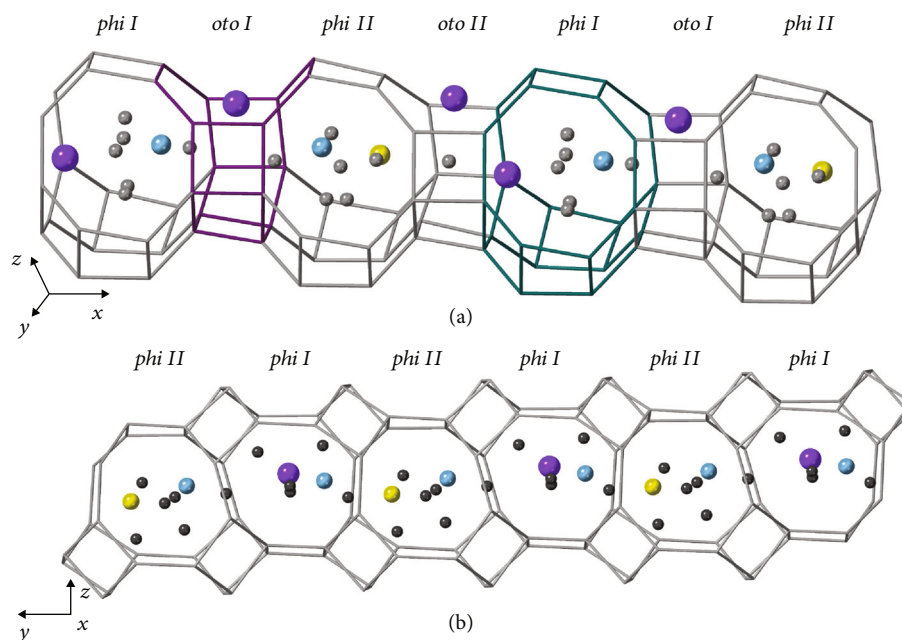
FIGURE 5: (a) Channel running along [100] within flörkeite structure: the *phi* unit is marked by green color, and the *oto* unit is marked by purple color; (b) channel composed of *phi* units running along [010] in flörkeite structure. Potassium, calcium, and sodium are purple, blue, and yellow spheres, respectively. Dark grey spheres represent H_2O sites.

revealed the doubling of *a* parameter in flörkeite, which is a consequence of the ordered arrangement of extraframework cations (Figure 5(a), [8]). The ordered distribution of extra-framework cations within flörkeite channels causes a reduction of the topochemical symmetry to the triclinic real symmetry [8].

FIGURE 6: (a, b) The *oto I* unit in two orientations occupied by potassium (K1), the water molecule at W11 is near the center of the 8-membered ring; (c, d) the *oto II* unit is filled by potassium (K2) and a water molecule at W1; (e, f) the *phi I* in two orientations occupied by calcium (Ca1) and potassium (K3), which is located near the center of 8-membered ring, and water molecules: W3, W4, W5, W7, W8, and W9; (g, h) the *phi II* in two orientations, which is occupied by calcium (Ca2), sodium (Na), and water molecules W6, W10, and W12.

5. Discussion

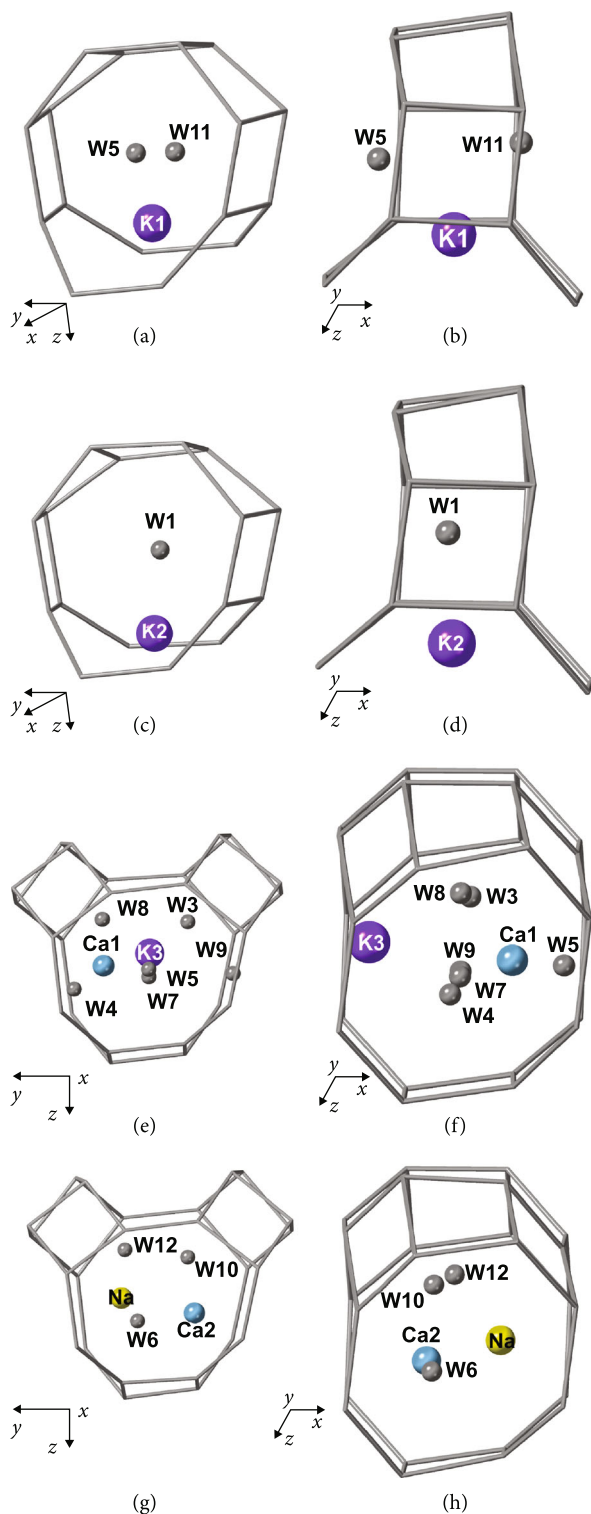The Hatrurim Complex is the second occurrence of flörkeite, which is the most abundant zeolite in the voids of high-temperature pyrometamorphic rocks. The obtained results on flörkeite from the Hatrurim Complex are similar to those on the type flörkeite from the Bellerberg volcano. The structure of the studied flörkeite does not differ significantly from the crystal structure of the type specimen (($K_{2.96}$, $Ca_{2.04}$, $Na_{1.02}$, $Mg_{0.01}$)[$Al_{8.03}Si_{7.97}O_{31.97}$]$\cdot 11.72H_2O$; $a = 19.965\,(1)$ Å, $b = 14.274\,(1)$ Å, $c = 8.704\,(1)$ Å, $\alpha = 88.37\,(1)°$, $\beta = 125.08\,(1)°$, $\gamma = 89.57\,(1)°$, and $V = 2028.2\,(3)$ Å^3; [8]). Also, the empirical formulas of flörkeite from the three localities of the Hatrurim Basin are close to the ideal formula (Table 1, [8]). The flörkeite and phillipsite-K Raman spectra show strong similarities (Figure 3), indicating that the main band at ~470 cm^{-1}, characteristics of the **PHI**-type structures, does not depend on the framework ordering and Si/Al ratio. The symmetric and asymmetric stretching T–O–T vibration in the region 700-1100 cm^{-1} of flörkeite spectrum confirms its ordered framework. The wide complex band of water molecule vibrations in the phillipsite-K spectrum indicates a disordered arrangement of partially occupied sites by water. Overall, the general features of the spectra are unchanged, and the Si/Al ordering at the tetrahedral sites induces minor differences. The chemical composition of L1 and L2 samples does not show significant differences. In the L1 sample of amygdaloidal paralava, flörkeite occurs in voids and associates with vertumnite ($Ca_4Al_4Si_4O_6(OH)_{24}\cdot 3H_2O$), in which no barium impurity was revealed. The chemical composition of zeolites from the latiumite-esseneite rock is relatively homogenous. Comparing phillipsite series $K_2(Ca_{0.5},Na)_4(Al_6Si_{10})O_{32}\cdot 12H_2O$ and flörkeite (K_3Ca_2Na)[$Al_8Si_8O_{32}$]$\cdot 12H_2O$ formulas reveals the depletion of extraframework cations in phillipsite minerals, balanced by the higher Si/Al ratio. Overgrowing flörkeite on phillipsite-K indicates a decrease of the Si/Al and Ca/(K + Na) ratio (Figure 2). A little amount of strontium and barium impurities distinguish the flörkeite composition of sample L3 (Table 1). In the **PHI**-type structures, barium substitutes potassium in the *oto* units [43]. In contrast, according to ion-exchanged phillipsite data, strontium could be present in *oto* and *phi* units [44]. Among the analyzed pyrometamorphic rock samples, gehlenite hornfels is distinguished by the greatest variety of zeolite mineralization. Likewise to the Bellerberg volcano, apart from flörkeite, other high-aluminum zeolites, such as gismondine-Sr, gismondine-Ca, and thomsonite-Ca, have been reported [28]. The presented data on flörkeite in voids of gehlenite hornfels and the presence of gismondine-Sr and Ba-bearing vertumnite (Table 1) point out the high content of barium and strontium in the low-temperature mineralization of these rocks. The sharp boundary between Ba-rich and Ba-poor vertumnite indicates an intense increase in the barium content in the crystallization medium (Figure 2). Moreover, gehlenite hornfels enrichment in barium and strontium is in agreement with the previous studies [22, 23, 46]. These elements have been dispersed in the baryte-hashemite and fluorapatite-fluorellestadite series [23,

47]. Zeolite mineralization of pyrometamorphic rocks varies compared to zeolite-bearing olive unit rocks. In zeolite-bearing rocks of the olive unit, zeolites such as thomsonite-Ca and gismondine-Ca are predominant. Phillipsite-Ca and clinoptilolite-Ca are rarely observed. Compared to the present data, the zeolite mineralization of the olive unit is characterized by a higher Si/Al ratio, as evidenced by the presence of clinoptilolite $Ca_3(Si_{30}Al_6)O_{72} \cdot 20H_2O$. Si/Al ratio differences could be related to the protoliths diversity [48–50]. A low Si/Al ratio in zeolites displays a highly alkaline environment [1, 48, 50–53]. The favourable pH for zeolite crystallization is around 9-10 [1, 48, 54]. The crystallization sequence of the low-temperature mineralization in all samples corresponds to the Ca/(K+Na) ratio decrease. Thus, the formation process of zeolite mineralization could be divided into two steps: the first step was characterized by the higher calcium content, whereas monovalent cations were dominant in the second step. As a result, flörkeite is formed at the end of a low-temperature crystallization sequence (Figure 2).

6. Conclusions

Zeolite flörkeite, known only from the xenolith in the Bellerberg volcano area, Germany, is a widespread low-temperature mineral in voids of gehlenite-bearing pyrometamorphic rocks in the Hatrurim Complex, Israel. It is a fully ordered zeolite characterize by the highest aluminium content among phillipsite-type zeolites. For the first time, Raman spectrum of flörkeite has been collected. The Raman spectroscopy investigation of **PHI**-type minerals indicates that the position of the main band at $470\,cm^{-1}$ does not depend on the Si/Al ratio and ordering at tetrahedral sites. Zeolitization in pyrometamorphic rocks of the Hatrurim Basin features a low silica activity and high pH conditions resulting from the reaction between meteoric waters and clinker-like rocks [55]. The zeolite mineralization of amygdule results from meteoric water circulations in pyrometamorphic rocks during their cooling [4, 9, 56, 57]. Extremely high aluminum contents are caused by the alteration of rock-forming minerals such as gehlenite, mayenite group minerals, ye'elimite, levantite-latiumite series, and kalsilite. The occurrence of flörkeite in different pyrometamorphic rocks indicates the relatively uniform, regional forming conditions, and open hydrologic system of zeolitization.

Data Availability

All data generated or analyzed during this study are included in this published article and its supplementary materials. Primary data are available from the corresponding author on request.

Conflicts of Interest

The authors declare that they have no conflicts of interest.

Supplementary Materials

Figure 1S: general view of rock-forming minerals in (a) the L1 sample amygdaloidal paralava and (b) the L2 sample esseneite-latiumite paralava; (c) the L3 sample, boundary between fine-grained hornfels and coarse-grained paralava is visible. Adr: andradite; Chr: chromite; Cls: celsian; Ess: esseneite; Fap: fluorapatite; Gh: gehlenite; Grs: grossular; Kls: kalsilite; Lat: latiumite; Wo: wollastonite. *(Supplementary Materials)*

References

[1] R. L. Hay and R. A. Sheppard, "Occurrence of zeolites in sedimentary rocks: an overview," *Reviews in Mineralogy and Geochemistry*, vol. 45, pp. 217–232, 2001.

[2] M. Utada, "Zeolites in hydrothermally altered rocks," *Reviews in Mineralogy and Geochemistry*, vol. 45, no. 1, pp. 305–322, 2001.

[3] F. Bernhard and U. Barth-Wirsching, "Zeolitization of a phonolitic ash flow by groundwater in the Laach volcanic area, Eifel, Germany," *Clays and Clay Minerals*, vol. 50, no. 6, pp. 710–725, 2002.

[4] T. B. Weisenberger, S. Spürgin, and Y. Lahaye, "Hydrothermal alteration and zeolitization of the Fohberg phonolite, Kaiserstuhl volcanic complex, Germany," *International Journal of Earth Sciences*, vol. 103, no. 8, pp. 2273–2300, 2014.

[5] R. A. Sheppard and R. L. Hay, "Formation of zeolites in open hydrologic systems," *Reviews in Mineralogy and Geochemistry*, vol. 45, pp. 261–273, 2001.

[6] G. D. Gatta, P. Cappelletti, N. Rotiroti, C. Slebodnick, and R. Rinaldi, "New insights into the crystal structure and crystal chemistry of the zeolite phillipsite," *American Mineralogist*, vol. 94, no. 1, pp. 190–199, 2009.

[7] E. Passaglia and A. Sheppard, "The Crystal Chemistry of Zeolites," *Reviews in Mineralogy and Geochemistry*, vol. 45, pp. 69–116, 2001.

[8] C. L. Lengauer, U. Kolitsch, and E. Tillmanns, "Florkeite, $K_3Ca_2Na[Al_8 Si_8 O_{32}]12H_2 O$, a new phillipsite-type zeolite from the Bellerberg, East Eifel volcanic area, Germany," *European Journal of Mineralogy*, vol. 21, no. 4, pp. 901–913, 2009.

[9] Ł. Kruszewski, V. Palchik, Y. Vapnik, K. Nowak, K. Banasik, and I. Galuskina, "Mineralogical, geochemical, and rock mechanic characteristics of zeolite-bearing rocks of the Hatrurim basin, Israel," *Minerals*, vol. 11, no. 10, p. 1062, 2021.

[10] Y. K. Bentor, "Israel," *Lexique Stratigraphique International, Asie*, vol. III, p. 80, 1960.

[11] S. Gross, "The mineralogy of the Hatrurim formation, Israel," *Geological Survey of Israel Bulletin*, vol. 70, 1977.

[12] A. Burg, A. Starinsky, Y. Bartov, and Y. Kolodny, "Geology of the Hatrurim formation ("Mottled Zone") in the Hatrurim

60:8849643107

basin," *Israel Journal of Earth Sciences*, vol. 40, pp. 107–124, 1991.

[13] A. Burg, Y. Kolodny, and V. Lyakhovsky, "Hatrurim-2000: the "Mottled Zone" revisited, forty years later," *Israel Journal of Earth Sciences*, vol. 48, pp. 209–223, 1999.

[14] Y. V. Seryotkin, E. V. Sokol, S. N. Kokh, and V. V. Sharygin, "Natural bentorite—Cr^{3+} derivate of ettringite: determination of crystal structure," *Phys Chem Minerals*, vol. 46, no. 6, pp. 553–570, 2019.

[15] I. Novikov, Y. Vapnik, and I. Safonova, "Mud volcano origin of the Mottled Zone, south Levant," *Geoscience Frontiers*, vol. 4, no. 5, pp. 597–619, 2013.

[16] I. O. Galuskina, Y. Vapnik, B. Lazic, T. Armbruster, M. Murashko, and E. V. Galuskin, "Harmunite CaFe2O4: a new mineral from the Jabel Harmun, West Bank, Palestinian Autonomy, Israel," *American Mineralogist*, vol. 99, no. 5-6, pp. 965–975, 2014.

[17] E. V. Sokol, I. S. Novikov, S. N. Zateeva, V. V. Sharygin, and Y. E. Vapnik, "Pyrometamorphic rocks of the spurrite-merwinite facies as indicators of hydrocarbon discharge zones (the Hatrurim formation, Israel)," *Doklady Earth Sciences*, vol. 420, no. 1, pp. 608–614, 2008.

[18] E. Sokol, I. Novikov, S. Zateeva, Y. E. Vapnik, R. Shagam, and O. Kozmenko, "Combustion metamorphism in the Nabi Musa dome: new implications for a mud volcanic origin of the Mottled Zone, Dead Sea area," *Basin Research*, vol. 22, no. 4, pp. 414–438, 2010.

[19] Y. Kolodny, M. Bar, and E. Sass, "Fission track age of the Mottled Zone event' in Israel," *Earth and Planetary Science Letters*, vol. 11, no. 1-5, pp. 269–272, 1971.

[20] Y. Kolodny, A. Burg, Y. I. Geller, L. Halicz, and Y. Zakon, "Veins in the combusted metamorphic rocks, Israel; weathering or a retrograde event?," *Chemical Geology*, vol. 385, pp. 140–155, 2014.

[21] D. Gur, G. Steinitz, Y. Kolodny, A. Starinsky, and M. McWilliams, "40Ar39Ar dating of combustion metamorphism ("Mottled Zone", Israel)," *Chemical Geology*, vol. 122, no. 1-4, pp. 171–184, 1995.

[22] E. V. Sokol, S. N. Kokh, Y. Vapnik, V. Thiery, and S. A. Korzhova, "Natural analogs of belite sulfoaluminate cement clinkers from Negev desert, Israel," *American Mineralogist*, vol. 99, no. 7, pp. 1471–1487, 2014.

[23] E. Sokol, S. Kokh, V. Sharygin et al., "Mineralogical diversity of Ca_2SiO_4-bearing combustion metamorphic rocks in the Hatrurim basin: implications for storage and partitioning of elements in oil shale clinkering," *Minerals*, vol. 9, no. 8, p. 465, 2019.

[24] E. V. Galuskin, B. Krüger, I. O. Galuskina et al., "Levantite, $KCa_3(Al_2Si_3)O_{11}(PO_4)$, a new latiumite-group mineral from the pyrometamorphic rocks of the Hatrurim basin, Negev desert, Israel," *Mineralogical Magazine*, vol. 83, no. 5, pp. 713–721, 2019.

[25] E. V. Sokol, O. L. Gaskova, S. N. Kokh et al., "Chromatite and its Cr^{3+}- and Cr^{6+}-bearing precursor minerals from the Nabi Musa Mottled Zone complex, Judean Desert," *American Mineralogist*, vol. 96, no. 4, pp. 659–674, 2011.

[26] R. Juroszek, B. Krüger, I. Galuskina, H. Krüger, Y. Vapnik, and E. Galuskin, "Siwaqaite, $Ca_6Al_2(CrO_4)_3(OH)_{12}·26H_2O$, a new mineral of the ettringite group from the pyrometamorphic Daba-Siwaqa complex, Jordan," *American Mineralogist*, vol. 105, no. 3, pp. 409–421, 2020.

[27] F. Hirsch, A. Burg, and Y. Avani, "Geological map of Israel 1:50 000 arade sheet," *Geological Survey*, 2008.

[28] K. Nowak, G. Cametti, I. O. Galuskina, Y. Vapnik, and E. V. Galuskin, "Gismondine-Sr, $Sr_4(Al_8Si_8O_{32})·9H_2O$, a new strontium dominant, orthorhombic zeolite of the gismondine series from the Hatrurim Complex, Israel," *American Mineralogist*, 2022.

[29] G. M. Sheldrick, "A short history of SHELX," *Acta Crystallographica Section A: Foundations of Crystallography*, vol. 64, no. 1, pp. 112–122, 2008.

[30] G. M. Sheldrick, "Crystal structure refinement with *SHELXL*," *Structural Chemistry*, vol. 71, Part 1, pp. 3–8, 2015.

[31] R. X. Fischer, M. Burianek, and R. D. Shannon, "Determination of the H_2O content in minerals, especially zeolites, from their refractive indices based on mean electronic polarizabilities of cations," *European Journal of Mineralogy*, vol. 32, no. 1, pp. 27–40, 2020.

[32] E. Passaglia, "The crystal chemistry of chabazites," *American Mineralogist*, vol. 55, no. 7-8, pp. 1278–1301, 1970.

[33] S. M. Auerbach, K. A. Carrado, and P. K. Dutta, *Handbook osf Zeolite Science and Technology*, M. Dekker, New York, 2003.

[34] J. Čejka, *Introduction to Zeolite Science and Practice*, Elsevier, Amsterdam; Boston, 3rd rev. ed. edition, 2007.

[35] A. W. Chester and E. G. Derouane, *Zeolite Chemistry and Catalysis*, Springer Netherlands, Dordrecht, 2009.

[36] W. Mozgawa, "The relation between structure and vibrational spectra of natural zeolites," *Journal of Molecular Structure*, vol. 596, no. 1-3, pp. 129–137, 2001.

[37] A. C. Gujar, A. A. Moye, P. A. Coghill, D. C. Teeters, K. P. Roberts, and G. L. Price, "Raman investigation of the SUZ-4 zeolite," *Microporous and Mesoporous Materials*, vol. 78, no. 2-3, pp. 131–137, 2005.

[38] Y.-L. Tsai, E. Huang, Y. H. Li et al., "Raman spectroscopic characteristics of zeolite group minerals," *Minerals*, vol. 11, no. 2, p. 167, 2021.

[39] W. Loewenstein, "The distribution of aluminum in the tetrahedra of silicates and aluminates," *American Mineralogist*, vol. 39, no. 1–2, pp. 92–96, 1954.

[40] G. Gottardi, "Topologic symmetry and real symmetry in framework silicates," *Mineralogy and Petrology*, vol. 26, no. 1-2, pp. 39–50, 1979.

[41] G. Gottardi and E. Galli, *Natural zeolites*, Springer Science & Business Media, 1985.

[42] T. Armbruster and E. Gunter, "Crystal structures of natural zeolites," *Reviews in Mineralogy and Geochemistry*, vol. 45, pp. 1–68, 2001.

[43] R. Rinaldi, J. J. Pluth, and J. V. Smith, "Zeolites of the phillipsite family. Refinement of the crystal structures of phillipsite and harmotome," *Acta Crystallographica - Section B: Structural Crystallography & Crystal Chemistry*, vol. 30, no. 10, pp. 2426–2433, 1974.

[44] A. F. Gualtieri, E. Passaglia, E. Galli, and A. Viani, "Rietveld structure refinement of Sr-exchanged phillipsites," *Microporous and Mesoporous Materials*, vol. 31, no. 1–2, pp. 33–43, 1999.

[45] G. D. Gatta and Y. Lee, "Anisotropic elastic behaviour and structural evolution of zeolite phillipsite at high pressure: a synchrotron powder diffraction study," *Microporous and Mesoporous Materials*, vol. 105, no. 3, pp. 239–250, 2007.

61:5494898858

[46] Y. I. Geller, A. Burg, L. Halicz, and Y. Kolodny, "System closure during the combustion metamorphic "Mottled Zone" event, Israel," *Chemical Geology*, vol. 334, pp. 25–36, 2012.

[47] R. Juroszek, B. Krüger, K. Banasik, Y. Vapnik, and I. Galuskina, "Raman spectroscopy and structural study of baryte-hashemite solid solution from pyrometamorphic rocks of the Hatrurim Complex, Israel," *Spectrochimica Acta Part A: Molecular and Biomolecular Spectroscopy*, vol. 205, pp. 582–592, 2018.

[48] A. Langella, P. Cappelletti, and M. de' Gennaro, "Zeolites in closed hydrologic systems," *Reviews in Mineralogy and Geochemistry*, vol. 45, pp. 235–257, 2001.

[49] J. M. R. Trian, R. J. F. Herrera, R. C. A. Rios et al., "Natural zeolites filling amygdales and veins in basalts from the British Tertiary Igneous Province on the Isle of Skye, Scotland," *Earth Sciences Research Journal*, vol. 16, no. 1, pp. 41–53, 2012.

[50] D. Novembre, D. Gimeno, P. Cappelletti, and S. F. Graziano, "A case study of zeolitization process: "Tufo Rosso a Scorie Nere" (Vico volcano, Italy): inferences for a general model," *European Journal of Mineralogy*, vol. 33, no. 3, pp. 315–328, 2021.

[51] R. H. Mariner and R. C. Surdam, "Alkalinity and formation of zeolites in saline alkaline lakes," *Science*, vol. 170, no. 3961, pp. 977–980, 1970.

[52] E. Passaglia, G. Vezzalini, and R. Carnevali, "Diagenetic chabazites and phillipsites in Italy: crystal chemistry and genesis," *European Journal of Mineralogy*, vol. 2, no. 6, pp. 827–840, 1990.

[53] S. J. Chipera and J. A. Apps, "Geochemical Stability of Natural Zeolites," *Reviews in Mineralogy and Geochemistry*, vol. 45, pp. 117–157, 2001.

[54] M. Kousehlar, T. B. Weisenberger, F. Tutti, and H. Mirnejad, "Fluid control on low-temperature mineral formation in volcanic rocks of Kahrizak, Iran," *Geofluids*, vol. 12, no. 4, p. 311, 2012.

[55] A. E. Milodowski, L. Trotignon, H. Khoury et al., "The Analogue Cement ZOne (ACZ)," in *a Natural Analog Study of Cement Buffered, Hyperalkaline Groundwaters and their Interaction with a Repository Host Rock IV: An Examination of the Khushaym Matruk (Central Jordan) and Maqarin (Northern Jordan) Sites, Chapter 4*, NDA, Moors Row, U.K, 2011.

[56] S. Spürgin, T. B. Weisenberger, and M. Marković, "Zeolite-group minerals in phonolite-hosted deposits of the Kaiserstuhl volcanic complex, Germany," *American Mineralogist*, vol. 104, no. 5, pp. 659–670, 2019.

[57] P. C. Piilonen, G. Poirier, W. Lechner, R. Rowe, and R. P. Richards, "Zeolite minerals from Wat Ocheng, Ta Ang, Ratanakiri Province, Cambodia – occurrence, composition, and paragenesis," *The Canadian Mineralogist*, vol. 60, no. 1, pp. 133–153, 2022.

Gismondine-Sr, $Sr_4(Al_8Si_8O_{32})\cdot9H_2O$, a new strontium dominant, orthorhombic zeolite of the gismondine series from the Hatrurim Complex, Israel

Katarzyna Skrzyńska[1,*,§], **Georgia Cametti**[2,†], **Irina O. Galuskina**[1,‡], **Yevgeny Vapnik**[3], **and Evgeny V. Galuskin**[1]

[1]Institute of Earth Sciences, Faculty of Natural Sciences, University of Silesia, Będzińska 60, 41-200 Sosnowiec, Poland
[2]Institute of Geological Sciences, University of Bern, Baltzerstrasse 1+3, 3012 Bern, Switzerland
[3]Department of Geological and Environmental Sciences, Ben-Gurion University of the Negev, POB 653, Beer-Sheva 84105, Israel

Abstract

A new mineral, gismondine-Sr with ordered gismondine framework type [$B22_12$ no. 20, $Z = 1$; $a = 14.0256(2)$ Å, $b = 10.45900(10)$ Å, $c = 13.79360(10)$ Å, $V = 2023.44(4)$ Å³] and the ideal chemical formula $Sr_4(Si_8Al_8O_{32})\cdot9H_2O$ was discovered in amygdaloidal voids of partly melted gehlenite hornfels at Halamish locality, Hatrurim Basin of the Hatrurim Complex, Negev Desert, Israel. Gehlenite hornfels is mainly composed of gehlenite, wollastonite, and garnet of the grossular-andradite-schorlomite series. In a low-temperature association occur minerals such as thomsonite-Ca, flörkeite, analcime and minerals of the tobermorite supergroup. Gismondine-Sr forms spherulitic aggregates up to 180 μm and, rarely, pseudotetragonal bipyramidal crystals up to 50 μm. Empirical crystal-chemical formula of gismondine-Sr is $(Sr_{2.02}Ca_{1.09}Ba_{0.02}K_{0.72}Na_{0.62})_{\Sigma4.47}Al_{7.91}Si_{8.09}O_{31.85}\cdot9H_2O$. It is the strontium analog of gismondine-Ca and the second orthorhombic zeolite with the **GIS** structure topology. Crystals are transparent to translucent and feature vitreous luster. The mineral exhibits a white color, imperfect cleavage in [101] direction, a brittle tenacity, and uneven fracture. The Mohs hardness was estimated at approximately 4. Gismondine-Sr is biaxial negative, $\alpha = 1.488(3)$, $\beta = 1.492(3)$, $\gamma = 1.495(3)$, $2V_{obs} = 70$–$80°$. The Raman spectrum is characterized by a band at 465 cm⁻¹, which is also the main band in gismondine-Ca. The structure refinement using SC-XRD ($R_1 = 0.0353$) reveals the ordered distribution of framework cations and the disordered arrangement of extraframework cations. The aluminosilicate framework is built by crankshaft chains with 8-membered apertures channels parallel to [101] and [10$\bar{1}$]. In gismondine-Sr, the 8-membered rings are elliptically deformed and the T-O-T angle of the upward and downward tetrahedra in the double crankshaft chains is smaller compared to that for gismondine-Ca. Consequently, a slight rotation of the double crankshaft chains has been noticed. Similar observations have been made in partially dehydrated and the pressure-modified gismondine-Ca. The present study suggests that, in addition to high-pressure and dehydration, the elliptical deformation of the channels in **GIS** also arises as a consequence of the extraframework cations and H_2O content. Thus, the extraframework content influences the aluminosilicate framework leading to the orthorhombic symmetry.

Keywords: Zeolite, **GIS** topology, gismondine, Raman, crystal structure, Hatrurim; Microporous Materials: Crystal-chemistry, Properties, and Utilizations

Introduction

Gismondine-Sr (IMA2021-043), $Sr_4(Si_8Al_8O_{32})\cdot9H_2O$ [$B22_12$, $a = 14.0256(2)$, $b = 10.45900(10)$, $c = 13.79360(10)$ Å, $V = 2023.44(4)$ Å³] is a new strontium dominant, orthorhombic analog of gismondine. In turn, gismondine has been renamed to gismondine-Ca and gismondine has become the series name (Miyawaki et al. 2021). Gismondine-Sr was found in amygdaloidal voids in gehlenite pyrometamorphic rocks of the Hatrurim Complex at Halamish Wadi, Hatrurim Basin, Negev Desert, Israel. Gismondine-Sr and other minerals with **GIS** framework type (Table 1) show a structure built by double

connected 4-membered ring crankshaft chains (Gottardi 1979; Gottardi and Galli 1985; Armbruster and Gunter 2001), which are also present in phillipsite (**PHI**) and merlinoite (**MER**) framework types (Fig. 1). The following seven mineral species are included in gismondine subgroup (Table 1): gismondine-Ca, gismondine-Sr, amicite, garronite-Ca, garronite-Na, and gobbinsite. "Gismondine-Ba" described from artificial material is not approved by the Commission on New Minerals, Nomenclature, and Classification-International Mineralogical Association (CNMNC-IMA) (Braithwaite et al. 2001). The highest symmetry of the **GIS** framework topology corresponding to the tetragonal $I4_1/amd$ space group was found in the high-silica synthetic zeolite $Na_{3.6}(A1_{3.6}Si_{12.4})O_{32}\cdot14H_2O$, $a = 9.9989(4)$, $c = 10.0697(4)$ Å, $V = 1006.75$ Å³ (Baerlocher and Meier 1972; Håkansson et al. 1990). The topological symmetry of the framework is reduced to orthorhombic due to the cations ordering at the tetrahedral

---
* E-mail: katarzyna.skrzynska@us.edu.pl. Orcid 0000-0001-5816-9958
† Orcid 0000-0002-3186-3074
‡ Orcid 0000-0001-9373-9274
§ Special collection papers can be found online at http://www.minsocam.org/MSA/AmMin/special-collections.html.

TABLE 1. Zeolite species with gismondine (**GIS**) framework structure

Name	Gismondine-Ca	Gismondine-Sr	"Gismondine-Ba"	Garronite-Ca	Garronite-Na	Amicite	Gobbinsite
IMAFormula	$Ca_2(Al_4Si_4O_{16})$ $\times 8H_2O$	$Sr_4(Al_8Si_8O_{32})$ $\times 9H_2O$	$Ba_4(Al_8Si_8O_{32})$ $\times 12H_2O$	$Ca_3(Al_6Si_{10}O_{32})$ $\times 14H_2O$	$Na_6(Al_6Si_{10}O_{32})$ $\times 8.5H_2O$	$K_2Na_2(Al_4Si_4O_{16})$ $\times 5H_2O$	$Na_5(Al_5Si_{11}O_{32})$ $\times 11H_2O$
Space group	$P2_1/c$	$B22_12$	monoclinic	$I\bar{4}m2$	$I2$	$I2$	$Pmn2_1$
a (Å)	10.02	13.794	14.896	9.927	9.990	10.226	10.104
b (Å)	10.62	14.026	9.951	9.927	10.032	10.422	9.782
c (Å)	9.84	10.459	7.613	10.303	10.036	9.884	10.152
α (°)	90	90	90	90	90	90	90
β (°)	92.42	90	103.25	90	90.11	88.32	90
γ (°)	90	90	90	90	90	90	90
V (Å³)	1046.2	2023.44	1098.42	1015.3	1005.8	1051.7	1003.4
References	Fischer 1963; Grice et al. 2016	This work	Braithwaite et al 2001; Grice et al. 2016	Grice et al. 2016	Grice et al. 2016	Alberti and Vezzalini 1979; Grice et al. 2016	Gatta et al. 2010

sites. Further lowering of the symmetry may occur due to the extraframework cation arrangement (Gottardi and Galli 1985; Armbruster and Gunter 2001). The synthetic monoclinic strontium gismondine was obtained by ion exchange from Na-zeolite (Allen et al. 2002).

The new mineral, gismondine-Sr (IMA2021-043), as well as its name, has been approved by the CNMNC-IMA. The new mineral and the name gismondine-Sr are consistent with the criteria of the new mineral species definition in the zeolite group, clearly specified in "Recommended nomenclature for zeolite minerals: report of the subcommittee on zeolites of the International Mineralogical Association, Commission on New Minerals and Mineral Names" (Coombs et al. 1997). The holotype material is deposited at the mineralogical collection of the Fersman Mineralogical Museum in Moscow, Russia, with the catalog number 97678 for the thin section and 97679 for the rock sample.

The aim of this paper is a detailed description of a recently discovered gismondine-Sr, its structure, and the genetic aspects of zeolite mineralization in pyrometamorphic rocks of the Hatrurim Complex.

EXPERIMENTAL METHODS

The semi-quantitative chemical composition of gismondine-Sr, as well as its morphology, was studied using a scanning electron microscope Phenom XL, equipped with an energy-dispersive X-ray spectrometer (Faculty of Natural Science, University of Silesia, Poland). The quantitative chemical analyses were carried out with a microprobe analyzer CAMECA SX100 (Institute of Geochemistry, Mineralogy and Petrology, University of Warsaw, Poland) at 15 kV and 10 nA; spot size was defocused to 5 μm. A larger spot size has not been used because of the relatively small grain size. The following lines and standards were used: $NaK\alpha$ = albite; $SiK\alpha$ = diopside; $AlK\alpha$ = orthoclase; $KK\alpha$ = orthoclase; $CaK\alpha$ = diopside; $FeK\alpha$ = Fe_2O_3; $SrL\alpha$ = celestine; $BaL\alpha$ = baryte.

Raman spectrum was obtained on a confocal Raman Microscope WITec α300R (Faculty of Natural Science, University of Silesia, Poland), equipped with an air-cooled 488 nm laser and a CCD camera working at –61 °C. The Raman signal was recorded with an optical fiber 30 μm in diameter and a monochromator with a 600 mm^{-1} grating. The laser power was ≈10 mW on the sample surface. The time of measurement was 3 s with an accumulation of 25 scans and a spectral resolution of 3 cm^{-1}. The monochromator was calibrated using the Raman scattering line of a silicon plate (520.7 cm^{-1}). Spectral software package GRAMS (Galactic Industries Corporation, New Hampshire, U.S.A.) was used for data processing. The fitting of Raman bands was performed using a Gauss-Lorentz cross-product function with preservation of the rule of the minimum number of component bands.

Diffraction data were collected using a Rigaku Synergy-S diffractometer equipped with a dual micro-focused source and a Hypix detector. $CuK\alpha$ radiation (λ = 1.540598 Å) was chosen because of the small size of the crystals (0.07 × 0.04 × 0.03 mm). Preliminary lattice parameters and the orientation matrix were obtained from three sets of frames. Final diffraction data were collected with ω scans at different φ settings. The software package CrysalisPro 40.29a was used for data reduction and absorption correction. The structure was solved by direct methods using SHELXS (Sheldrick 2008). The structural refinement was carried out by using SHELXL (Sheldrick 2015) and neutral atomic scattering factors for all atoms. The structure was refined as an inversion twin, with fractional volume contribution expressed by the BASF parameter (Sheldrick 2015) equal to 0.16(4). The CIF[1] has been deposited.

Because gismondine-Sr occurs only in small concentrations and forms intergrowth with other zeolites, it was not possible to collect experimental X-ray powder diffraction data (PXRD). The PXRD pattern has been calculated more reliably from the results of the single-crystal structure refinement using PowderCell 2.4 program (Kraus and Nolze 1996). The calculated patterns of gismondine-Sr and gismondine-Ca (Wadoski-Romeijn and Armbruster 2013) are given in Online Materials[1] Tables S1 and S2, respectively. The distinction
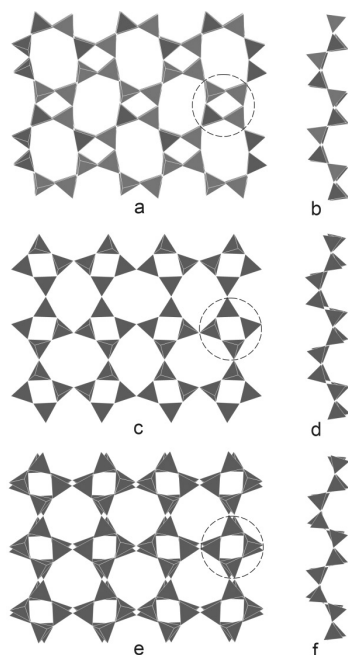
FIGURE 1. Zeolites with framework built by double connected 4-membered rings. (**a**) **GIS** framework type projected on (100), the dashed circle line point out a double crankshaft chain parallel to [100]. (**b**) Double crankshaft chain of **GIS** framework type (gismondine-Ca; Wadoski-Romeijn and Armbruster 2013). (**c**) **MER** framework type projected on (001), the dashed circle line point out a double crankshaft chain parallel to [001]. (**d**) Double crankshaft chain of **MER** framework type (merlinoite; Galli et al. 1979). (**e**) **PHI** framework type projected on (100), the dashed circle line point out a double crankshaft chain parallel to [100]. (**f**) Double crankshaft chain of **PHI** framework type (phillipsite; Gatta et al. 2009).
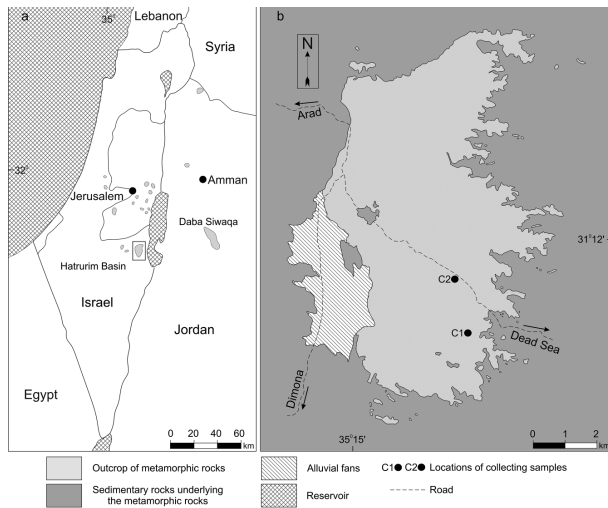
Figure 2. (**a**) Schematic map of the pyrometamorphic rocks outcrops in Israel, Palestinian Autonomy and Jordan; Fragment outlined by frame is magnified in **b**. (**b**) Map of the Hatrurim Basin with marked locations of sampling: wadi Halamish outcrops (C1), wadi Zohar (C2) [created on the basis of Geological Map of Israel 1:50 000, Arad sheet (Hirsch et al. 2008)].

between orthorhombic and monoclinic symmetry of gismondine is possible using the powder diffraction patterns.

Geological settings and paragenesis

The Hatrurim Complex, known as Mottled Zone, is composed of high-temperature metamorphic rocks and products of their low-temperature alteration spread on both sides of the Dead Sea Transform Fault in Israel, Palestine Autonomy, and Jordan (Fig. 2a; Bentor 1960; Gross 1977; Burg et al. 1992, 2000). High-temperature rocks are represented by spurrite marble, larnite pseudoconglomerates and gehlenite hornfelses formed at the sanidinite facies conditions after sedimentary protolith. Until now, despite many mineralogical studies over the last ten years, there is no scientific consensus on the genesis of these rocks. The most disputable issue is the source of heat energy. One of the theories establishes that the heat energy accrues from the combustion of bituminous chalk organic matter (Gross 1977; Geller et al. 2012; Galuskina et al. 2014). The latest conception associates the origin of pyrometamorphic processes with neotectonic mud volcanism and methane burning (Sokol et al. 2008, 2010; Novikov et al. 2013; Galuskina et al. 2014). Previous investigations showed that during formation of high-temperature rocks, the earlier formed minerals ("clinker association") react with combustion by-products, leading to a significantly greater variety of mineral species (Galuskina et al. 2014, 2017; Galuskin et al. 2015, 2016).

The pyrometamorphic rocks contain cracks, voids, and veins filled by low-temperature minerals formed due to hydrothermal alteration and weathering (Kolodny et al. 2014; Juroszek et al. 2020; Kruszewski et al. 2021). Gismondine-Sr was found in small amygdaloidal voids of partially melted gehlenite hornfels at wadi Halamish locality (N31°09′42″ E35°17′29″), which is located at the southern part of the Hatrurim Basin, the larg-

est exposed field of pyrometamorphic rocks of the Hatrurim Complex in Israel (Burg et al. 1992, 2000; Vapnik et al. 2007; Geller et al. 2012). The investigated material was collected in a marginal part of gray basalt-like gehlenite-wollastonite paralava, which contains sulfide globules. These pyrometamorphic rocks occur as irregular lenses low-T calcium-hydrosilicate rocks, and stratigraphically they correspond to the lower part of the Ghareb Formation (Sharygin et al. 2008, 2013). Hornfels is composed of gehlenite, wollastonite, rankinite, and garnet of the grossular-andradite-schorlomite series (Fig. 3). Accessory minerals are represented by fluorapatite, perovskite, minerals of magnesioferrite-trevorite-magnetite-maghemite series, and hematite (Fig. 3). Additionally, in amygdaloidal voids occur other zeolites such as gismondine-Ca, thomsonite-Ca, and two generations of flörkeite forming before and after gismondine-Sr (Fig. 3c). Analcime and minerals of the tobermorite supergroup,
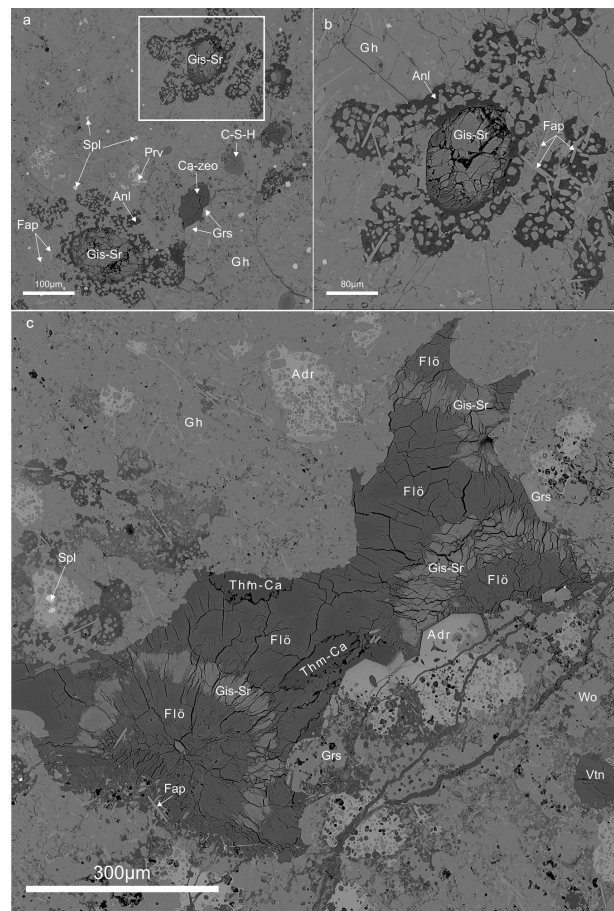
Figure 3. (**a**) Gehlenite-wollastonite-garnet hornfels with small voids filled by zeolite including gismondine-Sr. Fragment outlined by frame is magnified in **b**. (**b**) Gismondine-Sr with gismondine-Ca (most probably) rim in amygdule, around which analcime occurs with an irregular distribution. (**c**) Zone of gismondine-Sr in spherulite aggregates between two flörkeite generations. BSE images. Anl = analcime; Adr = andradite; Ca-zeo = calcium zeolite; C-S-H = hydrated calcium silicates; Fap = fluorapatite; Flö = flörkeite;, Gh = gehlenite; Grs = grossular; Prv = perovskite; Spl = spinel; Vtn = vertumnite; Wo = wollastonite; Gis-Sr = gismondine-Sr; Thm-Ca = thomsonite-Ca. (Color online.)

which surrounded the voids, are also present in association (Fig. 3b).

Furthermore, gismondine-Sr was found in voids of gehlenite hornfels from Zohar Wadi near the road Arad-Dead Sea (Fig. 2b). The association of main minerals is similar for both localities.

PHYSICAL AND OPTICAL PROPERTIES OF GISMONDINE-SR

Gismondine-Sr forms spherulitic aggregates up to 180 µm in the largest dimension filling amygdaloidal voids (Fig. 3c). Pseudotetragonal bipyramidal crystals up to 50 µm are rarely observed. Its color and streak are white. Crystals are transparent to translucent and feature vitreous luster. It does not exhibit fluorescence. Imperfect cleavage is observed in the [101] direction. The tenacity is brittle, and the fracture is uneven. The Mohs hardness was estimated at ~4, and the mean micro-hardness is 302(8) kg/mm^2. The range is 289–325 kg/mm^2 with VHN loaded 25 g. Gismondine-Sr is gradually dissolved in 10% HCl. Measurements of density could not be performed because of a large number of microcracks and a high degree of hydration. Density, $D_{calc} = 2.301$ g·cm^{-3}, was calculated on the basis of the empirical formula of the holotype and the unit-cell volume refined from the SC-XRD data. Pleochroism is not observed. Gismondine-Sr is negative biaxial, $\alpha = 1.488(3)$, $\beta = 1.492(3)$, $\gamma = 1.495(3)$, $2V_{obs} = 70–80°$, $2V_{calc} = 81.8°$. Dispersion is weak. The optical orientation is consistent with the cell vectors. The Gladstone-Dale compatibility index is based on the empirical values of the oxides, and the calculated H$_2$O content is $1 – (K_P/K_C) = –0.004$ (superior) (Mandarino 1981).

CHEMICAL COMPOSITION

The results of EMPA chemical analysis are presented in Table 2. The empirical formula is calculated on the basis of 16 T-sites within the framework. The water content was calculated based on stoichiometry, which is consistent with the SC-XRD data. The empirical formula of gismondine-Sr

TABLE 2. Chemical composition of gismondine-Sr

Constituent	C1			C2		
	Mean	s.d.	Range	Mean	s.d	Range
wt%	n = 14			n = 7		
SiO$_2$	34.93	0.56	34.14–36.02	35.37	0.64	34.10–35.89
Al$_2$O$_3$	28.99	0.38	28.61–29.96	29.53	0.48	28.59–30.14
CaO	4.38	0.43	3.75–5.49	4.73	0.23	4.39–5.03
SrO	15.06	0.62	14.10–16.57	13.56	0.75	12.14–14.42
BaO	0.26	0.11	0.08–0.50	0.39	0.08	0.29–0.50
Na$_2$O	1.38	0.25	0.80–1.83	1.13	0.19	0.89–1.39
K$_2$O	2.45	0.35	1.42–2.84	2.77	0.13	2.66–3.03
H$_2$O	11.66			11.84		
Total	99.11			99.32		
Si	8.09			8.06		
Al	7.91			7.94		
T	16.00			16.00		
Sr	2.02			1.79		
Ca	1.09			1.15		
Ba	0.02			0.03		
K	0.72			0.81		
Na	0.62			0.50		
Extraframework cations	4.47			4.28		
H$_2$O	9.00			9.00		
R	0.51			0.50		
E %	4.08			9.66		

Notes: s.d. = standard deviation; C1 = Halamish locality; C2 = Zohar locality; $R = \frac{Si}{Si + Al + Fe}$; E-balance error $= \frac{Al + Fe^{3+} - Al_{theor}}{Al_{theor}} \times 100$; $Al_{theor} = K + Na + 2Ca + 2Sr + 2Ba$ (Passaglia 1970); water content was calculated based on the SC-XRD data.
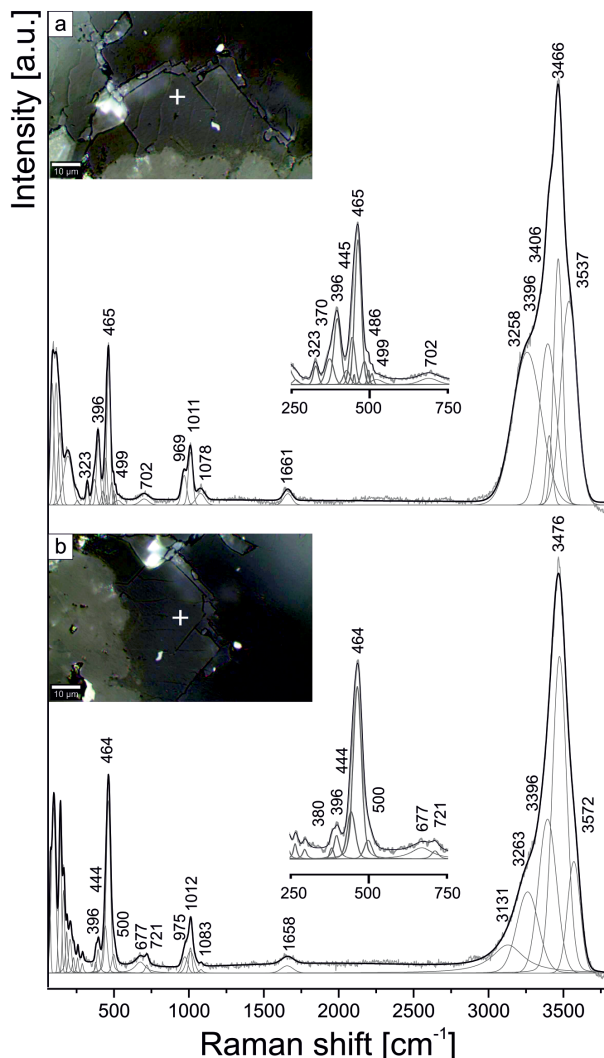
FIGURE 4. (**a** and **b**) Raman spectra of gismondine-Sr in two orientations. (Color online.)

from the type locality (symbol C1 in Table 2) could be written as: $(Sr_{2.02}Ca_{1.09}Ba_{0.02}K_{0.72}Na_{0.62})_{\Sigma4.47}Al_{7.91}Si_{8.09}O_{31.85}\cdot9H_2O$. The empirical formula of gismondine-Sr from Zohar (C2 in Table 2) is as follows: $(Sr_{1.79}Ca_{1.15}Ba_{0.03}K_{0.81}Na_{0.50})_{\Sigma4.28}Al_{7.93}Si_{8.05}O_{31.62}\cdot9H_2O$. The end-member formula of gismondine-Sr is $Sr_4Al_8Si_8O_{32}\cdot9H_2O$ (see Discussion).

RAMAN SPECTROSCOPY

The Raman spectra of gismondine-Sr are presented in Figure 4. The main bands and their assignments are given in Table 3. The range 323–500 cm^{-1} corresponds to symmetric bending vibrations of T-O-T in rings (Dutta and Del Barco 1988; Dutta et al. 1991; Knops-Gerrits et al. 1997; Yu et al. 2001; Mozgawa et al. 2005). Variations in band intensity, depending on the crystal orientation, are visible in this range (Figs. 4a and 4b), for example, the band at 396 cm^{-1}. Bands between 671 and 721 cm^{-1} could be attributed to symmetric stretching modes T-O-T (Yu et al. 2001; Mozgawa et al. 2005). Bands related to symmetric and antisymmetric stretching vibrations of T-O in

TABLE 3. Observed frequencies and their assignments in Raman spectra of gismondine-Sr

Raman bands (in cm⁻¹)	Assignments
323, 396, 444, 465, 499, 500	symmetric bending vibrations of T-O-T
677, 702, 721	symmetric stretching modes T-O-T
969, 975, 1011, 1012, 1078, 1083	symmetric and antisymmetric stretching vibrations of T-O in tetrahedra
1658, 1661	bending vibrations of water molecules
3131, 3258, 3263, 3396, 3396, 3406, 3466, 3476, 3537, 3572	stretching vibrations of water molecules

TABLE 4. Parameters for X-ray data collection and crystal-structure refinement

Crystal data	
Empirical formula	$Sr_{4.99}Ca_{1.52}K_{1.78}Na_{1.46}Si_{16}Al_{16}O_{82.36}$
Crystal system	Orthorhombic
Space group	$B22_12$
Unit-cell dimensions (Å)	$a = 14.0256(2)$
	$b = 10.45900(10)$
	$c = 13.79360(10)$
Volume (Å³)	2023.44(4)
Z	1
Structure refinement	
Reflections collected	11164
Independent reflections	2171
Observed data [$I > 2\sigma(I)$]	2133
R_1, wR_2 [$I > 2\sigma(I)$]	0.0353 (wR = 0.0988)
R_1, wR_2 (for all)	0.0359 (wR = 0.0996)
GooF	1.085
$\Delta\rho_{min}$ [e/Å⁻³]	−0.34
$\Delta\rho_{max}$ [e/Å⁻³]	0.72

tetrahedra are in the range 969–1083 cm⁻¹ (Dutta and Del Barco 1988; Dutta et al. 1991; Knops-Gerrits et al. 1997; Yu et al. 2001; Gujar et al. 2005). Other bands in the spectrum are assigned to water molecules. The band around 1660 cm⁻¹ corresponds to bending vibrations, and bands between 3130 and 3600 cm⁻¹ are attributed to stretching vibrations of water (Tsai et al. 2021).

TABLE 5. Atom coordinates (x,y,z), equivalent isotropic displacement parameters (U_{iso}, Å²) and site occupancies

Site	Atom	x	y	z	U_{eq}/U_{iso} (Å²)	Occupancy
C1	Sr	−0.1760(3)	−0.2145(2)	0.09992(19)	0.0305(9)	0.311(8)
C1A	Ca	−0.227(3)	−0.179(3)	0.1148(15)	0.049(9)	0.088(13)
C1B	Na	−0.203(3)	−0.202(4)	0.063(4)	0.100	0.18(2)
C1C	K	−0.148(2)	−0.293(4)	0.105(2)	0.100	0.113(7)
C2	Sr	−0.39918(16)	0.0323(2)	0.18035(18)	0.0385(10)	0.312(5)
C2A	Ca	−0.3805(8)	0.0744(11)	0.2377(9)	0.025(5)	0.101(9)
C2B	K	−0.428(3)	0.043(5)	0.226(3)	0.096(14)	0.107(15)
Si1	Si	0.0000	0.0000	0.43045(11)	0.0132(3)	1
Si2	Si	−0.23632(8)	0.28200(11)	0.16565(8)	0.0129(3)	1
Si3	Si	0.0000	0.0000	0.09934(11)	0.0134(4)	1
Al1	Al	−0.07829(13)	0.2500	0.0000	0.0138(4)	1
Al2	Al	0.10644(13)	0.2500	0.5000	0.0148(4)	1
Al3	Al	−0.15755(9)	0.03249(12)	0.26528(9)	0.0139(3)	1
O1	O	−0.1444(3)	0.3011(4)	0.0980(3)	0.0355(10)	1
O2	O	0.0954(3)	0.0120(4)	0.1624(3)	0.0292(8)	1
O3	O	−0.0876(3)	0.0519(4)	0.3665(3)	0.0316(9)	1
O4	O	−0.3285(3)	0.2375(4)	0.1060(3)	0.0315(9)	1
O5	O	−0.2179(3)	0.1760(4)	0.2489(3)	0.0330(9)	1
O6	O	−0.2443(3)	−0.0838(4)	0.2785(3)	0.0296(8)	1
O7	O	0.0025(3)	−0.1251(4)	0.0313(2)	0.0275(8)	1
O8	O	0.0350(2)	0.1143(4)	0.5004(3)	0.0276(8)	1
W1	O	−0.3975(9)	0.0528(12)	0.3721(8)	0.066(4)	0.545(18)
W1A	O	−0.5000	0.0000	0.344(3)	0.073(15)	0.23(3)
W2	O	−0.2518(13)	−0.0228(18)	0.0161(13)	0.076(8)	0.350(19)
W3	O	−0.4874(10)	0.2274(15)	0.2498(10)	0.049(5)	0.359(17)
W4	O	−0.3740(16)	−0.1865(19)	0.1058(17)	0.053(7)	0.33(3)
W4A	O	−0.345(2)	−0.210(3)	0.068(3)	0.048(11)	0.20(3)
W4B	O	−0.351(4)	−0.2500	0.0000	0.08(2)	0.21(4)
W4C	O	−0.441(2)	−0.126(3)	0.168(2)	0.083(10)	0.28(2)

The gismondine-Sr Raman spectrum confirms the gismondine structure topology (Tsai et al. 2021; Fig. 4).

CRYSTALLOGRAPHY AND STRUCTURE DESCRIPTION

The crystal structure of gismondine-Sr [$B22_12$, $a = 14.0256(2)$ Å, $b = 10.45900(10)$ Å, $c = 13.79360(10)$ Å, $V = 2023.44(4)$ Å³] was refined from the SC-XRD data. Details of the experiment and parameters of structure refinement are given in Table 4. The reflections were indexed in a C-centered orthorhombic lattice. After data reduction, the analysis of the intensities pointed to the space group $C222_1$(#20). The non-standard setting $B22_12$ was chosen for similarity with the unit cell of a high-temperature modification of gismondine (Vezzalini et al. 1993; Wadoski-Romeijn and Armbruster 2013). First, the framework atoms (Si, Al, O) were located. According to chemical analysis (Si/Al = 1) and Löewenstein rule (Löewenstein 1954), Si and Al are orderly distributed at distinct tetrahedral sites (Si1, Si2, Si3 and Al1, Al2, Al3, for Si and Al, respectively; Table 5), which were assigned to

TABLE 6. Selected interatomic distances (Å)

Site 1	Site 2	Distance (Å)	Site 1	Site 2	Distance (Å)
Si1	O3	1.607(4)×2	Al1	O1	1.724(4)×2
	O8	1.613(4)×2		O7	1.739(4)×2
	mean	1.610		mean	1.732
Si2	O1	1.604(4)	Al2	O8	1.737(4)×2
	O4	1.602(4)		O4	1.729(4)×2
	O6	1.624(4)		mean	1.733
	O5	1.617(4)	Al3	O3	1.719(4)
	mean	1.612		O6	1.730(4)
Si3	O2	1.601(4)×2		O2	1.729(4)
	O7	1.611(4)×2		O5	1.738(4)
	mean	1.606		mean	1.729
C1	W1	2.670(13)	C2	W1	2.654(12)
	W2	2.548(18)		W1A	2.68(4)
	W4	2.79(2)		W3	2.571(15)
	W4A	2.41(3)		W4	2.53(2)
	W4B	2.84(4)		W4C	*1.76(3)*
	O2	2.550(5)		W4C	2.45(3)
	O5	2.806		O8	2.783(5)
	O7	2.835		mean	2.490
	mean	2.635	C2A	W1	*1.883(17)*
C1A	W2	2.16(3)		W3	2.200(19)
	W4	2.07(4)		W1A	2.36(3)
	W4A	1.80(4)		W4C	2.45(3)
	W4B	2.47(4)		W4C	2.74(3)
	O2	2.624(19)		mean	2.327
	mean	2.225	C2B	W1	2.06(4)
C1B	W4A	*1.99(5)*		W1A	*1.96(6)*
	W2	2.10(5)		W3	2.13(4)
	W4B	2.30(7)		W4C	*1.94(5)*
	W4	2.47(5)		W4C	2.18(5)
	W4A	2.84(7)		mean	2.054
	mean	2.34	C2	C2A	*0.942(12)*
C1C	W1	*1.77(4)*		C2B	*0.76(5)*
	W2	2.94(4)		C2B	2.62(5)
	W3	2.77(3)	C2B	C2	2.62(5)
	W4A	2.94(5)		C2A	2.95(6)
	O5	2.77(3)		C2B	2.20(10)
	mean	2.638	C2A	C2B	*0.77(4)*
C1	C1A	*0.83(4)*		C2B	2.95(6)
	C1B	*0.65(5)*		C1C	2.61(4)
	C1B	2.44(5)	C1B	C1	2.44(5)
	C1C	*0.91(4)*		C1A	2.77(7)
C1A	C1B	*0.82(5)*		C1B	2.01(10)
	C1B	2.77(7)		C1C	*1.35(6)*
	C1C	*1.63(6)*		C1C	2.45(6)
	Si2	3.10(2)			
C1C	C1B	2.45(6)			
	C2A	2.61(4)			
	C1	2.86(3)			

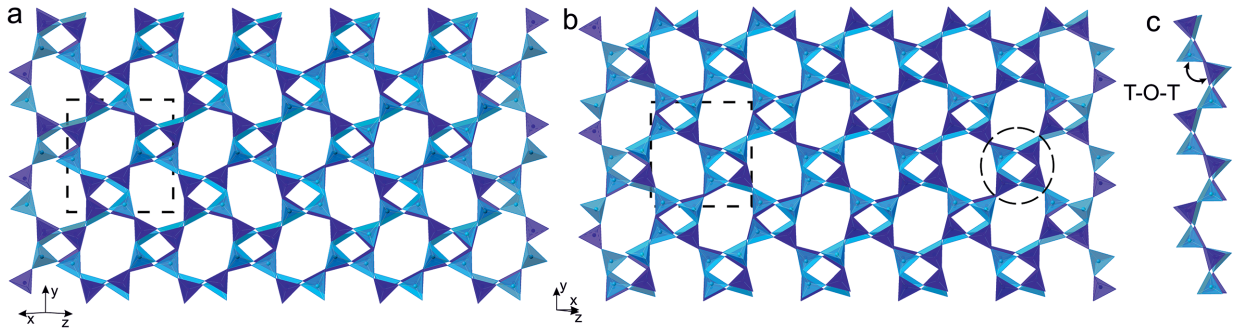*Note:* Non-occurring short distances are reported in italic.

FIGURE 5. The framework of gismondine-Sr structure: (**a**) projection on (101); (**b**) projection on (10$\bar{1}$), dashed circle indicates double crankshaft chain (*dcc*); (**c**) *dcc* running parallel to [10$\bar{1}$] with the marked T-O-T angle between the tetrahedra up and down. Silica tetrahedra are dark blue and alumina tetrahedra are light blue, dashed line shows the unit cell. (Color online.)

the basis of interatomic T-O distances [mean distances T(Al)-O = 1.73 Å and T(Si)-O = 1.61 Å; Table 6]. Framework oxygen atoms occupy eight sites: O1-O8 (Table 5). After the first cycle of refinement, two strong peaks appeared in difference-Fourier maps. These peaks were added to the structural model (*C*1 and *C*2 sites) and refined with Sr scattering factors. Additional residual electron density was found very close (distances in the range of 0.5–1.0 Å) to the *C*1 and *C*2 sites. Such residual electron density was modeled by low-occupied sites (*C*1A, *C*1B, *C*1C and *C*2A, *C*2B) refined with Ca, Na, and K scattering factors, respectively (Table 5). The assignment of atomic species to each crystallographic site was not straightforward due to the structural disorder and the low population of these sites. The best model, which was consistent with the chemical composition, achieved the quality of the structural refinement $R_1 = 0.0353$.

    GIS structure is composed of 4-membered rings tetrahedra, which form double crankshaft chains (defined as *dcc*, Fig. 5). The *dcc* chains are connected to each other and create double

4-membered rings, which result in two systems of channels with 8-membered ring apertures. These channels run parallel to [101] and [10$\bar{1}$] (Fig. 5), and they are connected by 2_1 axes parallel to [010]. At the intersection of two system channels occur *t-gsm* cavities, which are built by six 4-membered rings and four 8-membered rings (notation 4^68^4) (Figs. 6 and 7; Alberti and Vezzalini 1979).

    In gismondine-Sr, extraframework cations and H$_2$O are disorderly distributed at partially occupied sites in the *t-gsm* cavity (Fig. 6; Table 5). Strontium is the dominant extraframework cation, located at sites *C*1 and *C*2 within two adjacent cages, respectively. Each of these cages hosts 0.6 Sr disordered over two symmetry-equivalent sites (Figs. 6b, 7a, and 7b), whose simultaneous occupation is prevented due to the excessively short distances between them (~2.8 Å; Table 6). The remaining extraframework cations (Ca, K, and Na) do not equally distribute between two adjacent *t-gsm* cavities (Fig. 6b). One cavity is occupied by Ca, Na, and K at *C*1A, *C*1B, and *C*1C, respectively
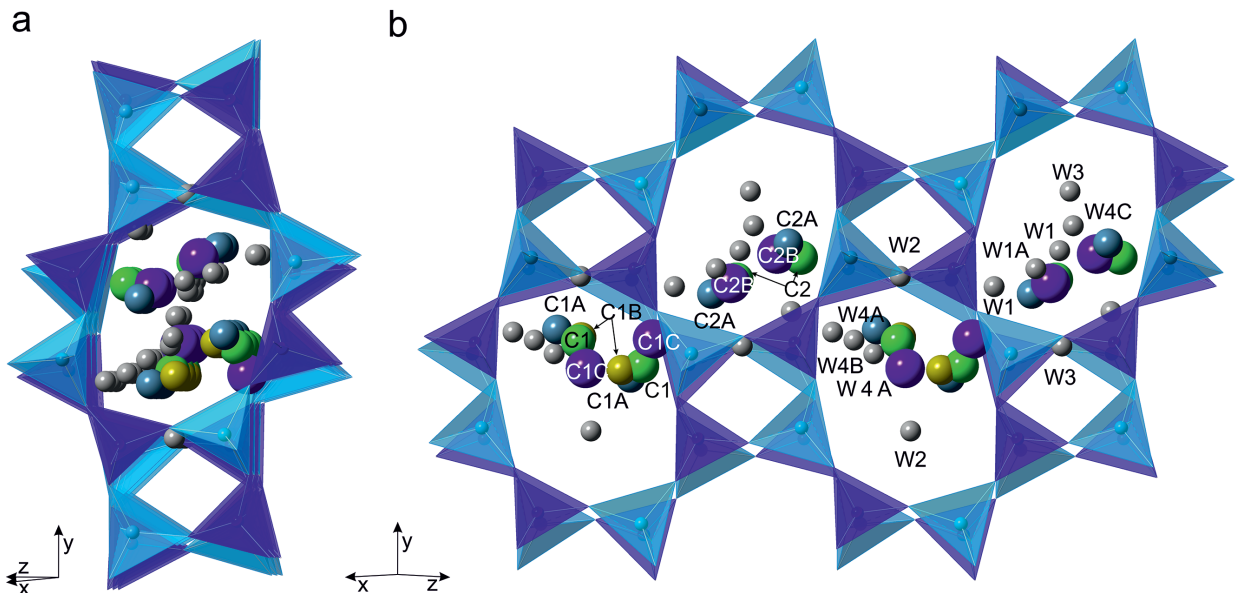

FIGURE 6. (**a**) General view of the 8-membered rings channel, projected along [10$\bar{1}$]. (**b**) Cations and H$_2$O distributed into four adjacent *t-gsm* cavities, projected along [101]. All extraframework sites are partially occupied. Strontium, calcium, potassium, and sodium are represented as green, blue, purple, and yellow spheres, respectively. Gray spheres represent H$_2$O sites. (Color online.)
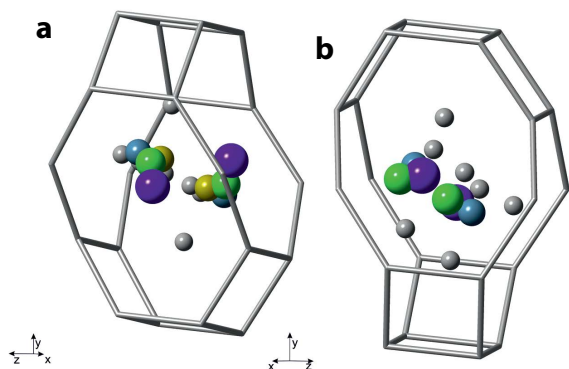
FIGURE 7. Exraframework cations population in the two non-equivalent symmetry cages: (**a**) cage containing Ca, Na, and K at C1A, C1B, and C1C, respectively; (**b**) cage containing Ca and K at *C*2A and *C*2B sites. All extraframework sites are partially occupied. Strontium, calcium, potassium, and sodium are represented as green, blue, purple, and yellow spheres, respectively. Gray spheres represent H$_2$O sites. (Color online.)


FIGURE 8. Part of the framework containing 8- and 4-membered rings. (**a**) Gismondine-Ca projection along [00$\bar{1}$] (Wadoski-Romeijn and Armbruster 2013). (**b**) Gismondine-Sr projection along [101]. (**c**) Partially dehydrated gismondine-Ca at 75 °C along [101] (Wadoski-Romeijn and Armbruster 2013). (**d**) Scheme of overlapping double 4-member ring of gismondine-Ca (gray line) and gismondine-Sr (dashed line). (Color online.)

(Fig. 7a), whereas the adjacent one by Ca and K at *C*2A and *C*2B sites, respectively (Fig. 7b; Table 5). Thus, although the refined occupancy of *C*1 and *C*2 converged to the same value, the arrangement of other cations (K, Ca, and Na) slightly differs, and the two adjacent *t-gsm* cavities are not symmetry-equivalent. H$_2$O is also disordered at partially occupied eight sites (Table 5), which have no simultaneous full occupancy because of the excessively short distances from each other.

TABLE 7. Comparison parameters of gismondine-Sr structure with literature data for gismondine-Ca

	Gismondine-Sr This work	Gismondine-Ca Wadoski-Romeijn and Armbruster 2013		Gismondine-Ca 75 °C Wadoski-Romeijn and Armbruster 2013	
Lattice parameters					
Chemical formula	Sr$_4$(Si$_8$Al$_8$O$_{32}$) × 9H$_2$O	Ca$_4$(Si$_8$Al$_8$O$_{32}$) × 18H$_2$O		Ca$_4$(Si$_8$Al$_8$O$_{32}$) × 12H$_2$O	
Space group	*B*22$_1$2	*P*2$_1$/*c*		*P*2$_1$2$_1$2$_1$	
a	14.0256(2)	10.0214(1)		10.1035(15)	
b	10.45900(10)	10.5997(1)		9.7819(10)	
c	13.79360(10)	9.8327(1)		10.1523(9)	
β		92.363			
V	2023.44(4)	1043.58(2)		1985.6(2)	
Channel size					
[101]		[100]		[101]	
O5-O7	2.90	O8-O8	2.70	O16-O12	2.62
O2-O1	4.57	O3-O3	4.90	O5-O4	4.72
Ellipticity ratio	0.63		0.55		0.55
[10$\bar{1}$]		[001]		[10$\bar{1}$]	
O6-O8	2.91	O7-O6	3.14	O2-O14	2.90
O4-O3	4.58	O2-O4	4.49	O7-O10	4.466
Ellipticity ratio	0.64	Ellipticity ratio	0.70	Ellipticity ratio	0.62
T-O-T angle of the crankshaft chain					
Si3-O7-Al1	140.21	Si2-O5-Al1	146.54	Si1-O12-Al2	143.68
Si1-O8-Al2	141.19	Si2-O6-Al1	145.75	Si4-O14-Al4	143.52
Si2-O6-Al3	140.84	Si1-O7-Al2	142.43	Si4-O11-Al1	137.14
Si2-O5-Al3	139.67	Si1-O8-Al2	138.55	Si3-O8-Al3	133.32
				Si2-O16-Al1	129.16
				Si2-O2-Al2	130.53
				Si2-O15-Al4	143.30
				Si3-O13-Al3	142.19
mean T-O-T angle	140.47	mean T-O-T angle	143.32	mean T-O-T angle	137.85

Note: Channel sizes were measured according to the free diameter reported in the *Atlas of Zeolites Framework Types* ellipticity ratio was measured using the free diameter as the ratio of the short diagonal to the long diagonal (Baerlocher et al. 2007).
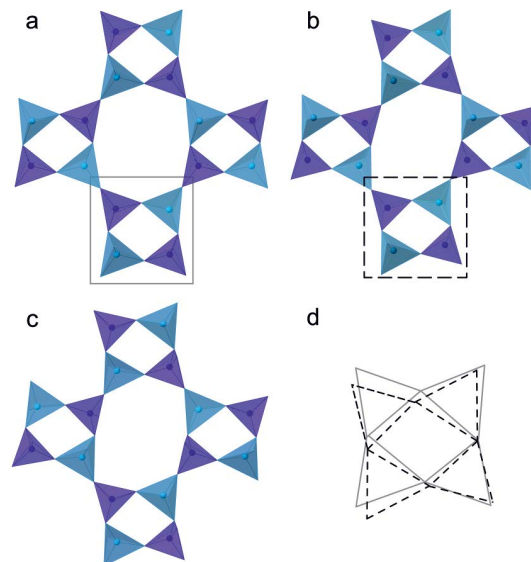
DISCUSSION

Gismondine-Sr is one of the few zeolites which contain strontium as the dominant extraframework cation and the first strontium zeolite with the **GIS** framework type (Gottardi 1979; Gottardi and Galli 1985; Smith 1988; Armbruster and Gunter 2001; Baerlocher et al. 2007). After gobbinsite, gismondine-Sr is the second **GIS** zeolite, with the orthorhombic symmetry (Gatta et al. 2010). The unit cell of gismondine-Sr is related to the monoclinic cell of gismondine-Ca by the matrix transformation 101/010/10$\bar{1}$, which corresponds to rotation by an angle of 45° around the b axis and leads to an increase in the a and c parameters. As a result, gismondine-Sr has almost doubled the unit-cell volume with respect to gismondine-Ca (Table 7; Vezzalini et al. 1993). Both gismondine-Ca and gismondine-Sr are characterized by an ordered Si/Al distribution of the tetrahedral framework. However, within the channels of gismondine-Sr the extraframework cations and H$_2$O molecules are disorderly distributed (Tables 5 and 6; Figs. 5 and 6).

The comparison of gismondine-Sr and gismondine-Ca frameworks showed that T-O-T angle between the upward and downward tetrahedra in the double crankshaft chains is smaller in gismondine-Sr (Figs. 1b and 4b; mean T-O-T angle in gis-Sr: 140.47; mean T-O-T angle in gis-Ca: 143.32). However, no significant changes in the value of angles in the 4-membered rings building the double crankshaft chains have been observed, suggesting their quasi-rigid behavior. In contrast to gismondine-Ca, in gismondine-Sr the ellipticity ratio in the two 8-membered channels is similar (Table 7). Consequently, a slight rotation of the double crankshaft chains in gismondine-Sr was observed (Fig. 8). The tilting occurs around bridging O atoms between the upward and downward tetrahedra in the double crankshaft

chain, which behaves as hinges within the framework (Figs. 1b and 4b; Gatta and Lee 2014). The framework of gismondine-Sr is similar to partially dehydrated gismondine-Ca (Vezzalini et al. 1993; Wadoski-Romeijn and Armbruster 2013; Fig. 8c). Moreover, deformations of partially dehydrated gismondine-Ca are similar to deformations of pressure-induced gismondine-Ca, which was reported by Betti et al. (2007) and Ori et al. (2008). The ellipticity of the 8-membered channels increases with the degree of dehydration or pressure, respectively. Moreover, the decrease of the T-O-T angle of the crankshaft chain was also observed (Vezzalini et al. 1993; Betti et al. 2007; Fig. 8c). The Raman spectrum of gismondine-Sr shows no change in the main band, which vibrates at 465 cm^{-1} (Table 3) as in the case of gismondine-Ca. Thus, in agreement with the quasi-rigid behavior of the 4-membered rings, the main band could be attributed to T-O-T vibration of the 4-member rings. Furthermore, its frequency is independent of the T-O-T angle in the double crankshaft chains (Table 7; Fig. 4). The bands from 8-membered rings could appear in the spectrum (Fig. 4) at 396 cm^{-1} (Dutta and Del Barco 1988; Dutta et al. 1991; Knops-Gerrits et al. 1997; Yu et al. 2001). Its variations of intensity (Figs. 4a and 4b) could be related to the orientation of the channels with regard to the laser beam.

Zeolites of the gismondine group (Table 1) reveal different extraframework cations and different Si/Al ratios. Gismondine-Ca, amicite and gismondine-Sr stand out from this group by the Si/Al ratio equal to one (Passaglia and Sheppard 2001). The isomorphic substitution scheme of gismondine-Ca for gismondine-Sr is as follows: $Ca^{2+} \rightarrow Sr^{2+}$. Additionally, the experimental data indicate monoclinic symmetry for the pure strontium gismondine (Allen et al. 2002), as is the case with gismondine-Ca and gismondine-Ba (Fischer 1963; Braithwaite et al. 2001). However, the content of the monovalent cations in the composition of the investigated gismondine-Sr is significantly different compared to gismondine-Ca, in which monovalent cations are present in negligible amounts (Vezzalini and Oberti 1984). The presence of roughly equal content of K and Na in the composition of the holotype gismondine-Sr, $(Sr_{2.02}Ca_{1.09}Ba_{0.02}K_{0.72}Na_{0.62})_{\Sigma4.47}Al_{7.91}Si_{8.09}O_{31.85} \cdot 9H_2O$ is indicative of formal existence of a solid solution between gismondine-Sr and amicite $K_4Na_4(Al_8Si_8O_{32}) \cdot 10H_2O$. Based on the end-member formulas of gismondine-Ca $Ca_4(Al_8Si_8O_{32}) \cdot 16H_2O$, gismondine-Sr $Sr_4(Al_8Si_8O_{32}) \cdot 9H_2O$ and amicite $K_4Na_4(Al_8Si_8O_{32}) \cdot 10H_2O$, the scheme of the substitutions could be presented as follows: $H_2O + Ca^{2+}/Sr^{2+} \rightarrow 2(Na^+/K^+)$. Thus, besides monoclinic symmetry, gismondine-Sr without monovalent extraframework cations is characterized by a higher water content compared to the presented data. The general zeolite formula with the gismondine framework type and Si/Al ratio equal to one could be: $(D_xM)_{4-8}(Al_8Si_8O_{32}) \cdot nH_2O$, where M is monovalent and D is divalent cations. The simplified formula of gismondine-Sr derived from the EMPA and structural data can be presented as $(D_{3.1}M_{1.8})_{\Sigma4.9}(Al_8Si_8O_{32}) \cdot 9H_2O$, i.e., the $D_4(Al_8Si_8O_{32}) \cdot 9H_2O$ end-member is more than 77%. Strontium is significantly predominant over calcium at the D site, so the ideal formula of gismondine-Sr would be $Sr_4(Al_8Si_8O_{32}) \cdot 9H_2O$.

Based on the filling voids (Fig. 3c), the sequence of zeolite crystallization in the voids of gehlenite-wollastonite paralava could be presented as thomsonite-Ca, $NaCa_2(Al_5Si_5O_{20}) \cdot 6H_2O$ (**THO** framework); flörkeite, $K_3Ca_2Na(Al_8Si_8O_{32} \cdot 12H_2O$ (**PHI** framework); gismondine-Sr, $Sr_4(Al_8Si_8O_{32}) \cdot 9H_2O$ (**GIS** framework) and again flörkeite. Moreover, analcime, $Na(AlSi_2O_6) \cdot H_2O$ (**ANA** framework) is the last zeolite of the crystallization sequence in pyrometamorphic rocks of the Hatrurim Complex. The presented sequence implies that the formation of gismondine-Sr is conditioned by a one-time appearance of high Sr content in the crystallization environment. The association of flörkeite and gismondine-Sr suggests very low-temperature (<100 °C) conditions of crystallization of these zeolites (Lengauer et al. 2009).

The controversial question is the origin of the strontium in the environment. As shown by Geller et al. (2012) and Sokol et al. (2014, 2019), the sedimentary rocks, protolith of gehlenite hornfels, contain carbonates enriched with strontium. We suggest that during processes of pyrometamorphism, strontium from carbonates has been released. The relatively elevated strontium content was recorded in bulk analyses of pyrometamorphic rocks, but it is rather dispersed in rock-forming minerals, especially in fluorapatite-fluorellestadite and baryte (Juroszek et al. 2018; Sokol et al. 2019).

IMPLICATIONS

Zeolites are the most common microporous materials in nature. They are characterized by selective cation-exchange capacity, reversible hydration and dehydration, catalytic activity, and sorption of molecules induced by pressure, the investigation of which has seen rapid development in the past decade (Gatta 2003; Betti et al. 2007; Ori et al. 2008; Arletti et al. 2017; Gatta et al. 2018). Zeolites with **GIS** framework type are used as detergent builders (Adams et al. 1995, 1997), and they received attention because of the high framework flexibility (Betti et al. 2007; Gatta and Lee 2014; Arletti et al. 2017; Chukanov et al. 2020). Nevertheless, despite many studies on zeolite synthesis and ion exchange properties, literature data on Sr^{2+} in **GIS** are scarce (Taylor 1964; Mimura and Akiba 1993; Dyer et al. 2006; Kwon et al. 2021).

Previously conducted high-pressure experiments showed that the deformation mechanisms of the structure are conditioned by the topological configuration of the aluminosilicate framework (Gatta 2003; Gatta and Lee 2014; Gatta et al. 2018). However, the influence of the Si/Al distribution and the extraframework cations on the deformation has not been investigated in detail. The channel content is also responsible for the compressibility of the cavities and, therefore, can lead to different deformation mechanisms under non-ambient conditions. The present study suggested that, in addition to high pressure and dehydration (Vezzalini et al. 1993; Wadoski-Romeijn and Armbruster 2013; Gatta and Lee 2014), the elliptical deformation of the channels in **GIS** also arises as a consequence of the extraframework cations and H_2O content. In conclusion, the extraframework content, i.e., the type of extraframework cations in *t-gsm* cages of gismondine-Sr, influences the aluminosilicate framework leading to the orthorhombic symmetry. In general, the gismondine framework type is extraordinarily flexible and could sorb ions with a wide range of ionic radii at the expense of changing framework symmetry.

REFERENCES CITED

Adams, C.J., Araya, A., Carr, S.W., Chapple, A.P., Graham, P., Minihan, A.R., and Osinga, T.J. (1995) Zeolite map: A new detergent builder. In H.G. Karge and J. Weitkamp, Eds., Studies in Surface Science and Catalysis, 98, 206–207. Elsevier.

Adams, C.J., Araya, A., Carr, S.W., Chapple, A.P., Franklin, K.R., Graham, P., Minihan, A.R., Osinga, T.J., and Stuart, J.A. (1997) Zeolite map: The new detergent zeolite. In H. Chon, S-K. Ihm, and Y.S. Uh, Eds., Studies in Surface Science and Catalysis, 105, p. 1667–1674. Elsevier.

Alberti, A., and Vezzalini, G. (1979) The crystal structure of amicite, a zeolite. Acta Crystallographica, B35, 2866–2869.

Allen, S., Carr, S., Chapple, A., Dyer, A., and Heywood, B. (2002) Ion exchange in the synthetic gismondine, zeolite MAP. Physical Chemistry Chemical Physics, 4, 2409–2415.

Arletti, R., Giacobbe, C., Quartieri, S., and Vezzalini, G. (2017) The influence of the framework and extraframework content on the high pressure behavior of the GIS type zeolites: The case of amicite. Minerals, 7, 18.

Armbruster, T., and Gunter, E. (2001) Crystal Structures of Natural Zeolites. In D.L. Bish and D.W. Ming, Eds., Natural Zeolites: Occurrence, Properties, Applications, 45, p. 1–68. Reviews in Mineralogy and Geochemistry, Mineralogical Society of America, Chantilly, Virginia.

Baerlocher, C., and Meier, W.M. (1972) The crystal structure of synthetic zeolite Na-P 1, an isotype of gismondine. Zeitschrift für Kristallographie, 135, 339–354.

Baerlocher, C., McCusker, L.B., and Olson, D.H. (2007) Atlas of Zeolite Framework Types, 6th revised ed., 398 p. Elsevier.

Bentor, Y.K. (1960) Israel. Lexique Stratigraphique International: Asie fascicule 10 c 2 Israel. Centre National de la Recherche Scientifique, 3.

Betti, C., Fois, E., Mazzucato, E., Medici, C., Quartieri, S., Tabacchi, G., Vezzalini, G., and Dmitriev, V. (2007) Gismondine under HP: Deformation mechanism and re-organization of the extra-framework species. Microporous and Mesoporous Materials, 103, 190–209.

Braithwaite, R.S.W., Dyer, A., and Wilson, J.I. (2001) Gismondine-Ba, a zeolite from the weathering of slag. Journal of the Russell Society, 7, 83–85.

Burg, A., Starinsky, A., Bartov, Y., and Kolodny, Y. (1992) Geology of the Hatrurim Formation ("Mottled Zone") in the Hatrurim basin. Israel Journal of Earth Sciences, 40, 107–124.

Burg, A., Kolodny, Y., and Lyakhovsky, V. (2000) Hatrurim-2000: The "Mottled Zone" revisited, forty years later. Israel Journal of Earth Sciences, 48, 209–223.

Chukanov, N.V., Kazheva, O.N., Chervonnaya, N.A., Varlamov, D.A., Ermolaeva, V.N., Pekov, I.V., and Shilov, G.V. (2020) Ion-exchange properties of the natural zeolite amicite. Macedonian Journal of Chemistry and Chemical Engineering, 39, 207.

Coombs, D., Alberti, A., Armbruster, T., Artioli, G., Colella, C., Galli, E., Grice, J.D., Liebau, F., Mandarino, J.A., Minato, H., and others. (1997) Recommended nomenclature for zeolite minerals: Report of the subcommittee on zeolites of the international mineralogical association, commission on new minerals and mineral names. The Canadian Mineralogist, 35, 1571–1606.

Dutta, P.K., and Del Barco, B. (1988) Raman spectroscopy of zeolite A: Influence of silicon/aluminum ratio. The Journal of Physical Chemistry, 92, 354–357.

Dutta, P.K., Rao, K.M., and Park, J.Y. (1991) Correlation of Raman spectra of zeolites with framework architecture. The Journal of Physical Chemistry, 95, 6654–6656.

Dyer, A., Heywood, B., and Szyrokyj, N. (2006) Cation exchange in the synthetic gismondine-zeolite MAP. Microporous and Mesoporous Materials, 92, 161–164.

Fischer, K. (1963) The crystal structure determination of the zeolite gismondite CaAl$_2$Si$_2$O$_8$4H$_2$O. Mineralogical Notes, 664–672.

Galli, E., Gottardi, G., and Pongiluppi, D. (1979) The crystal structure of the zeolite merlinoite. Neues Jahrbuch für Mineralogie, Monatshefte, 1–9.

Galuskin, E.V., Gfeller, F., Armbruster, T., Galuskina, I.O., Vapnik, Y., Murashko, M., Włodyka, R., and Dzierżanowski, P. (2015) New minerals with a modular structure derived from hatrurite from the pyrometamorphic Hatrurim Complex. Part I. Nabimusaite, KCa$_{12}$(SiO$_4$)$_4$(SO$_4$)$_2$O$_2$F, from larnite rocks of Jabel Harmun, Palestinian Autonomy, Israel. Mineralogical Magazine, 79, 1061–1072.

Galuskin, E.V., Galuskina, I.O., Gfeller, F., Krüger, B., Kusz, J., Vapnik, Y., Dulski, M., and Dzierżanowski, P. (2016) Silicocarnotite, Ca$_5$[(SiO$_4$)(PO$_4$)](PO$_4$), a new "old" mineral from the Negev Desert, Israel, and the ternesite-silicocarnotite solid solution: Indicators of high-temperature alteration of pyrometamorphic rocks of the Hatrurim Complex, Southern Levant. European Journal of Mineralogy, 28, 105–123.

Galuskina, I.O., Vapnik, Y., Lazic, B., Armbruster, T., Murashko, M., and Galuskin, E.V. (2014) Harmunite CaFe$_2$O$_4$: A new mineral from the Jabel Harmun, West Bank, Palestinian Autonomy, Israel. American Mineralogist, 99, 965–975.

Galuskina, I.O., Galuskin, E.V., Vapnik, Y., Prusik, K., Stasiak, M., Dzierżanowski, P., and Murashko, M. (2017) Gurimite, Ba$_3$(VO$_4$)$_2$ and hexacelsian, BaAl$_2$Si$_2$O$_8$—two new minerals from schorlomite-rich paralava of the Hatrurim Complex. Mineralogical Magazine, 81, 1009–1019.

Gatta, G. (2003) New insights on high-pressure behaviour of microporous materials from X-ray single-crystal data. Microporous and Mesoporous Materials, 61, 105–115.

Gatta, G.D., and Lee, Y. (2014) Zeolites at high pressure: A review. Mineralogical Magazine, 78, 267–291.

Gatta, G.D., Cappelletti, P., Rotiroti, N., Slebodnick, C., and Rinaldi, R. (2009) New insights into the crystal structure and crystal chemistry of the zeolite phillipsite. American Mineralogist, 94, 190–199.

Gatta, G.D., Birch, W.D., and Rotiroti, N. (2010) Reinvestigation of the crystal structure of the zeolite gobbinsite: A single-crystal X-ray diffraction study. American Mineralogist, 95, 481–486.

Gatta, G.D., Lotti, P., and Tabacchi, G. (2018) The effect of pressure on open-framework silicates: Elastic behaviour and crystal–fluid interaction. Physics and Chemistry of Minerals, 45, 115–138.

Geller, Y.I., Burg, A., Halicz, L., and Kolodny, Y. (2012) System closure during the combustion metamorphic "Mottled Zone" event, Israel. Chemical Geology, 334, 25–36.

Gottardi, G. (1979) Topologic symmetry and real symmetry in framework silicates. Mineralogy and Petrology, 26, 39–50.

Gottardi, G., and Galli, E. (1985) Natural Zeolites, 412 p. Springer.

Grice, J.D., Rowe, R., and Poirier, G. (2016) Garronite-Na, a new zeolite species from Mont Saint-Hilaire, Québec. Canadian Mineralogist, 54, 1549–1562.

Gross, S. (1977) The mineralogy of the Hatrurim Formation, Israel. Geological Survey of Israel Bulletin, 70.

Gujar, A.C., Moye, A.A., Coghill, P.A., Teeters, D.C., Roberts, K.P., and Price, G.L. (2005) Raman investigation of the SUZ-4 zeolite. Microporous and Mesoporous Materials, 78, 131–137.

Håkansson, U., Fälth, L., and Hansen, S. (1990) Structure of a high-silica variety of zeolite Na-P. Acta Crystallographica, C46, 1363–1364.

Hirsch, F., Burg, A., and Avani, Y. (2008) Geological Map of Israel 1:50 000 Arade Sheet 15-IV. Geological Survey.

Juroszek, R., Krüger, B., Banasik, K., Vapnik, Y., and Galuskina, I. (2018) Raman spectroscopy and structural study of baryte-hashemite solid solution from pyrometamorphic rocks of the Hatrurim Complex, Israel. Spectrochimica Acta Part A: Molecular and Biomolecular Spectroscopy, 205, 582–592.

Juroszek, R., Krüger, B., Galuskina, I., Krüger, H., Vapnik, Y., and Galuskin, E. (2020) Siwaqaite, Ca$_6$Al$_2$(CrO$_4$)$_3$(OH)$_{12}$·26H$_2$O, a new mineral of the ettringite group from the pyrometamorphic Daba-Siwaqa complex, Jordan. American Mineralogist, 105, 409–421.

Knops-Gerrits, P.-P., De Vos, D.E., Feijen, E.J.P., and Jacobs, P.A. (1997) Raman spectroscopy on zeolites. Microporous Materials, 8, 3–17.

Kolodny, Y., Burg, A., Geller, Y.I., Halicz, L., and Zakon, Y. (2014) Veins in the combusted metamorphic rocks, Israel; Weathering or a retrograde event. Chemical Geology, 385, 140–155.

Kraus, W., and Nolze, G. (1996) POWDER CELL—a program for the representation and manipulation of crystal structures and calculation of the resulting X-ray powder patterns. Journal of Applied Crystallography, 29, 301–303.

Kruszewski, Ł., Palchik, V., Vapnik, Y., Nowak, K., Banasik, K., and Galuskina, I. (2021) Mineralogical, geochemical, and rock mechanic characteristics of zeolite-bearing rocks of the Hatrurim Basin, Israel. Minerals, 11, 1062.

Kwon, S., Kim, C., Han, E., Lee, H., Cho, H.S., and Choi, M. (2021) Relationship between zeolite structure and capture capability for radioactive cesium and strontium. Journal of Hazardous Materials, 408, 124419.

Lengauer, C.C., Kolitsch, U., and Tillmanns, E. (2009) Flörkeite, K$_3$Ca$_2$Na [Al$_8$Si$_8$O$_{32}$]·12H$_2$O, a new phillipsite-type zeolite from the Bellerberg, East Eifel volcanic area, Germany. European Journal of Mineralogy, 21, 901–913.

Löewenstein, W. (1954) The distribution of aluminum in the tetrahedra of silicates and aluminates. American Mineralogist, 39, 92–69.

Mandarino, J.A. (1981) The Gladstone-Dale relationship. IV. The compatibility concept and its application. Canadian Mineralogist, 19, 441–450.

Mimura, H., and Akiba, K. (1993) Adsorption behavior of cesium and strontium on synthetic zeolite P. Journal of Nuclear Science and Technology, 30, 436–443.

Miyawaki, R., Hatert, F., Pasero, M., and Mills, S. (2021) Newsletter 63. Mineralogical Magazine, 85, 910–915.

Mozgawa, W., Jastrzębski, W., and Handke, M. (2005) Vibrational spectra of D4R and D6R structural units. Journal of Molecular Structure, 744-747, 663–670.

Novikov, I., Vapnik, Y., and Safonova, I. (2013) Mud volcano origin of the Mottled Zone, South Levant. Geoscience Frontiers, 4, 597–619.

Ori, S., Quartieri, S., Vezzalini, G., and Dmitriev, V. (2008) Pressure-induced over-hydration and water ordering in gismondine: A synchrotron powder diffraction study. American Mineralogist, 93, 1393–1403.

Passaglia, E. (1970) The crystal chemistry of chabazites. American Mineralogist, 55, 1278–1301.

Passaglia, E., and Sheppard, A. (2001) The crystal chemistry of zeolites. In D.L. Bush and D.W. Ming, Eds., Natural Zeolites: Occurrence, properties, applications, 45, 69–116. Reviews in Mineralogy and Geochemistry, Mineralogical Society of America, Chantilly, Virginia.

Sharygin, V.V., Lazic, B., Armbruster, T.M., Murashko, M.N., Wirth, R., Galuskina, I.O., Galuskin, E.V., Vapnik, Y., Britvin, S.N., and Logvinova, A.M. (2013) Shulamitite $Ca_3TiFe^{3+}AlO_8$—A new perovskite-related mineral from Hatrurim Basin, Israel. European Journal of Mineralogy, 25, 97–111.

Sharygin, V.V., Sokol, E.V., and Vapnik, Y. (2008) Minerals of the pseudobinary perovskite-brownmillerite series from combustion metamorphic larnite rocks of the Hatrurim Formation (Israel). Russian Geology and Geophysics, 49, 709–726.

Sheldrick, G.M. (2008) A short history of SHELX. Acta Crystallographica, A64, 112–122.

——— (2015) Crystal structure refinement with SHELXL. Acta Crystallographica, C71, 3–8.

Smith, J.V. (1988) Topochemistry of zeolites and related materials. 1. Topology and geometry. Chemical Reviews, 88, 149–182.

Sokol, E.V., Novikov, I.S., Zateeva, S.N., Sharygin, V.V., and Vapnik, Y. (2008) Pyrometamorphic rocks of the spurrite-merwinite facies as indicators of hydrocarbon discharge zones (the Hatrurim formation, Israel). Doklady Earth Sciences, 420, 608–614.

Sokol, E., Novikov, I., Zateeva, S., Vapnik, Y., Shagam, R., and Kozmenko, O. (2010) Combustion metamorphism in the Nabi Musa dome: new implications for a mud volcanic origin of the Mottled Zone, Dead Sea area: Combustion metamorphism in the Nabi Musa dome. Basin Research, 22, 414–438.

Sokol, E.V., Kokh, S.N., Vapnik, Y., Thiery, V., and Korzhova, S.A. (2014) Natural analogs of belite sulfoaluminate cement clinkers from Negev Desert, Israel. American Mineralogist, 99, 1471–1487.

Sokol, E., Kokh, S., Sharygin, V., Danilovsky, V., Seryotkin, Y., Liferovich, R., Deviatiiarova, A., Nigmatulina, E., and Karmanov, N. (2019) Mineralogical diversity of Ca_2SiO_4-bearing combustion metamorphic rocks in the Hatrurim Basin: Implications for storage and partitioning of elements in oil shale clinkering. Minerals, 9, 465.

Taylor, A.M. (1964) Zeolite studies IV: Na-P zeolites and the ion exchanged derivatives of tetragonal Na-P. American Mineralogist, 49, 656–682.

Tsai, Y.L., Huang, E., Li, Y.-H., Hung, H.-T., Jiang, J.-H., Liu, T.-C., Fang, J.-N., and Chen, H.-F. (2021) Raman Spectroscopic Characteristics of Zeolite Group Minerals. Minerals, 11, 167.

Vapnik, Y., Sharygin, V.V., Sokol, E.V., and Shagam, R. (2007) Paralavas in a combustion metamorphic complex Hatrurim Basin, Israel. In G.B. Stracher, Ed., Geology of Coal Fires: Case Studies from Around the World. Geological Society of America.

Vezzalini, G., and Oberti, R. (1984) The crystal chemistry of gismondines: The non-existence of K-rich gismondines. Bulletin de Minéralogie, 107, 805–812.

Vezzalini, G., Quartieri, S., and Alberti, A. (1993) Structural modifications induced by dehydration in the zeolite gismondine. Zeolites, 13, 34–42.

Wadoski-Romeijn, E., and Armbruster, T. (2013) Topotactic transformation and dehydration of the zeolite gismondine to a novel Ca feldspar structure. American Mineralogist, 98, 1988–1997.

Yu, Y., Xiong, G., Li, C., and Xiao, F.-S. (2001) Characterization of aluminosilicate zeolites by UV Raman spectroscopy. Microporous and Mesoporous Materials, 46, 23–34.

Endnote:

CAMBRIDGE
UNIVERSITY PRESS

Article

New data on minerals with the **GIS** framework-type structure: gismondine-Sr from the Bellerberg volcano, Germany, and amicite and Ba-rich gismondine from the Hatrurim Complex, Israel

Katarzyna Skrzyńska[1] ⓘ, Georgia Cametti[2], Rafał Juroszek[1] ⓘ, Christof Schäfer[3] and Irina Galuskina[1] ⓘ

[1]University of Silesia, Faculty of Natural Sciences, Institute of Earth Sciences, Sosnowiec 41-200, Poland; [2]University of Bern, Institute of Geological Science, Bern 3012, Switzerland; and [3]Independent researcher, Untereisesheim, 74257, Germany

Abstract

Gismondine-Sr, recently discovered in the Hatrurim Complex in Israel, has been recognised in a xenolith sample from the Bellerberg volcano in Germany. The empirical crystal-chemical formula indicates elevated K content: $(Sr_{1.74}Ca_{1.05}Ba_{0.09}K_{1.56}Na_{0.49})_{\Sigma 4.93}$ $[Al_{7.98}Si_{8.06}O_{32}]\cdot 9.62H_2O$. Additionally, Ba-rich gismondine and amicite have been found in the low-temperature mineral association of the pyrometamorphic rock from the Hatrurim Complex. The Raman spectra of the studied zeolites and the crystal structure of gismondine-Sr from the second occurrence are presented. A review of zeolites with **GIS** framework-type structure leads to the following conclusions: (1) garronite-Na and gobbinsite are equivalent and constitute a solid solution with garronite-Ca; (2) gismondine-Ca, -Sr, and amicite belong to one mineral series; (3) two zeolites series with different R-factors (defined as Si/(Si+Al+Fe)) can be distinguished within **GIS** topology: the garronite series ($R > 0.6$) including garronite-Ca and gobbinsite, with general formula $(M_y D_{0.5(x-y)})$ $[Al_x Si_{(16-x)}O_{32}]\cdot nH_2O$, where M and D refer to monovalent and divalent cations, respectively; and the gismondine series, including amicite, gismondine-Sr and gismondine-Ca, with $R \approx 0.5$, and the general formula $(M_y D_{0.5(8-y)})[Al_8 Si_8 O_{32}]\cdot nH_2O$. The Raman band between $475\ cm^{-1}$ and $485\ cm^{-1}$ is distinctive for the garronite series, whereas the band around $460\ cm^{-1}$ is characteristic of the gismondine series. On the basis of these findings, a revision of **GIS** zeolites nomenclature is suggested.

Introduction

Zeolites are one of the most complex mineral groups in terms of crystal structure and crystal chemistry (Armbruster and Gunter, 2001), which leads to several difficulties in unambiguously defining a zeolite mineral species. Guidelines for nomenclature and distinction rules for new zeolite species by Coombs *et al.* (1997) recommend that zeolites with the same topological framework, exhibiting a wide variety of extra-framework cations form a series. The end-members of the series are defined on the basis of the most abundant extra-framework cation in atomic proportions. The disparity in Si:Al ratio, the different hydration levels (i.e. content of H_2O), differences in space-group symmetry, and order–disorder distributions of cations at the tetrahedral sites are not sufficient criteria to distinguish a new zeolite mineral species. However, there may be exceptions to all of these rules. Coombs *et al.* (1997) give an example of gismondine-Ca, $Ca_4[Al_8 Si_8 O_{32}]$ $\cdot 16H_2O$, and garronite-Ca, $Ca_3[Al_6 Si_{10}O_{32}]\cdot 14H_2O$ (Coombs

et al., 1997). Both are calcium dominant and are characterised by **GIS** topology (see the chapter on 'Crystallography of **GIS**-type structure' in the Background information section of Coombs *et al.*, 1997). Nevertheless, garronite-Ca is notable for the disordered Si/Al distribution of the framework, and partial replacement of Ca by Na, resulting in a different space group with respect to gismondine-Ca. The **GIS** framework-type is also characteristic of alkali-dominant zeolites: fully ordered amicite, $K_4 Na_4[Al_8 Si_8 O_{32}]\cdot 10H_2O$, and (Si, Al) disordered gobbinsite, $Na_5[Al_5 Si_{11}O_{32}]\cdot 11H_2O$. It is worth adding that monoclinic Ba-dominant gismondine, $Ba_4[Al_8 Si_8 O_{32}]\cdot 12H_2O$, has been found only in anthropogenic material hence it is not approved by the Commission on New Minerals, Nomenclature and Classification of the International Mineralogical Association (IMA–CNMNC).

It has been 25 years since Coombs *et al.* (1997) published their guidelines for zeolite mineral species. The recent findings of garronite-Na, $Na_6[Al_6 Si_{10}O_{32}]\cdot 8.5H_2O$, and gismondine-Sr, $Sr_4[Al_8 Si_8 O_{32}]\cdot 9H_2O$, have revealed, however, the necessity of reviewing the data of minerals with **GIS** structure topology. This paper provides new data about gismondine-Sr from its second recorded occurrence at the Bellerberg volcano in Germany. Previously, it has been known only at the Halamish locality from the pyrometamorphic rocks of the Hatrurim Complex, Israel

(Skrzyńska *et al.*, 2023). Additionally, we provide data on barium-rich gismondine. Finally, we proposed revising the definition and classification for zeolites with **GIS** framework type.

Background information

Crystallography of the GIS-type structure

The **GIS**-type structure belongs to the group of doubly connected 4-membered ring chains. It is characterised by two (4- and 8-membered rings of tetrahedra) secondary building units (SBU) (Baerlocher *et al.*, 2007). The 4-membered rings are connected by sharing oxygen atoms and form a double crankshaft chain (Fig. 1a). The rings are alternatively oriented upwards and downwards, defining a T–O–T angle and resulting in a ~10 Å periodicity of the chains (Armbruster and Gunter, 2001). Thus, the T–O–T angle is determined by two adjacent rings in the double crankshaft chain pointing in opposite directions. In a gismondine structure-type, there are two systems of double crankshaft chains, which are perpendicular to each other and run parallel to the *a* and *b* axis, creating 8-membered ring channels (Fig. 1b). The ellipticity of the 8-membered aperture results from the T–O–T angle in the double crankshaft chain, which is perpendicular to the 8-membered rings window (Fig. 1; Skrzyńska *et al.*, 2023). The cage (*t-gsm*, pore descriptor $4^6 8^4$), which hosts extra-framework cations and water molecules, is formed at the intersection of the perpendicular double crankshaft chains. The type of extra-framework cations in these cages leads to modifications of the flexible zeolite framework (Skrzyńska *et al.*, 2023). The symmetry of the **GIS** structure-type varies from tetragonal to monoclinic (Hansen *et al.*, 1990; Håkansson *et al.*, 1990). The archetype symmetry (topological symmetry) of the **GIS** topology is $I4_1/amd$. This symmetry corresponds to that of the synthetic phase (called Na-P) – sodium high silica compound $(Na_4[Al_4Si_{12}O_{32}]\cdot 14H_2O;$

$a = 9.9989(4)$ Å; and $c = 10.0697(4)$ Å) (Baerlocher and Meier, 1972; Håkansson *et al.*, 1990, Supplementary Table S1). The topological symmetry is reduced to at least orthorhombic (*Fddd*) by the ordering of the cations at the framework T-sites. In turn, the ordered arrangement of extra-framework cations lowers the orthorhombic symmetry to monoclinic (Gottardi, 1979; Gottardi and Galli, 1985; Armbruster and Gunter, 2001).

Minerals with GIS structure type

Gismondine-Ca is the most common species among minerals with **GIS** topology. It is characterised by a monoclinic structure with (Si, Al) distribution fully ordered at T sites (Table 1). However, the symmetry can change to orthorhombic due to dehydration (van Reeuwijk, 1971; Vezzalini *et al.*, 1993; Wadoski-Romeijn and Armbruster, 2013). The *R*-value, defined as Si/(Si+Al+Fe), varies from 0.50 to 0.54 (Passaglia and Sheppard, 2001). The monovalent cations are present in negligible amounts (Vezzalini and Oberti, 1984). Ba-rich gismondine has only been found in weathered lead-smelting slags, therefore, it has not been approved as a new mineral species. Its crystals exhibited monoclinic symmetry and a slight amount of sodium and calcium were revealed in the chemical composition (Braithwaite *et al.*, 2001). Strontium impurities, however, were detected only as insignificant substitutions (Vezzalini and Oberti, 1984; Passaglia and Sheppard, 2001). Gismondine-Sr has been discovered recently in voids from the pyrometamorphic rock of the Hatrurim Complex in Israel (Skrzyńska *et al.*, 2023). Despite the ordered framework and Si/Al ratio equal to 1, its symmetry was found to be orthorhombic (Table 1) with channels that are elliptically deformed with respect to the monoclinic calcium variety (Skrzyńska *et al.*, 2023). Gismondine-Sr has a lower water molecule content and a significant substitution of monovalent cations (especially K), arranged randomly in the channels.
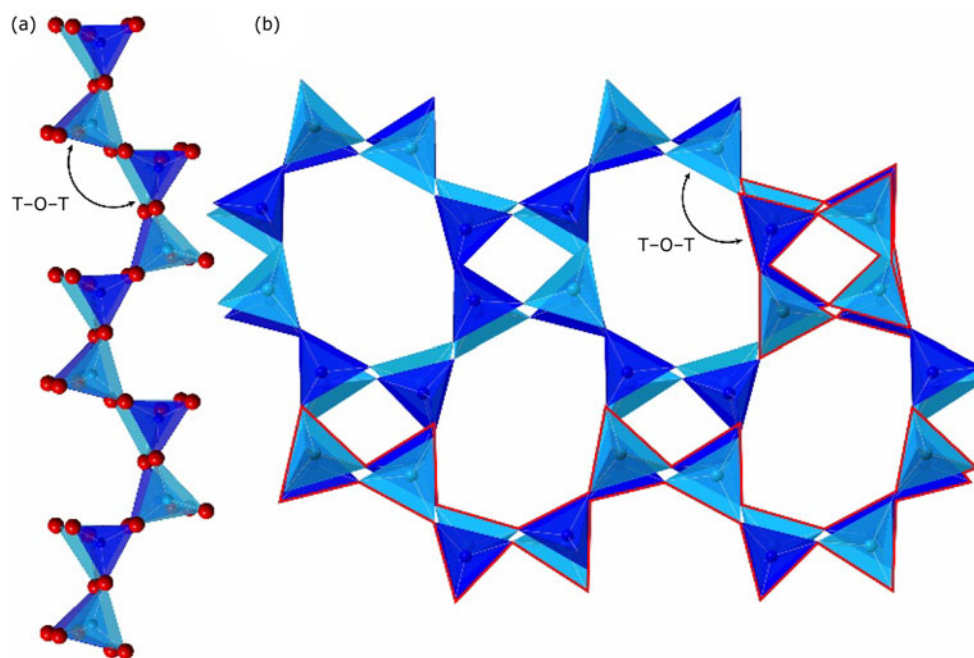

Figure 1. (a) Double crankshaft chain with marked T–O–T angle between upward and downward 4-membered rings; (b) framework of **GIS** structure-type with 8-membered ring channels. A red colour marks double the crankshaft chains, the first perpendicular to the picture plane and the second parallel to the picture plane (drawn with *CrystalMaker®* software).

Table 1. Zeolite minerals with **GIS** framework type.

Formula	$Ca_4[Al_8Si_8O_{32}]$ ·16H_2O	$Sr_4[Al_8Si_8O_{32}]$ ·9H_2O	$K_4Na_4[Al_8Si_8O_{32}]$ ·10H_2O	$Ba_4[Al_8Si_8O_{32}]$ ·12H_2O
Name	Gismondine-Ca	Gismondine-Sr	Amicite	'Gismondine-Ba'
Space group	$P2_1/c$	$B22_12$	$I2$	monoclinic
a (Å)	10.02	13.794	10.226	14.896
b (Å)	10.62	14.026	10.422	9.951
c (Å)	9.84	10.459	9.884	7.613
α (°)	90	90	90	90
β (°)	92.42	90	88.32	103.25
γ (°)	90	90	90	90
V (Å³)	1046.2	2023.43	1051.7	1098.42
$R = Si/(Si+Al+Fe)$	0.50–0.54	0.50–0.51	0.50	0.50–0.51
Si–Al distribution	ordered	ordered	ordered	ordered
Possible extra-framework cations in abundance order	Ca, Sr, Ba	Sr, K, Ca, Ba, Na	K, Na, Ca	Ba, Ca, Sr, K, Na
References	Fischer (1963)	Skrzyńska et al. (2023)	Alberti and Vezzalini (1979)	Braithwaite et al. (2001)

Formula	$Ca_3[Al_6Si_{10}O_{32}]$ ·14H_2O	$Na_6[Al_6Si_{10}O_{32}]$ ·8.5H_2O	$(Na_{1.99}K_{0.27})_{\Sigma2.26}Ca_{1.61}$ $[Al_{5.31}Si_{10.64}O_{32}]$ ·14.3H_2O	$Na_5[Al_5Si_{11}O_{32}]$ ·11H_2O
Name	Garronite-Ca	Garronite-Na	Si-rich garronite-Na	Gobbinsite
Space group	$I\bar{4}m2$ or $I2/a$	$I2$	$I2$	$Pmn2_1$
a (Å)	9.927 or 9.880	9.990	9.983	10.104
b (Å)	9.927 or 10.280	10.032	10.089	9.782
c (Å)	10.303 or 9.876	10.036	10.070	10.152
α (°)	90	90	90	90
β (°)	90 or 90.114	90.11	90.223	90
γ (°)	90	90	90	90
V (Å³)	1015.3	1005.8	1014	1003.4
$R = Si/(Si+Al+Fe)$	0.60–0.65	0.60–0.67	0.60–0.64	
Si–Al distribution	disordered–partially ordered	disordered–partially ordered	disordered	
Possible extra-framework cations in abundance order	Ca, Na, K	Na, K	Na, Ca, K, Mg	
References	Artioli (1992); Artioli and Marchi (1999)	Grice et al. (2016)	Hirahata et al. (2022)	Gatta et al. (2010)

The **GIS** zeolite with Si/Al ratio equal to 1 containing K and Na as dominant cations is amicite (Alberti and Vezzalini, 1979). This is a rare zeolite known only from a few localities (Pekov and Podlesnyi, 2004; Calvo et al., 2013; Jackson et al., 2019). Similar to gismondine minerals, the R-value is ∼0.5. The structure is also monoclinic and perfectly ordered (framework and extra-framework cations, Table 1). The positions of Na and K sites in amicite correspond to the Ca and H_2O sites in gismondine, respectively (Alberti and Vezzalini, 1979). Consequently, amicite has a lower hydration level than monoclinic gismondine-Ca. In addition, amicite shows no significant variation in the chemical composition, and Ca is present in minor amounts (Passaglia and Sheppard, 2001; Pekov and Podlesnyi, 2004). Interestingly, amicite can be completely dehydrated retaining the monoclinic symmetry (Vezzalini et al., 1999; Armbruster and Gunter, 2001).

Other zeolites with **GIS** framework-type display a lower Si/Al ratio with respect to gismondine and amicite (Table 1). A disordered counterpart of gismondine-Ca is garronite-Ca with an R-value of 0.60–0.65 (Walker, 1962; Gottardi and Galli, 1985). The symmetry of garronite-Ca is usually described as tetragonal in space group $I\bar{4}m2$, which is lowered from the archetype structure due to possible partial ordering of the T sites or cations/water molecules order in the zeolitic cavities (Artioli, 1992; Artioli and Marchi, 1999; Armbruster and Gunter, 2001; Passaglia and Sheppard, 2001). However, orthorhombic and monoclinic symmetry have also been reported (Artioli and Marchi, 1999;

Armbruster and Gunter, 2001). It has also been noticed that the symmetry of the partly dehydrated phase decreased to $I2/a$ and $P4_12_12$ (Passaglia and Sheppard, 2001). Contrary to gismondine-Ca, samples of garronite-Ca contain a relevant amount of K and especially as Na substitutions. Passaglia and Sheppard (2001) indicated that the compositional gap between gismondine and garronite relates to Si/Al ratio, not boundaries in extra-framework content.

Garronite-Na, the Na end-member of the garronite series, was first described by Grice et al. (2016). It differs from the Ca species because of the lower hydration degree and the monoclinic symmetry (Table 1), which can be explained by the partial ordering of the framework cations, as demonstrated by the tetrahedral bond distances. Grice et al. (2016) found that the naturally occurring garronite-Na is the intermediate phase between two synthetic phases, low-Si garronite $Na_8(Al_8Si_8O_{32})$·15H_2O (Albert et al., 1998) and high-Si garronite $Na_4(Al_4Si_{12}O_{32})$·14H_2O (Håkansson et al., 1990) (Grice et al., 2016; Supplementary Table S1). Additionally, it was emphasised that the structure of garronite-Na is isostructural to gobbinsite, and the transformation matrix from garronite-Na to gobbinsite is (010/001/100) (Grice et al., 2016).

Gobbinsite was first described by Nawaz and Malone (1982). The structure was obtained by powder X-ray diffraction data and subsequent Rietveld refinement (Nawaz and Malone, 1982; Artioli and Foy, 1994). Regardless of the suggestion above of Grice et al. (2016), Gottardi and Galli (1985) envisaged that gobbinsite is the sodium equivalent of garronite-Ca and similar to the

synthetic compound Na-P1. It should be highlighted that the *R*-value of gobbinsite corresponds to garronite-Ca. Sodium is consistently a dominant cation in the chemical analyses. However, high substitutions of Ca are regularly present, whereas Mg and K were only detected in minerals from one locality (Passaglia and Sheppard, 2001). In 2010 the crystal structure of gobbinsite was successfully refined from single-crystal X-ray diffraction (SCXRD, Gatta *et al.*, 2010). The refinement revealed the orthorhombic space group *Pmnb* (Table 1). The framework exhibits high disorder, while the calcium and sodium cations occupy two separated sites in the cage. According to Gatta *et al.* (2010) the gobbinsite structure is consistent with the synthetic zeolite $Na_4(Al_4Si_{12}O_{32})\cdot14H_2O$ reported by Hansen *et al.* (1990; Table S1). Furthermore, the authors proposed a general formula for gobbinsite: $(Na,K,0.5Ca)_{5+x}[Al_{5+x}Si_{11-x}O_{32}]\cdot12H_2O$ (Gatta *et al.*, 2010).

Sample description and methods of investigation

Bellerberg volcano, Germany

The Bellerberg volcano belongs to the Quaternary volcanics in the Eastern Eifel region, Rhineland-Palatinate, Germany (Hentschel, 1987; Mihajlovic *et al.*, 2004). It is characterised by different thermally metamorphosed xenoliths embedded within the basaltic lava of tephrite–leucite composition (Hentschel, 1987; Mihajlovic *et al.*, 2004). The xenoliths have unique mineral assemblages crystallised as a result of high-temperature metamorphism and a variety of numerous secondary phases formed at low-temperature conditions and the weathering processes (Mihajlovic *et al.*, 2004; Juroszek *et al.*, 2022). The Bellerberg volcano region is famous for several new mineral findings, including the Sr-rich zeolite bellbergite (Rudinger *et al.*, 1993; Irran *et al.*, 1997; Kraus *et al.*, 1999; Lengauer *et al.*, 2009; Chukanov *et al.*, 2015).

Gismondine-Sr was detected in white–grey xenolith samples collected in the 'Seekante' district, which is the eastern part of the southern lava flow of the Bellerberg volcano. The primary mineral association of the analysed sample is composed of high-temperature phases such as wollastonite, åkermanite, gehlenite, larnite, combeite, bredigite, fluorapatite and feldspathoids, mostly

nepheline and leucite. The abundant accessory assemblages are represented by brownmillerite, shulamitite, perovskite, magnesioferrite, hematite, baghdadite, some rare Ba-minerals such as fresnoite, bennesherite, noonkanbahite, batiferrite and alforsite, as well as Cl- and OH-apatite minerals. Gismondine-Sr was found in the cavities filled with secondary minerals such as flörkeite, strätlingite/vertumnite, baryte, periclase, afwillite, ettringite, and minerals of the tobermorite supergroup (Fig. 2a). The crystals of gismondine-Sr form pseudotetragonal bipyramids and are characterised by distinct cleavage in [101] direction (Fig. 2b).

Hatrurim Complex, Israel

The Hatrurim Complex is a pyrometamorphic complex consisting of several individual outcrops formed by resistant rock nested in a weathered calcium–hydrosilicate mass. The genesis aspect of the rock formations is uncertain. Mud volcanism activity and burning organic matter in bituminous chalk are considered possible sources of heat (Gross, 1977; Sokol *et al.*, 2008; Geller *et al.*, 2012; Novikov *et al.*, 2013; Galuskina *et al.*, 2014). Indubitably, the conditions of rock formation were high temperature and low pressure, comparable to the Bellerberg volcano conditions. Hornfels-like rocks, containing wollastonite, fluorapatite, minerals of gehlenite–alumoåkermanite series, and Ti-bearing andradite prevail among various rock types of the Hatrurim Complex. They host coarse-grained rocks called paralava despite the absence of glass (Vapnik *et al.*, 2007; Sharygin *et al.*, 2008; Krzątała *et al.*, 2020). Accessory mineralisation of paralava containing celsian, barioferrite, and Si-rich V-bearing zadovite forms in clusters enriched in Ba, V, P, and rarely U (Krzątała *et al.*, 2020, 2022). The high-temperature rocks contain voids filled by low-temperature mineralisation, in which Ba-rich crystals of the gismondine series have been found. It occurs adjacent to the Ba-rich paralava minerals (Fig. 3a,b). Barium-rich gismondine forms tiny intergrown crystals and is characterised by variable content of Ba, Sr and Ca. In addition to minerals of the gismondine series, flörkeite (**PHI** type structure), the most abundant zeolite in the pyrometamorphic rock of the Hatrurim Complex, (Skrzyńska *et al.*, 2022) has been recorded. Another type of
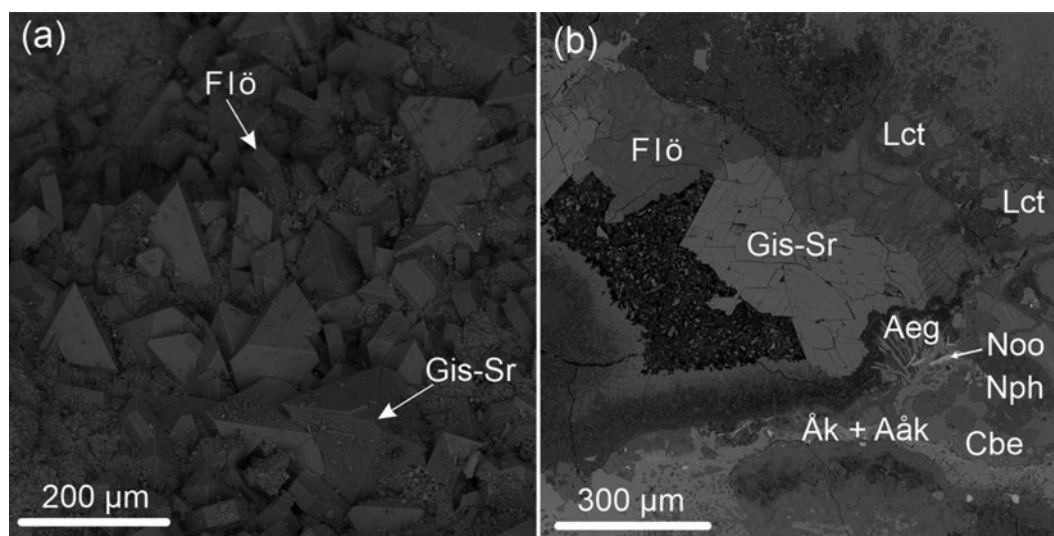

Figure 2. BSE images. (a) Cavity in xenolith from the Bellerberg volcano filled by gismondine-Sr and flörkeite crystals on tobermorite; (b) gismondine-Sr in the xenolith association. Symbols from Warr (2021): Aeg – aegirine; Åk – åkermanite; Aåk – alumo åkermanite; Cbe – combeite; Gis-Sr – gismondine-Sr; Lct – leucite; Nph – nepheline; and Noo – noonkanbahite.
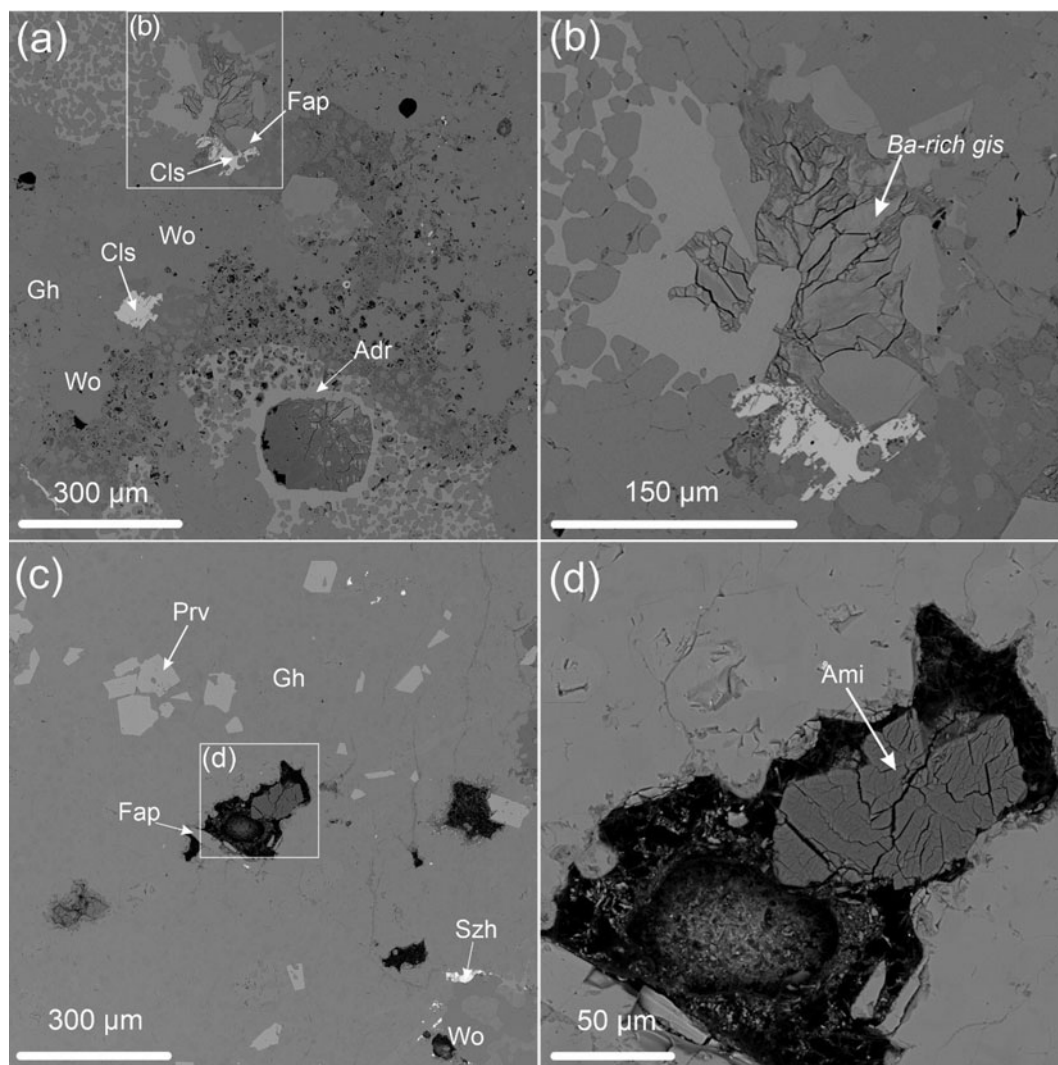
Figure 3. BSE images of paralava from the Hatrurim Complex, Israel. (a) General view of paralava with voids filled by Ba-rich zeolite, the frame indicates the magnified fragment shown in: (b) crystals of Ba-rich gismondine. (c) General view of paralava with amygdaloidal voids filled by amicite, the frame outlines the magnified fragment in: (d) crystals of amicite in amygdaloidal voids. Symbols from Warr (2021): Adr – andradite, Ami – amicite, Cls – celsian, Fap – fluorapatite, Gh – gehlenite, Ba-rich gis – Ba-rich gismondine, Prv – perovskite, Szh – shenzhuangite, Wol – wollastonite.

paralava from the Hatrurim Complex is porous and contains mainly gehlenite, wollastonite, kalsilite, fluorapatite, perovskite and chromite (Fig. 3c); the zeolite amicite has also been found forming pseudo-octahedral crystals (Fig. 3d). Moreover, minerals of ettringite–thaumasite series and flörkeite have been revealed in the low-temperature mineralisation.

Chemical composition

The preliminary chemical composition and crystal habit of the zeolites and mineral association have been investigated using a Phenom XL scanning electron microscope equipped with an energy-dispersive X-Ray spectrometer and back-scattered electron (BSE) detectors (Faculty of Natural Science, University of Silesia, Poland). A Cameca SX100 microprobe analyser was used to obtain quantitative chemical analyses. The gismondine-Sr and amicite were characterised at the Faculty of Geology, University of Warsaw, Poland. The results were obtained at 15 keV and 5 nA. The beam size was 15 μm. The following standards and lines were applied: Na$K\alpha$ (albite); Si$K\alpha$ (diopside); Al$K\alpha$ (orthoclase); $KK\alpha$ (orthoclase); Ca$K\alpha$ (diopside); Fe$K\alpha$ Fe$_2$O$_3$; Sr$L\alpha$ (celestine); and Ba$L\alpha$ (baryte). Ba-rich gismondine was studied at the Polish Geological Institute, National Research Institute, Warsaw, Poland. The analyses were carried out at 15 keV and 20 nA with a 5 μm beam size. The following standards and lines were used: Na$K\alpha$ (NaCl); Si$K\alpha$ (wollastonite); Al$K\alpha$ (orthoclase); $KK\alpha$ (orthoclase); Ca$K\alpha$ (wollastonite); Fe$K\alpha$ (pentlandite); Sr$L\alpha$ (celestine); and Ba$L\alpha$ (BaSO$_4$).

Raman spectroscopy

Raman spectroscopy analyses were conducted on a WITec alpha 300R confocal Raman microscope (Faculty of Natural Science, University of Silesia, Poland) with a CCD camera operating at –61°C. The spectra were collected with a 488 nm laser. A silicon plate (520.7 cm^{-1}) was used to calibrate the monochromator with a 600 mm^{-1} grating. Integration time and accumulation were as follows: 15 accumulations with 10 s integration for gismondine-Sr; 30 accumulations with 7 s integration for Ba-rich gismondine; 25 accumulations and 5 s integration for amicite. The spectra

deconvolution was performed using the *GRAMS* package (Thermo Scientific™). For the peak-fitting process, the Gauss–Lorentz function with the minimum number of component bands was used.

Single-crystal X-ray diffraction

Single-crystal X-ray diffraction experiments were conducted using a Rigaku Synergy-S diffractometer equipped with a dual microfocused source and a Hypix detector (University of Bern, Switzerland). Due to the tiny sizes and brittleness of the zeolite crystals, data could only be obtained successfully on a sample of gismondine-Sr. The data were collected using Cu$K\alpha$ radiation ($\lambda = 1.540598$ Å). Data reduction and absorption correction procedures were performed by Rigaku *CrysalisPro 40.29a*. The structure solution and refinement procedure were performed in the *WinGX* package (Farrugia, 1999) using *SHELXS* (Sheldrick, 2008) and *SHELXL* (Sheldrick, 2015), respectively.

Results

Chemical composition

The results of the chemical microanalyses are in Table 2. Water content has been estimated based on the difference to 100%. The following empirical crystal chemical formula has been calculated based on the 16 framework tetrahedral sites and 32 oxygen atoms:

Gismondine-Sr: $(Sr_{1.74}Ca_{1.05}K_{1.56}Na_{0.49}Ba_{0.09})_{\Sigma 4.93}[Al_{7.98}Si_{8.06}O_{32}]\cdot 9.62H_2O$;
Ba-rich gismondine: $(Ba_{1.27}Sr_{1.26}K_{1.25}Ca_{0.73}Na_{0.36})_{\Sigma 4.87}[Al_{7.78}Fe_{0.05}Si_{8.09}O_{32}]$
   $\cdot 8.40H_2O$;
Amicite: $(K_{3.73}Na_{3.29}Ca_{0.31})_{\Sigma 7.33}[Al_{8.03}Fe_{0.02}Si_{8.06}O_{32}]\cdot 4.81H_2O$

Compared to the type locality, the gismondine-Sr crystals from Germany stand out by having significantly higher potassium content. The empirical formula of Ba-rich zeolite revealed relevant Sr- and K- substitutions in the cages. Additionally, both gismondine-Sr, Ba-rich gismondine and amicite display a significant Ca content. In addition, amicite from the Hatrurim Complex exhibits lower water content than the end-member formula (Alberti and Vezzalini, 1979).

Raman spectroscopy

The Raman spectra in Fig. 4 collected on gismondine-Sr crystals (a), Ba-rich gismondine (b), and amicite (c) are typical of the **GIS** structure-type. Generally, bands in zeolite spectra can be divided into external- and intra-tetrahedral bands. However, it is not possible to separate them precisely. The external-tetrahedral bands come from the links between TO_4. Thus, they depend on the framework type (Auerbach *et al.*, 2003; Čejka *et al.*, 2007; Chester and Derouane, 2009). The intra-tetrahedral bands are structure insensitive. Hence, they are correlated to tetrahedral modes. All spectra exhibit three framework vibrations regions: 300–500 cm^{-1}, 650–730 cm^{-1} and 950–1100 cm^{-1}, and vibrations of water molecules (Table 3). In the first framework vibrations region, the strongest band at ∼460 cm^{-1}, corresponds to breathing modes of 4-membered rings originating from the symmetric bending O–T–O vibrations of the tetrahedron (Mozgawa, 2001; Borodina *et al.*, 2022). The bands between 374–407 cm^{-1} can be assigned to the 8-membered rings deformation vibration (Borodina *et al.*, 2022; Skrzyńska *et al.*, 2023). Both 460 cm^{-1} and 374–407 cm^{-1} regions experience variations in intensity depending on the crystal orientation in terms of laser beam polarisation, and they are classified as external-tetrahedral bands (Skrzyńska *et al.*, 2023). The bands around 700 cm^{-1} are related to the asymmetric O–T–O bending vibrations of the tetrahedrons. However, symmetric stretching vibrations of bridging oxygen atoms between tetrahedra may also appear. Symmetric and

Table 2. Chemical composition of gismondine-Sr from Germany, Ba-rich gismondine and amicite from the Hatrurim Complex.*

Wt.%	Gismondine-Sr			Ba-rich gismondine			Amicite		
	mean $n = 11$	S.D.	range	mean $n = 4$	S.D.	range	mean $n = 16$	S.D.	range
SiO_2	34.44	0.97	33.47–34.62	32.98	0.30	32.81–33.42	37.94	0.70	36.47–39.25
Al_2O_3	28.95	0.71	27.94–29.19	26.91	0.23	26.67–27.19	32.05	0.60	30.86–32.95
Fe_2O_3	n.d.	n.d.	n.d.	0.27	0.10	0.20–0.41	0.11	0.07	0.00–0.21
CaO	4.17	0.17	3.84–4.23	2.79	0.15	2.68–3.01	1.34	0.62	0.40–2.99
SrO	12.83	0.55	12.16–12.92	8.84	0.15	8.67–9.02	n.d.	n.d.	n.d.
BaO	0.96	0.41	0.63–1.18	13.20	0.76	12.12–13.76	n.d.	n.d.	n.d.
Na_2O	1.09	0.31	0.58–1.27	0.75	0.11	0.62–0.87	7.99	0.47	7.29–8.68
K_2O	5.23	0.52	4.78–5.43	4.01	0.03	3.97–4.04	13.75	0.53	12.71–14.64
H_2O	12.33			10.27			6.79		
Total	100.00			100.00			100.00		
Atomic proportions based on 16 T sites and 32 oxygen atoms									
Si	8.06			8.09			8.06		
Al	7.98			7.78			8.03		
Fe^{3+}				0.05			0.02		
T	16.00			16.00			16.00		
Sr	1.74			1.26			–		
Ca	1.05			0.73			0.31		
Ba	0.09			1.27			–		
K	1.56			1.25			3.73		
Na	0.49			0.36			3.29		
Extra-framework	4.93			4.87			7.33		
H_2O	9.62			8.40			4.81		
R	0.50			0.51			0.50		
E %	2.17			−3.71			5.32		

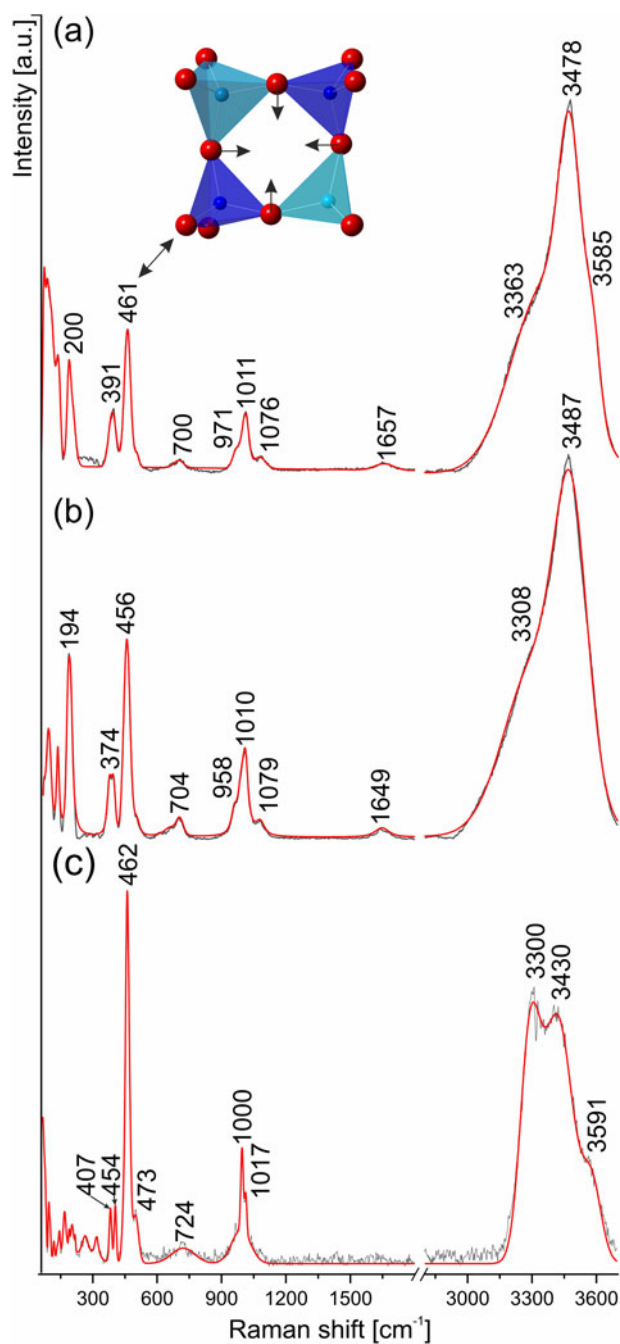*S.D. – standard deviation; *n* – number of analyses; n.d. – not detected.

Figure 4. Raman spectra of (a) gismondine-Sr with corresponding vibrations of a 4-membered ring; (b) Ba-rich gismondine; and (c) amicite.

asymmetric stretching T–O vibrations occur between 958–1079 cm^{-1}. The bands at ~1650 cm^{-1} and in the range 3363–3585 cm^{-1} correspond to the bending and stretching vibrations of the water molecules, respectively.

SCXRD data and structure description

The crystal structure of gismondine-Sr from the Bellerberg volcano was refined in space group $B22_12$ to $R = 0.0440$ with the following unit cell parameters: $a = 13.9859(2)$ Å, $b = 10.4683(1)$ Å, $c = 13.7542(2)$ Å and $V = 2013.733$ Å^3 (Table 4). By analogy with the structure from the type locality, the non-standard setting of the unit cell was chosen for similarity with partially dehydrated gismondine-Ca (van Reeuwijk, 1971; Vezzalini *et al.*, 1993; Wadoski-Romeijn and Armbruster, 2013). The atoms of the framework were refined first. The average bond distances of tetrahedra indicated the ordered distribution of Al and Si at the T sites (<Si–O> = 1.61 Å and <Al–O> = 1.73 Å, Supplementary Table S2). After the refinement of the framework atoms, the extra-framework positions were inserted into the model. The two strongest peaks in the electron density maps were refined with the Sr scattering curve (C1 and C2 sites). Then, residual electron density, at ~0.57–0.89 Å distance from Sr cations, was refined with Ca scattering factors (C1A and C1A). Nevertheless, additional electron density was observed near the C2 position. This electron density was modelled as a split potassium site (C2B and C2C). The remaining electron density was assigned to partially occupied water molecules sites (W1, W1A, W2, W3, CW3 and W4). Due to the high-level of disorder and low occupancy of extra-framework sites, the average chemical compositions from microprobe analyses were availed to improve the refinement. Therefore, the C1 position was finally refined with a mixed scattering factor (0.29 Sr and 0.110 K), and the CW3 site was assigned to sodium atoms (Table 5). Due to excessively short distances, not all of the extra-framework positions and water sites can be simultaneously occupied (Table 6). The crystallographic information file has been deposited as Supplementary material (see below).

The structure of gismondine-Sr from Germany does not differ significantly from the Israeli (holotype) specimen. The double crankshaft chains and the 8-membered rings are parallel to [101] and [10$\bar{1}$] (Fig. 5a). The structure of gismondine-Sr contains two types of non-equivalent symmetry cages, which host randomly distributed extra-framework cations and water molecules (Fig. 5). It is worth highlighting that the cages are topologically the same. They differ only in the extra-framework content. The *t-gsm 1* cage (Fig. 5, purple colour) contains two symmetry equivalent partially occupied sites by calcium (C1A) and strontium-potassium (C1). The potassium content *t-gsm 2* cage

Table. 3. Assignment of Raman bands for **GIS** zeolites.

Band assignment	This work (cm^{-1})			Tsai *et al.* (2021) (cm^{-1})		
	gismondine-Sr	Ba-rich gismondine	amicite	gismondine-Ca	garronite-Ca	gobbinsite
Lattice vibrations	200	194				
8–membered rings deformation	391	374	454	403	421	391
Symmetric bending O–T–O*	**461**	**456**	**462**	**463**	**475**	**485**
Asymmetric O–T–O bending	700	704	724			
Symmetric and asymmetric stretching T–O	971, 1011, 1076	958,1010, 1079	1000, 1017			
Bending of H$_2$O	1657	1649				
Stretching of H$_2$O	3363, 3478, 3585	3308, 3487	3300, 3430, 3591			

*The main bands are indicated in bold.

Table 4. Crystal data and refined parameters of gismondine-Sr.

Crystal data	
Refined chemical formula	$Sr_{2.44}Ca_{0.87}K_{0.91}Na_{0.48}[Al_8Si_8O_{32}]\cdot 8.7H_2O$
Crystal system	Orthorhombic
Space group	$B22_12$
Unit cell dimensions (Å)	
a	13.9859(2)
b	10.46830(10)
c	13.7542(2)
Volume (Å³)	2013.73(5)
Data collection	
Diffractometer	Rigaku synergy-S
Radiation wavelength (Å)	1.54184
Temperature (K)	293(2)
Crystal dimensions (mm)	0.04 × 0.03 × 0.03
F(000)	1364
Max. 2θ (°)	153.39
Index ranges	$-13 \leq h \leq 17$
	$-13 \leq k \leq 12$
	$-17 \leq l \leq 16$
R_{int}	0.0418
$R\sigma$	0.0317
Structure refinement	
Reflections collected	8046
Independent reflections	2077
Observed data ($I > 2\sigma(I)$)	2012
No. of refined parameters	181
R_1, wr_2^* ($I > 2\sigma(I)$)	0.0451 ($wr = 0.1215$)
R_1, wr_2 (for all)	0.0463 ($wr = 0.1223$)
Goof	1.074
$\Delta\rho_{min}$ ($e^- / Å^{-3}$)	−0.52
$\Delta\rho_{max}$ ($e^- / Å^{-3}$)	0.78
*Weighting scheme	$W = 1/[\sigma^2(F_o^2) + (0.0676P)^2 + 13.13P]$ where $P = (F_o^2 + 2F_c^2)/3$

Table 5. Atom coordinates (*x,y,z*), equivalent isotropic displacement parameters (U_{eq}/U_{iso}*, Å²) and site occupancies.

| Site	Atom	Occupancy	x	y	z	U_{eq}/U_{iso}*
Si1	Si	1	0	0	0.43129(16)	0.0110(5)
Si2	Si	1	−0.23605(11)	0.28208(15)	0.16611(11)	0.0087(4)
Si3	Si	1	0	0	0.09875(16)	0.0115(5)
Al1	Al	1	−0.07729(18)	¼	0	0.0117(5)
Al2	Al	1	0.10610(17)	¼	½	0.0116(5)
Al3	Al	1	−0.15801(12)	0.03346(16)	0.26592(13)	0.0104(4)
O1	O	1	−0.1435(4)	0.2989(5)	0.0996(4)	0.0286(12)
O2	O	1	0.0959(4)	0.0098(5)	0.1620(4)	0.0268(11)
O3	O	1	−0.0874(4)	0.0514(5)	0.3671(5)	0.0321(13)
O4	O	1	−0.3280(4)	0.2372(5)	0.1061(4)	0.0285(12)
O5	O	1	−0.2183(4)	0.1774(5)	0.2505(4)	0.0286(13)
O6	O	1	−0.2444(4)	−0.0839(5)	0.2788(4)	0.0245(11)
O7	O	1	0.0010(4)	−0.1259(6)	0.0310(4)	0.0306(12)
O8	O	1	0.0352(4)	0.1139(6)	0.5015(4)	0.0298(12)
C1	Sr	0.352(9)	−0.17411(16)	−0.2147(2)	0.10303(17)	0.0321(8)
C11	K	0.048(9)	−0.17411(16)	−0.2147(2)	0.10303(17)	0.0321(8)
C1A	Ca	0.08	−0.217(4)	−0.197(4)	0.067(4)	0.077(11)*
C2	Sr	0.258(7)	−0.4003(2)	0.0318(3)	0.1808(3)	0.0297(16)
C2A	Ca	0.135(12)	−0.3876(17)	−0.038(3)	0.1465(18)	0.068(8)*
C2B	K	0.089(12)	−0.380(2)	0.071(3)	0.236(3)	0.051(10)*
C2C	K	0.09	−0.430(3)	0.043(3)	0.227(3)	0.064(8)*
C2W	O	0.18(3)	−0.440(4)	−0.129(5)	0.176(4)	0.067(19)*
W1	O	0.67(3)	−0.3960(11)	0.0574(15)	0.3685(11)	0.071(5)*
W1A	O	0.18(4)	−½	0	0.346(5)	0.07(2)*
W2	O	0.33(2)	−0.4871(14)	0.226(2)	0.2507(13)	0.041(7)*
W3	O	0.45(3)	−0.3705(15)	−0.183(2)	0.1040(16)	0.065(7)*
CW3	Na	0.12	−0.354(3)	−0.225(4)	0.048(3)	0.059(9)*
W4	O	0.45(3)	−0.253(2)	−0.034(3)	0.020(2)	0.107(13)*

(Fig. 5, green colour) differs from *t-gsm 1*. Two additional potassium positions (C2B and C2C) are found in *t-gsm 2*, whereby the C2 position is occupied only by strontium (Fig. 5). The two types of cages occur alternatively in the structure (Fig. 5a), producing an overlapping picture along the channel (Fig. 5b,c).

Discussion

Orthorhombic gismondine-Sr differs significantly from monoclinic gismondine-Ca. They vary not only in symmetry but also in water content — gismondine-Sr has only half the water content of the calcium species. Additionally, the monovalent cations have not been detected in the monoclinic gismondine-Ca in contrast to gismondine-Sr (Vezzalini and Oberti, 1984). These chemical changes lead to the elliptical deformation of the 8-membered rings window in gismondine-Sr (Skrzyńska *et al.*, 2023). Nevertheless, according to the guidelines for nomenclature of zeolites (Coombs *et al.*, 1997) the Sr-dominant zeolite with **GIS** framework type is only classified as a new end-member mineral in the gismondine series (Coombs *et al.*, 1997). Present data on Ba-rich gismondine indicate that the next potential new member of that series is gismondine-Ba. Significant replacement by Ca^{2+} in gismondine-Sr and by Sr^{2+} and Ca^{2+} in Ba-rich gismondine imply the following $D^{2+} \rightarrow D^{2+}$ mechanism of substitution (Fig. 6; Table 2). On the other hand, the high K content in gismondine-Sr and Ba-rich gismondine indicates a possible solid solution between the gismondine series and amicite, $K_2Na_2[Al_4Si_4O_{16}]\cdot 5H_2O$ (Fig. 6; Table 2). This is corroborated by the detected Ca substitution in amicite. In addition, the chemical analyses of some crystals of gismondine-Sr from the Bellerberg volcano exhibit the dominance of monovalent cations (i.e. K) in atomic proportions. In both the amicite and gismondine series the *R*-value is ∼0.5, which implies the second substitution $D^{2+} \rightarrow 2M^+$. Furthermore, the presence of the K ions explains the lower water content in gismondine-Sr and amicite. As was noted by Bauer and Baur (1998), K-exchanged gismondine featured a lower hydration level, probably because of the occupation of the available water sites by potassium, which has nearly the same interatomic distances to framework oxygen atoms (Bauer and Baur, 1998). This leads to the substitution scheme $H_2O + D^{2+} \rightarrow 2K^+$. According to the present results, amicite should be regarded as an alkali end-member of the gismondine series. Moreover, amicite and gismondine minerals are characterised by a prominent Raman band at about 460 cm^{-1}. The slight displacement of the main band in Ba-rich gismondine may result from the presence of a heavier cation. Despite framework deformation in gismondine-Sr, the spectra of gismondine-Sr and gismondine-Ca are similar (Table 3), which corroborates the origin of the band at 460 cm^{-1} from the symmetric-bending O–T–O vibrations of the Al/Si ordered 4-membered rings (Skrzyńska *et. al.*, 2023). In conclusion, amicite, gismondine-Ca and gismondine-Sr belong to one series, for which the Si/Al ratio = 1 and the main Raman band around 460 cm^{-1} is distinctive.

The next mineral series within the **GIS** topology is the garronite series, which is characterised by a disordered framework and a higher *R* (> 0.6) value than the gismondine series. This difference may trigger the displacement of the main band to a higher frequency (Table 3). The garronite series includes the recently described garronite-Na. Albeit, a distinction between gobbinsite and garronite-Na is questionable. Their distinguishing features are slightly different hydration degrees, as well as Si/Al ratio resulting in different Na content (Fig. 7, 8; Table 1). The substitution mechanism from garronite-Na to gobbinsite can be

Table 6. Interatomic distances of the extra-framework cations in the gismondine-Sr structure.

C1–C1A	0.80(6)	C2–C2C	0.77(5)	C2B–C2C	0.78(4)	C2W–W3	1.50(5)	W2–C2W	1.76(6)
C1–W4	2.47(3)	C2–C2A	0.89(3)	C2B–W1	1.84(4)	C2W–W2	1.76(6)	W2–C2A	2.99(3)
C1–O2	2.541(6)	C2–C2B	0.91(4)	C2B–W2	2.22(4)	C2W–C2C	2.14(6)	W2–C2C	3.06(4)
C1–C1A	2.59(5)	C2–C2W	1.78(5)	C2B–W1A	2.38(5)	C2W–CW3	2.36(7)	W2–C1	3.087(19)
C1–W1	2.609(16)	C2–C2W	2.45(5)	C2B–C2W	2.41(6)	C2W–C2	2.45(5)	W2–C11	3.087(19)
C1–CW3	2.63(4)	C2–W3	2.52(2)	C2B–C2W	2.72(6)	C2W–C2B	2.72(6)	W2–C2	3.26(2)
C1–O5	2.757(5)	C2–W2	2.55(2)	C2B–C2C	2.91(6)	C2W–C2A	3.01(6)		
C1–W3	2.77(2)	C2–C2C	2.57(4)					W3–CW3	0.92(4)
C1–C11	2.929(5)	C2–W1	2.596(15)	C2C–C2W	1.94(7)	W1–W1A	1.60(2)	W3–CW3	2.31(5)
C1–C1	2.929(5)	C2–W1A	2.69(6)	C2C–W1A	1.96(7)	W1–C11	2.609(16)	CW3–CW3	1.41(9)
		C2–O8	2.763(7)	C2C–W1	2.01(5)	W1–C1	2.609(16)	CW3–W3	2.31(5)
C1A–W4	1.90(6)			C2C–W2	2.09(4)	W1–C2C	3.29(5)	CW3–W4	2.48(5)
C1A–CW3	1.95(7)	C2A–C2W	1.27(6)	C2C–C2W	2.14(6)	W1A–W1	1.60(2)	CW3–C1A	2.61(7)
C1A–C1A	2.16(9)	C2A–C2C	1.52(5)	C2C–C2C	2.14(8)	W1A–C2C	1.96(7)	CW3–O3	2.74(4)
C1A–W3	2.21(5)	C2A–W3	1.64(4)	C2C–C2	2.57(4)	W1A–C2B	2.38(5)	CW3–O8	2.86(4)
C1A–C11	2.59(5)	C2A–C2B	1.68(5)	C2C–C2A	2.77(5)	W1A–C2	2.69(6)		
C1A–C1	2.59(5)	C2A–CW3	2.43(5)	C2C–C2B	2.91(6)			W4–C1A	3.10(5)
C1A–CW3	2.61(7)	C2A–W4	2.56(4)					W4–C11	3.32(3)
C1A–O2	2.90(5)	C2A–O8	2.77(2)						
C1A–O5	2.97(5)	C2A–C2C	2.77(5)						
C1A–C2A	3.10(6)	C2A–O8	2.98(3)						
		C2A–W2	2.99(3)						
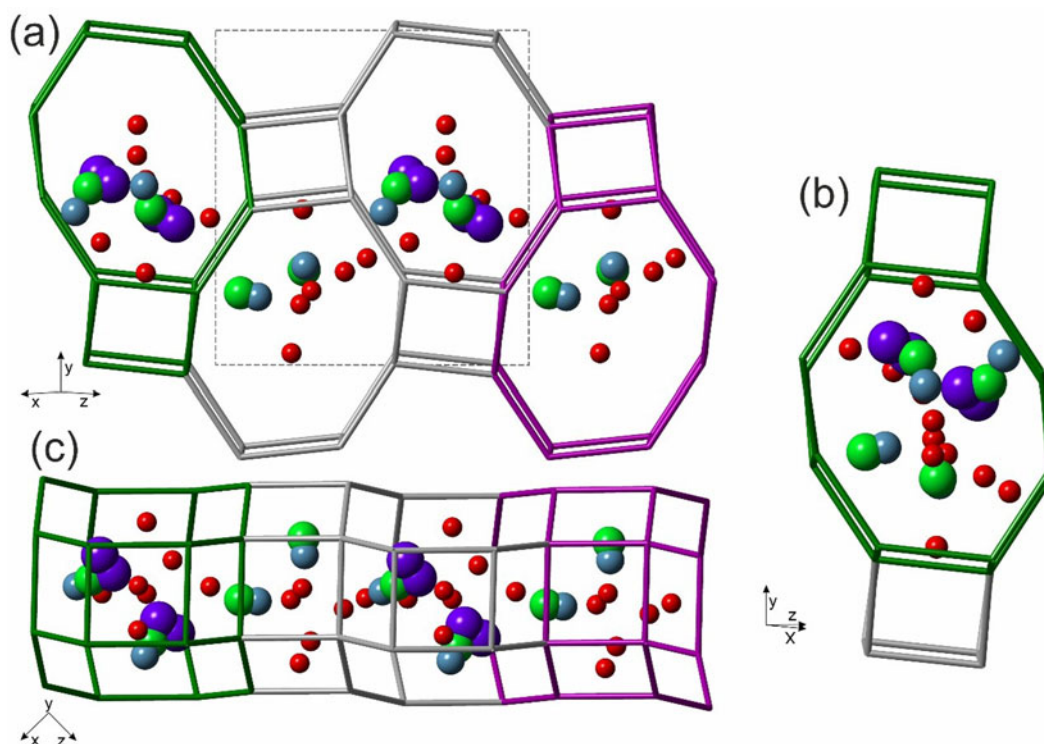
Figure 5. Framework of gismondine-Sr. (a) Two types of cages filled by distinct extra-framework cations and water molecules, view along [101]; (b) structure presented in (a) rotated by 90° around the *b* axis; (c) view along [010]; purple colour marks *t-gsm 1*, green colour marks *t-gsm 2*. Key: green spheres – strontium cations; blue spheres – calcium cations; purple spheres – potassium cations; red spheres – water molecules; and the dotted grey line – unit cell.

represented as follows: $2M^+ + Al^{3+} \rightarrow M^+ + Si^{4+}$. The extra-framework cations content influences the channel diameters, leading to higher ellipticity along [100] in the gobbinsite structure with respect to garronite-Na (Fig. 8; Grice *et al.*, 2016). Recently, Hirahata *et al.* (2022) described Si-rich garronite-Na from Hirado Island in Japan. The empirical crystal-chemical formula $(Na_{1.99}K_{0.27}Ca_{1.61})_{\Sigma3.87}[Fe_{0.01}Al_{5.31}Si_{10.64}]_{\Sigma15.96}O_{32}\cdot14.3H_2O$ has been calculated based on O = 32. The authors concluded that garronite-Na from Hirado Island, Japan represents a Ca–Na

solid solution in the garronite series. However, the crystals can be regarded as Ca-rich gobbinsite, the phase between gobbinsite and garronite-Ca solid solution (Fig. 7). The empirical formula of the crystals from Hirado Island, can be obtained from garronite-Ca or the gobbinsite end-member by combining $2M^+ + Al^{3+} \rightarrow M^+ + Si^{4+}$ and $D^{2+} \rightarrow 2M^+$ mechanism substitutions. According to the results reported on Si-rich garronite-Na (Hirahata *et al.*, 2022), the garronite series should include a broader Si/Al ratio range. This finding corroborates the existence
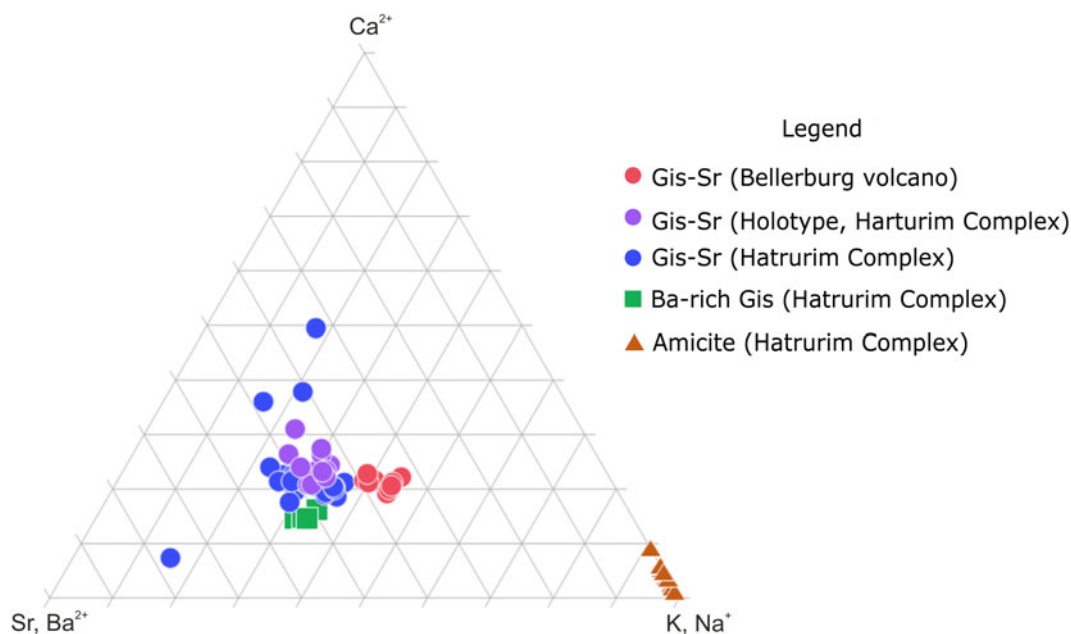
Figure 6. Ternary diagram showing atomic proportions in gismondine-Sr (Gis-Sr) from the Bellerberg volcano, gismondine-Sr, Ba-rich gismondine and amicite from the Hatrurim Complex (Table 2, Supplementary Table S3; Skrzyńska *et al.* 2023).
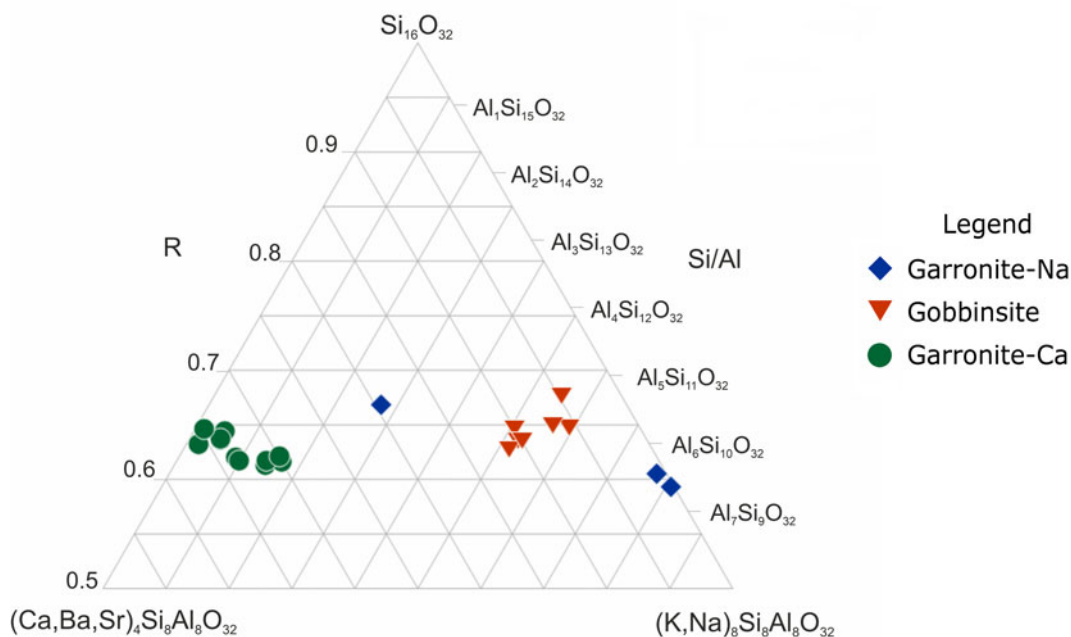

Figure 7. Compositional diagram for the garronite series and gobbinsite (Walker, 1962; Nawaz and Malone, 1982; Artioli, 1992; Artioli and Foy, 1994; Gatta *et al.*, 2010; Kónya and Szakáll, 2011; Grice *et al.*, 2016; Popova *et al.*, 2020; Hirahata *et al.*, 2022; Pauliš *et al.*, 2015).

of a solid solution between garronite-Ca and gobbinsite (Fig. 7). On the basis of the current rules for zeolite nomenclature (Coombs *et al.*, 1997), the grounds for gobbinsite and garronite-Na distinction would be insufficient. Therefore, we suggest a revision of the nomenclature of zeolites with the **GIS** framework type.

Summarising, the differences between gismondine-Sr and gismondine-Ca and between garronite-Ca and gobbinsite are similar. Two mineral series can be distinguished within **GIS** topology. Their end-member formulas should be calculated based on

the 16 framework T sites and 32 oxygen atoms (Table 1). The garronite–gobbinsite series includes Ca–Na solid solution with $R > 0.60$ and consists of garronite-Ca and gobbinsite. The general formula of this series can be written as $(M_y D_{0.5(x-y)})[Al_x Si_{(16-x)} O_{32}] \cdot n H_2 O$, where $x < 8$ and y is the content of the monovalent cations. Amicite, gismondine-Sr and gismondine-Ca belong to the gismondine series including Ca–Sr–K, Na solid solution with $R \approx 0.5$. The range of the gismondine series should be extended after a description of gismondine-Ba. The general
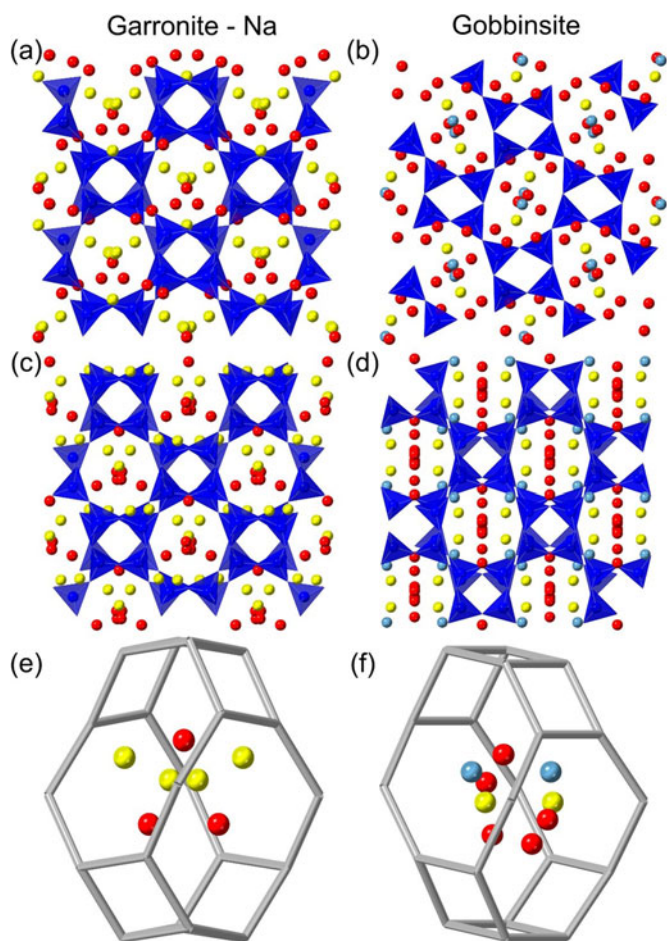
Figure 8. Comparison of garronite-Na (Grice *et al.*, 2016) and gobbinsite (Gatta *et al.*, 2010) structures along corresponding directions. (a) Structure of garronite-Na, view along [001]; (b) structure of gobbinsite, view along [100]; (c) structure of garronite-Na, view along [100]; (d) structure of gobbinsite, view along [010]; (e) *t-gsm* cage of garronite-Na; and (f) *t-gsm* cage of gobbinsite. Red sphere – water molecules; yellow sphere – sodium ions; pale blue sphere – calcium ions.

formula for the series with an *R*-value of ∼0.5 can be written as follows $(M_yD_{0.5(8-y)})[Al_8Si_8O_{32}]\cdot nH_2O$. The garronite and gismondine series differ from each other in terms of their *R*-value. So far, there are no available data on **GIS** minerals whose composition ranges between the *R*-value of the garronite and gismondine series. Hence, two separated series can be distinguished. The Raman band between $475\ cm^{-1}$ and $485\ cm^{-1}$ is distinctive for the garronite series, whereas the band around $460\ cm^{-1}$ is characteristic of the gismondine series. The displacement of Raman spectra presumably originates because of different *R*-values. In contrast, the extra-framework cations have a limited influence on Raman spectra of **GIS** zeolites.

References

Albert B.R., Cheetham A.K., Stuart J.A. and Adams C.J. (1998) Investigations on P zeolites: synthesis, characterisation, and structure of highly crystalline low-silica NaP. *Microporous and Mesoporous Materials*, **21**, 133–142.

Alberti A. and Vezzalini G. (1979) The crystal structure of amicite, a zeolite. *Acta Crystallographica*, **B35**, 2866–2869.

Armbruster T. and Gunter E. (2001) Crystal structures of natural zeolites. Pp. 1–68 in: *Natural Zeolites: Occurrence, Properties, Applications*. Reviews in Mineralogy and Geochemistry, Mineralogical Society of America and the Geochemical Society.

Artioli G. (1992) The crystal structure of garronite. *American Mineralogist*, **77**, 189–196.

Artioli G. and Foy H. (1994) Gobbinsite from Magheramorne Quarry, Northern Ireland. *Mineralogical Magazine*, **58**, 615–620.

Artioli G. and Marchi M. (1999) On the space group of garronite. *Powder Diffraction*, **14**, 190–194.

Auerbach S.M., Carrado K.A. and Dutta P.K. (editors) (2003) *Handbook of Zeolite Science and Technology*. M. Dekker, New York, 1184 pp.

Baerlocher C. and Meier W.M. (1972) The crystal structure of synthetic zeolite Na-P 1, an isotype of gismondine. *Zeitschrift für Kristallographie*, **135**, 339–354.

Baerlocher C., McCusker L.B. and Olson D.H. (2007) *Atlas of Zeolite Framework Types*. 6th revised edition. Elsevier, Amsterdam, 398 pp.

Bauer T. and Baur W.H. (1998) Structural changes in the natural zeolite gismondine (GIS) induced by cation exchange with Ag, Cs, Ba, Li, Na, K and Rb. *European Journal of Mineralogy*, **10**, 133–148.

Borodina U., Goryainov S., Krylova S., Vtyurin A. and Krylov A. (2022) The behavior of zeolites wairakite and phillipsite at high P-T parameters. *Spectrochimica Acta*, **A273**, 120979.

Braithwaite R.S.W., Dyer A. and Wilson J.I. (2001) Gismondine-Ba, a zeolite from the weathering of slag. *Journal of the Russell Society*, **7**, 83–85.

Calvo M., Viñals J., Sanz A. and Martí J. (2013) Zeolites and associated minerals in the vacuoles of some of the Campo de Calatrava volcanoes – Ciudad Real, Spain. *Mineral up*, **3**, 54–69.

Čejka J., van Bekkum H., Corma A., and Schueth F. (editors) (2007) *Introduction to Zeolite Science and Practice*. 3rd Revised Edition. Studies in Surface Science and Catalysis, **168**. Elsevier, Amsterdam, 1058 pp.

Chester A.W. and Derouane E.G. (editors) (2009) *Zeolite Chemistry and Catalysis*. Springer Netherlands, Dordrecht, Netherlands.

Chukanov N.V., Aksenoy S.M., Rastsvetaeva R.K., Blass G., Varlamov D.A., Pekov I.V., Belakovskiy D.I. and Gurzhiy V.V. (2015) Calcinaksite, $KNaCa(Si_4O_{10})\cdot H_2O$, a new mineral from the Eifel volcanic area, Germany. *Mineralogy and Petrology*, **109**, 397–404.

Coombs D., Alberti A., Armbruster T., Colella C., Galli E., Grice J.D., Liebau F., Mandarino J.A., Minato H., Nickel E.H., Passaglia E., Peacor D.R., Quartieri S., Rinaldi R., Ross M., Sheppard R.A., Tillmanns E. and Vezzalini G. (1997) Recommended nomenclature for zeolite minerals: report of the subcommittee on zeolites of the international mineralogical association, commission on new minerals and mineral name. *The Canadian Mineralogist*, **35**, 1571–1606.

Fischer K. (1963) The crystal structure determination of the zeolite gismondite $CaAl_2Si_2O_8\cdot 4H_2O$. *Mineralogical Notes*, **1963**, 664–672.

Galuskina I.O., Vapnik Y., Lazic B., Armbruster T., Murashko M. and Galuskin E.V. (2014) Harmunite $CaFe_2O_4$: A new mineral from the Jabel Harmun, West Bank, Palestinian Autonomy, Israel. *American Mineralogist*, **99**, 965–975.

Gatta G.D., Birch W.D. and Rotiroti N. (2010) Reinvestigation of the crystal structure of the zeolite gobbinsite: A single-crystal X-ray diffraction study. *American Mineralogist*, **95**, 481–486.

Geller Y.I., Burg A., Halicz L. and Kolodny Y. (2012) System closure during the combustion metamorphic "Mottled Zone" event, Israel. *Chemical Geology*, **334**, 25–36.

Gottardi G. (1979) Topologic symmetry and real symmetry in framework silicates. *Mineralogy and Petrology*, **26**, 39–50.

Gottardi G. and Galli E. (1985) *Natural Zeolites*. Minerals and Rocks Series Vol. 18. Springer-Verlag, Berlin, Heidelberg, New York, Tokyo.

Grice J.D., Rowe R. and Poirier G. (2016) Garronite-Na, A New Zeolite Species From Mont Saint-Hilaire, Québec. *The Canadian Mineralogist*, **54**, 1549–1562.

Gross S. (1977) The mineralogy of the Hatrurim Formation, Israel. *Geological Survey of Israel Bulletin*, **70**, 1–80.

Håkansson U., Fälth L. and Hansen S. (1990) Structure of a high-silica variety of zeolite Na-P. *Acta Crystallographica*, **C46**, 1363–1364.

Hansen S., Håkansson U. and Fälth L. (1990) Structure of synthetic zeolite Na-P2. *Acta Crystallographica*, **C46**, 1361–1362.

Hentschel G. (1987) *Die Mineralien der Eifelvulkane*. 2nd edition. Weise Verlag, München, Germany.

Hirahata Y., Kobayashi S. and Nishido H. (2022) Silica-rich garronite-Na from Hirado Island, Nagasaki Prefecture, Japan. *The Canadian Mineralogist*, **60**, 91–99.

Irran E., Tillmanns E. and Hentschel G. (1997) Ternesite, $Ca_5(SiO_4)_2SO_4$, a new mineral from the Ettringer Bellerberg/Eifel, Germany. *Mineralogy and Petrology*, **60**, 121–132.

Jackson M.D., Couper S., Stan C.V., Ivarsson M., Czabaj M.W., Tamura N., Parkinson D., Miyagi L.M. and Moore J.G. (2019) Authigenic mineral texture in submarine 1979 basalt drill core, Surtsey Volcano, Iceland. *Geochemistry, Geophysics, Geosystems*, **20**, 3751–3773.

Juroszek R., Krüger B., Marciniak-Maliszewska B. and Ternes B. (2022) Minerals of the arctite supergroup from the Bellerberg volcano xenoliths, Germany. *Mineralogical Magazine*, **86**, 929–939.

Kónya P. and Szakáll S. (2011) Occurrence, composition and paragenesis of the zeolites and associated minerals in the alkaline basalt of a maar-type volcano at Haláp Hill, Balaton Highland, Hungary. *Mineralogical Magazine*, **75**, 2869–2885.

Kraus W., Blaß G. and Effenberger H. (1999) Schäferite, a new vanadium garnet from the Bellberg volcano, Eifel, Germany. *Neues Jahrbuch für Mineralogie*, 123–134.

Krzątała A., Krüger B., Galuskina I., Vapnik Y. and Galuskin E. (2020) Walstromite, $BaCa_2(Si_3O_9)$, from rankinite paralava within gehlenite hornfels of the Hatrurim Basin, Negev Desert, Israel. *Minerals*, **10**, 407.

Krzątała A., Krüger B., Galuskina I., Vapnik Y. and Galuskin E. (2022) Bennesherite, $Ba_2Fe^{2+}Si_2O_7$: A new melilite group mineral from the Hatrurim Basin, Negev Desert, Israel. *American Mineralogist*, **107**, 138–146.

Lengauer C.L., Kolitsch U. and Tillmanns E. (2009) Flörkeite, $K_3Ca_2Na[Al_8Si_8O_{32}]\cdot12H_2O$, a new phillipsite-type zeolite from the Bellerberg, East Eifel volcanic area, Germany. *European Journal of Mineralogy*, **21**, 901–913.

Mihajlovic T., Lengauer C.L., Ntaflos T., Kolitsch U. and Tillmanns E. (2004) Two new minerals rondorfite, $Ca8Mg[SiO4]4Cl2$, and almarudite, $K(\square, Na)_2(Mn,Fe,Mg)_2(Be,Al)_3[Si_{12}O_{30}]$, and a study of iron-rich wadalite, $Ca_{12}[(Al_8Si_4Fe2)O_{32}]Cl_6$, from the Bellerberg (Bellberg) volcano, Eifel, Germany. *Neues Jahrbuch für Mineralogie - Abhandlungen*, 265–294.

Mozgawa W. (2001) The relation between structure and vibrational spectra of natural zeolites. *Journal of Molecular Structure*, **596**, 129–137.

Nawaz R. and Malone J.F. (1982) Gobbinsite, a new zeolite mineral from Co. Antrim, N. Ireland. *Mineralogical Magazine*, **46**, 365–369.

Novikov I., Vapnik Y. and Safonova I. (2013) Mud volcano origin of the Mottled Zone, South Levant. *Geoscience Frontiers*, **4**, 597–619.

Passaglia E. and Sheppard R.A. (2001) Crystal chemistry of zeolites. Pp. 69–104 in: *Natural Zeolites: Occurrence, Properties, Applications* (David Bish and Doug Ming, editors). Reviews in Mineralogy and Geochemistry, Volume 45, Mineralogical Society of America and the Geochemical Society, Chantilly, Virginia, USA.

Pauliš P., Hrůzek L., Janeček O., Sejkora J., Malíková R. and Pour O. (2015) Tschernichite, garronite-Ca and associated zeolite mineralization from Jehly u České Kamenice (Česká republika). *Bulletin mineralogicko-petrologického oddělení Národního muzea v Praze*, **23**, 147–170.

Pekov I.V. and Podlesnyi A.S. (2004) Kukisvumchorr deposit: Mineralogy of alkaline pegmatites and hydrothermalites. *Mineralogical Almanac*, **7**, 1–164.

Popova V.I., Kasatkin A.V., Popov V.A., Nikandrov S.N., Makagonov E.P., Kuznetsov A.M. and Škoda R. (2020) Zeolites in pegmatites and late veinlets of the Vishnevogorsky Alkaline-Carbonatite Complex (South Urals). *МИНЕРАЛОГИЯ* (*MINERALOGY*), **6**, 1–16 [in Russian].

Rudinger B., Tillmanns E. and Hentschel G. (1993) Bellbergite a new mineral with the zeolite structure type EAB. *Mineralogy and Petrology*, **48**, 147–152.

Sharygin V.V., Sokol E.V. and Vapnik Ye. (2008) Minerals of the pseudobinary perovskite-brownmillerite series from combustion metamorphic larnite rocks of the Hatrurim Formation (Israel). *Russian Geology and Geophysics*, **49**, 709–726.

Skrzyńska K., Cametti G., Galuskina I.O., Vapnik Y. and Galuskin E. (2022) Flörkeite, $(K_3Ca_2Na)[Al_8Si_8O_{32}]\cdot12H_2O$: A rare zeolite from pyrometamorphic rocks of the Hatrurim Complex, Israel. *Lithosphere*, **2022**, 1343791.

Skrzyńska K., Cametti G., Galuskina I.O., Vapnik Y. and Galuskin E.V. (2023) Gismondine-Sr, $Sr_4(Al_8Si_8O_{32})\cdot H_2O$, a new strontium dominant, orthorhombic zeolite of the gismondine series from the Hatrurim Complex, Israel. *American Mineralogist*, **108**, 249–258.

Sokol E.V., Novikov I.S., Zateeva S.N., Sharygin V.V. and Vapnik Ye. (2008) Pyrometamorphic rocks of the spurrite-merwinite facies as indicators of hydrocarbon discharge zones (the Hatrurim formation, Israel). *Doklady Earth Sciences*, **420**, 608–614.

van Reeuwijk L.P. (1971) The dehydration of gismondite. *American Mineralogist*, **56**, 1655–1659.

Vapnik Y., Sharygin V.V., Sokol E.V. and Shagam R. (2007) Paralavas in a combustion metamorphic complex Hatrurim Basin, Israel. Pp. 1–21 in: *Geology of Coal Fires: Case Studies from Around the World* (G.B. Stracher, editor). The Geological Society of America Reviews in Engineering, v. XVIII. The Geological Society of America, Boulder, Colorado, USA, https://doi.org/10.1130/2007.4118(09).

Vezzalini G. and Oberti R. (1984) The crystal chemistry of gismondines : the non-existence of K-rich gismondines. *Bulletin de Minéralogie*, **107**, 805–812.

Vezzalini G., Quartieri S. and Alberti A. (1993) Structural modifications induced by dehydration in the zeolite gismondine. *Zeolites*, **13**, 34–42.

Vezzalini G., Alberti A., Sani A. and Triscari M. (1999) The dehydration process in amicite. *Microporous and Mesoporous Materials*, **31**, 253–262.

Wadoski-Romeijn E. and Armbruster T. (2013) Topotactic transformation and dehydration of the zeolite gismondine to a novel Ca feldspar structure. *American Mineralogist*, **98**, 1988–1997.

Walker G.P.L. (1962) Garronite, a new zeolite, from Ireland and Iceland. *Mineralogical Magazine and Journal of the Mineralogical Society*, **33**, 173–186.

Warr L.N. (2021) IMA-CNMNC approved mineral symbols. *Mineralogical Magazine*, **85**, 291–320, https://doi.org/10.1180/mgm.2021.43